May 2018

Novel Solar Cells Based on Two-Dimensional Nanomaterials and Recycled Lead Components

Xiaoru Guo
University of Wisconsin-Milwaukee

NOVEL SOLAR CELLS BASED ON TWO-DIMENSIONAL NANOMATERIALS AND RECYCLED LEAD COMPONENTS

by

Xiaoru Guo

A Dissertation Submitted in

Partial Fulfillment of the

Requirements for the Degree of

Doctor of Philosophy

in Engineering

at

The University of Wisconsin-Milwaukee

May 2018

ABSTRACT

NOVEL SOLAR CELLS BASED ON
TWO-DIMENSIONAL NANOMATERIALS AND
RECYCLED LEAD COMPONENTS

by

Xiaoru Guo

The University of Wisconsin-Milwaukee, 2018
Under the Supervision of Professor Junhong Chen

To meet the rapidly growing demand for energy and reduce the use of dwindling fossil fuels, the efficient utilization of renewable energy is a constant pursuit globally. Because solar cells convert vastly available sunlight into electricity, developing high-performance and low-cost solar cells is a top strategy for future energy supply. Dye-sensitized solar cells (DSSCs) and perovskite solar cells (PSCs) are the most promising choices. In the meantime, highly concentrated sulfuric acids from retired lead-acid batteries become an environmental concern, and lead contamination in drinking water raises concerns in general public. This study addresses both above-mentioned problems by using two-dimensional (2D) nanomaterials and recycled lead for solar cell fabrication.

Firstly, 2D nanomaterials are used to improve the performance of solar cells as a counter electrode in DSSCs and a hole transport material (HTM) in PSCs. MoS_2/graphene hybrids are hydrothermally prepared at different temperatures. A phase transition is observed from 150 to 210 °C, and the reaction temperature of 180 °C leads to the best performing 2D nanomaterial hybrids for electrochemical catalysis. Semi-transparent PSCs are explored in smart buildings to simultaneously adapt to indoor lighting conditions and convert part of sunlight into electricity.

Furthermore, through crumbling graphene oxide with copper thiocyanate at 650 °C, a new HTM is prepared for PSCs with steady, high performance and a low cost.

Secondly, the recovery of lead contents from waste acid and contaminated water is studied by using nanocarbon materials. The lead removal in acid is evaluated through adsorption, filtration, and capacitive deionization (CDI). The removal rate is limited, but as-obtained lead wastes are then successfully reformed to produce perovskite precursors. A CDI process through sulfur-treated carbon materials is studied to selectively collect lead contaminants in water. Complete lead recovery and reformation for perovskite precursors is explored to obtain PSCs featuring a low cost and an overall positive environmental impact.

This study addresses a full life cycle of solar cell materials to meet sustainable requirements. Taking advantage of outstanding properties of 2D nanomaterials, results from the study will lead to next-generation solar cells featuring enhanced performance, a lower cost, and better environmental sustainability.

TABLE OF CONTENTS

LIST OF FIGURES

LIST OF TABLES

LIST OF ABBREVIATIONS

0D	zero-dimensional
1D	one-dimensional
2D	two-dimensional
3D	three-dimensional
BET	Brunauer–Emmett–Teller
CDI	capacitive deionization
CNT	carbon nanotube
CV	cyclic voltammetry
CVD	chemical vapor deposition
CX	carbon xerogel
DFT	density functional theory
DMF	N,N'-dimethylformamide
DMSO	dimethyl sulfoxide
DSSC	dye-sensitized solar cell
EDS	energy-dispersive X-ray spectroscopy
EIS	electrochemical impedance spectroscopy
EQE	external quantum efficiency
ETM	electron transfer material
FA	formamidinium
FE-SEM	field-emission scanning electron microscopy
FF	fill factor
FTO	fluorine-doped tin oxide

GBL	gamma-butyrolactone
GCE	glassy carbon electrode
GO	graphene oxide
GQD	graphene quantum dot
HER	hydrogen evolution reaction
HRTEM	high-resolution transmission electron microscopy
HTM	hole transport material
ICP-AES	inductively coupled plasma atomic emission spectroscopy
ICP-MS	inductively coupled plasma mass spectroscopy
IR	infrared
i_{SC}	short-circuit current
ITO	indium tin oxide
LSV	linear sweep voltammetry
MA	methylammonium
MOF	metal-organic framework
NCX	nitrogen-doped carbon xerogel
NMP	N-methyl-2-pyrrolidone
PCE	power conversion efficiency
PV	photovoltaic
PVDF	polyvinylidene fluoride
PSC	perovskite solar cell
RHE	reversible hydrogen electrode
rGO	reduced graphene oxide

SAED	selected area electron diffraction
sp. gr.	specific gravity
TEM	transmission electron microscopy
TMD	transition metal dichalcogenide
V_{OC}	open-circuit voltage
XPS	X-ray photoelectron spectroscopy
XRD	X-ray diffraction

ACKNOWLEDGMENTS

I would like to thank Dr. Chen for his patience and guidance. He introduced me to the new world of nanomaterial research and directed me throughout my studies. I am grateful to the post-doctoral researchers in Dr. Chen's group, for their teaching on my experiment skills and guidance on my theoretical study. Thanks to all my labmates for their support and help. I would also like to thank my committee members for their time and advising.

It is also my great honor to have all my collaborators. They shared their genius ideas with me and enhanced my knowledge and skills. Thanks to Dr. Hardcastle for all instrument training and help in AAF, thanks to Dr. Owen for FE-SEM support, and thanks to Dr. Qu for assisting ICP-AES measurements.

Lastly, I would like to thank my wife, Huilei Zhao and my family, for their understanding and support. Thanks to all my friends for their insprations.

Chapter 1. Background and Literature Review

1.1. Introduction to solar cells and current research trends

It has become an important and urgent quest to seek clean and sustainable alternatives for fossil fuels because of the diminishing supply of these fuels, the ever-increasing demand for energy, and the environmental challenges associated with fossil fuel consumption. Many types of renewable energies (e.g., solar, wind, and hydraulic energies) have been actively explored, and related technologies for energy conversion and storage have been developed and/or commercialized for building a "sustainable energy future".[1] Solar energy is an abundant, unlimited, and clean source and has been widely considered as one of the top options among renewable energy sources. However, since solar energy has a relatively low energy density (i.e., power per unit area), the realistic and competitive employment of solar cells requires a large-scale collection area and/or high efficiency.

So far, three generations of solar cells have been developed.[2-4] Silicon-based p-n junction photovoltaic (PV) cells, including polysilicon and monocrystalline Si cells, are the first-generation solar cells, which offer a high efficiency but are expensive to manufacture for reasons such as the very high temperature (over 1,600 °C) required to obtain Si by reducing silica. Despite the continuous improvement in the fabrication process, the energy that one Si-based PV cell can generate in its lifetime is still less than that needed to fabricate it.[5] To overcome the high cost issue for Si PV cells, thin-film solar cells with a low cost (or the second generation solar cells) were developed using inexpensive amorphous silicon and other semiconducting materials; however, the efficiency of the second generation solar cells is relatively low compared with the Si cells.[3,4] The third generation solar cells have been explored with the aim to achieve both a low cost and

relatively high efficiency. Among the technologies for emerging third generation solar cells, dye-sensitized solar cells (DSSCs) are considered as a technically and economically viable option, particularly in comparison with Si-based p–n junction PV devices.[2] Recently, perovskite solar cells (PSCs) show higher efficiencies than regular DSSCs with a low cost.[6-8] Both DSSCs and PSCs are widely studied nowadays to optimize their performance and meet future energy requirements.

The studies of PSCs began with the DSSC sensitizer study to utilize the photoelectron generation ability of perovskite crystals by Miyasaka *et al.* in 2009[7]. The general model of a DSSC, initially proposed and developed by Michael Graetzel in 1991, is a liquid junction device that consists of a nanocrystalline TiO_2 photoanode, an iodine redox (I_3^-/I^-) pair electrolyte, and a counter electrode (also called cathode) typically made of a thin film of Pt. The same group modified the initial DSSC design and further developed a monolithic architecture in 1996, in which the counter electrode was moved to the photoanode side and separated from the photoanode with a thin spacer of insulating material. The monolithic design reduced the cost of transparent conductive materials.[9] Different types of DSSCs are mainly distinguished by sensitizing materials including organic dyes, quantum dots, inorganic dyes, and perovskite crystals.[10,11] In the past two decades, a lot of studies have been carried out on each and every part of the DSSC to improve its performance. From the materials perspective, new materials and conventional materials with novel morphologies and structures have been explored extensively for each component in the DSSC. For example, various less expensive alternatives, such as cobalt sulfide (CoS), have been studied as the catalytic material to replace expensive platinum (Pt) in the counter electrode [12,13]; all-solid-state DSSCs were fabricated and reported to reach a high efficiency[14]; more recently, perovskite materials were introduced into the solar cell study and raised the lab efficiency record over 20%[6,15-17].

The sandwiched structure of a DSSC is shown in Figure 1-1. The whole cell is mechanically supported by transparent conductive materials, such as conductive polymers, indium tin oxide (ITO) glass, and fluorine-doped tin oxide (FTO) glass. Inside the cell, a monolayer of dye molecules, attached on semiconducting materials (typically TiO_2), is hosted on the photoanode; an electrocatalyst material on a counter electrode (cathode in Figure 1-1) is separated from the photoanode by an electrolyte with a selected redox mediator. The operating cycle of the DSSC starts with sensitizers (dyes in Figure 1-1) absorbing photons, leading to the injection of electrons from excited dye (S*) molecules to the conduction band of large bandgap semiconducting materials (TiO_2 in Figure 1-1). After diffusing in the current collector and transferring in conducting glass, the electrons are returned through an external circuit to the electrolyte or hole conductor by the electrocatalyst materials at the counter electrode. The mediators in the electrolyte or hole conductor finally complete the circuit with a reduction reaction to regenerate dye molecules.[11] Among all types of solar cells, the DSSC is the kind that separates photon absorption and charge transportation during photoelectric conversion, mimicking the photosynthesis process in the green leaves of plants.[10] This separation yields significant advantage for improving the DSSC design, since all cell elements can be analyzed and optimized individually.[5]

Despite the advantages of DSSCs over silicon solar cells, critical challenges still limit the commercialization of DSSCs. Firstly, the overall efficiency of DSSCs is still low, and the computed module cost per peak Watt is still higher than the market acceptance.[18] Also the in-lab record efficiency of DSSCs is lower than that of current Si solar cells, and a significant boost to the efficiency is highly demanded. Secondly, to bring down the cost of DSSCs, new materials are

sought, especially the catalyst for counter electrodes. Current technology still relies on platinum-based materials for counter electrodes, and the associated cost is significant. Thirdly, the stability of the liquid electrolyte is a concern for long-term field use, due to evaporation and aging. Although multiple solid or quasi-solid electrolytes have been discovered in recent years, the stability of these new electrolytes is still limited.

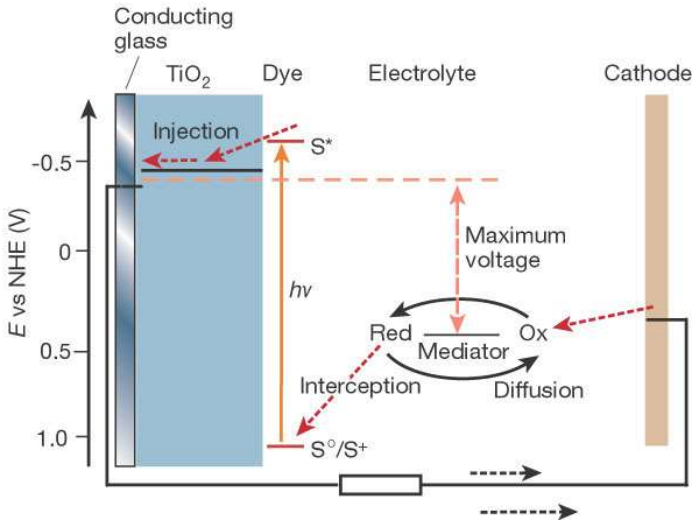

Figure 1-1. DSSC working principles. (Gratzel, 2001) Copyright Nature Publishing Group, 2001.

Two types of PSC architectures have been developed. One is to fabricate the PSC in the DSSC style; and the other is to build a planar heterojunction, which is similar with that in Si-based solar cells.[19,20] A comparison of both structures is shown in Figure 1-2 with four different designs in two architectures. Compared with regular DSSCs working through catalytic reactions, PSCs function through electron-hole separation processes in a crystal.[21,22] The p-n-junction-like behavior makes the material appropriate for the simple planar design. Perovskites have a pseudocubic crystal structure, with two types of cations at the corners and the center of the lattice, respectively, as shown in Figure 1-2a. The architecture of DSSC-style PSCs is the same as that of

regular DSSCs, but the hole transport material (HTM) is essential for stable performance instead of liquid or quasi-solid electrolyte.[7] This is due to both the dissolving of perovskite crystals in most liquid solvents and the degradation of perovskite materials. In a planar architecture, the mesoporous layer of semiconducting material is removed, while the thin layers of electron and hole transport materials remain on both sides, as shown in Figure 1-2c and e. However, the planar structure requires a high crystallization quality of perovskites and is always hard to achieve, which is a drawback for this cheaper design compared with the DSSC architecture.[23-27]

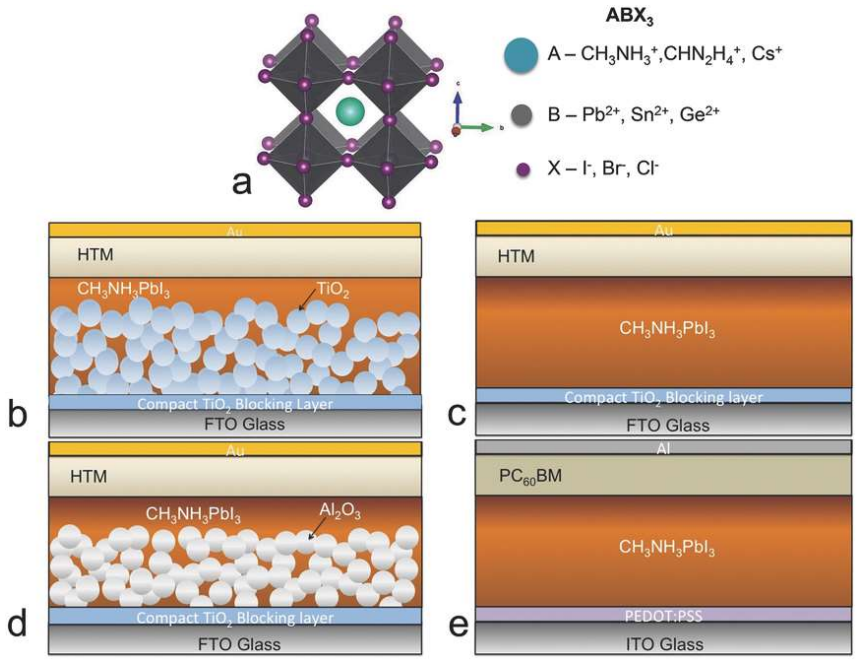

Figure 1-2 Schematic comparison of the DSSC style PSC and the planar style PSC. (a) An ABX_3 perovskite crystal structure with common groups for the A, B, and X positions. (b) DSSC-style PSC with mesoporous TiO_2. (c) The planar heterojunction PSC. (d) The mesosuperstructured solar cells with DSSC architecture. (e) The "inverted" planar heterojunction solar cell using organic electron and hole selective contacts.[28] Copyright Nature Publishing Group, 2013.

The effective perovskite crystals for PSCs are organometal halides, which always have small C-N groups at A position, lead (Pb^{2+}) or tin (Sn^{2+}) at B position, and halides at X positions.[20] The organic-inorganic perovskites draw great attention due to their insulating to metallic transition by increasing the layer number of inorganic layers in $(C_4H_9NH_3)_2(CH_3NH_3)_{n-1}Sn_nI_{3n+1}$ crystals discovered in superconductor studies.[29] Later the <110>-oriented $CH_3NH_3SnI_3$ sheet in the huge crystal was discovered and a suitable bandgap was noticed.[30] After a report in 2009, scientists realized the possibility of tuning bandgaps of perovskites by utilizing different organic groups and halides, and a comparison is shown in Figure 1-3. Currently, the DSSC-style PSC holds the highest efficiency record, with lithium-treated TiO_2 as electron transfer material (ETM), mixed methylammonium (MA) and formamidinium (FA) as organic parts in perovskite crystals, copper (I) thiocyanate (CuSCN) as HTM, and graphene oxide (GO) as interface material.[17]

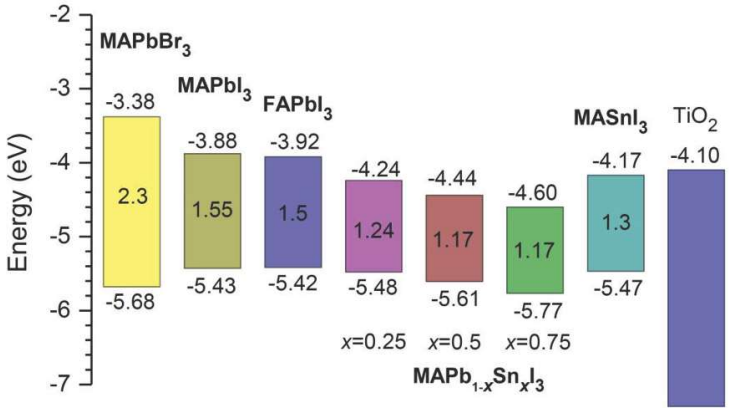

Figure 1-3 Comparison of band positions in some common perovskites.[31] Copyright ACS, 2014.

A major challenge of PSCs is their stability. The perovskite crystals can degrade quickly with even slight exposure to water vapor. Some research demonstrated more stable cells can be achieved with the band gap tuned between 1.56 eV and 1.48 eV by partially substituting MA with FA.[16] Also, the HTMs used in PSCs are sensitive to moisture and oxygen, and can be etched away during

a short period of storage. The discontinuous HTM film after degradation exposes the covered perovskite layer, which speeds up the failure of PSCs. Hysteresis effect of PSCs is another widely studied issue, which is considered mostly because of the interface between perovskite crystals and charge transport layers.[28,32] In addition, the toxicity of Pb^{2+} is a public concern. Studies of PSCs have been focusing on replacing Pb with Sn, Cu or other less hazardous elements[33,34], replacing organic groups with alkali metals or other cation groups for higher stability[35,36], improving HTM stability[17,37-39], improving the crystallization of perovskites[24,26,27] and more.

1.2. 2D nanomaterials for solar cell applications

1.2.1. Development and properties of graphene

According to the International Union of Pure and Applied Chemistry (IUPAC), graphene is defined as "a single carbon layer of the graphite structure, describing its nature by analogy to a polycyclic aromatic hydrocarbon of quasi infinite size".[40] Nevertheless, the term 'graphene' has been used loosely to represent not only pristine graphene but also its derivatives. The graphene-based materials we discuss here include pristine graphene, GO nanosheets, and reduced graphene oxide (rGO) nanosheets.

Although graphene-based materials are not the first carbon materials used in solar cells, they show some outstanding and unique potential compared with other carbon materials. Many different types of carbon materials have been applied in emerging solar cell studies, from earlier graphite-like carbon for conductivity and catalytic reactivity, to recently discovered fullerene, diamond-like carbon, carbon nanotube (CNT), and graphene. Graphene-based materials have attracted significant interests because of their superior mechanical strength, electrical conductivity, and

thermal conductivity compared with other common materials. Nevertheless, these carbon materials are structurally related. Figure 1-4 is a schematic illustrating the relationship of carbon materials. Graphene (2D) can be viewed virtually as the basic modeling unit of other carbon materials since fullerene (0D), CNT (1D), and graphite (3D) can be "obtained" by wrapping, rolling, and stacking graphene sheets, respectively.[41] Being limited by its dimension (i.e., 0D), fullerene is very differently from CNTs and graphene. Comparing CNT with graphene, their properties are mostly similar, while CNT has slightly different chemical and electronic properties due to the high aspect ratio and strain effects. Strictly speaking, CNT and fullerene are not exactly sp^2-hybridized because of strain effects. Although graphene has no significant advantage over CNT, the mono-atomic 2D sp^2-hybridized carbon layer has a much larger and thinner surface, which leads to higher reactivity and transparency.[41-44]

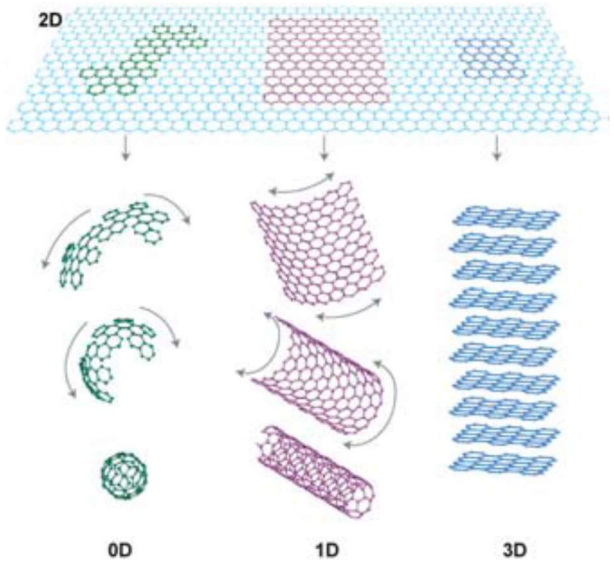

Figure 1-4 Graphene is the basic building block of other carbon structures including 0D fullerene, 1D CNT, and 3D graphite. [41] Copyright Nature Publishing Group, 2007.

Although graphene-based materials are not core parts for emerging solar cells, the unique and outstanding properties of graphene are ideal for addressing many known issues in solar cells, such as photo-electron generation, charge carrier transfer, and surface reaction and reduction. For instance, it has been shown that graphene has an ultrahigh theoretical surface area of 2,600 m^2/g and high thermal conductivity of 5×10^3 W/(m·K). Long range π-conjugation gives graphene exceeding electron mobility of ~15,000 $m^2/(V\cdot s)$ at room temperature and a current density of ~1×10^9 A/cm^2.[45-48] For perfect graphene, it absorbs 2.3% of visible light with an extinction coefficient of about 10^8 mol/cm^2.[49] Although pristine graphene has a zero bandgap, the quantum confinement effect theoretically allows graphene with the structure of a nanoribbon or a quantum dot (so-called graphene nanoribbon and graphene quantum dot) to have a tunable band gap covering the entire solar light spectrum. This tunability in band gap makes graphene an attractive candidate for photo-electron generation. At the same time and more obviously, graphene offers a 2D conductive support path for electron transfer with a work function of 4.42 eV, which can enhance the electron transfer and reduce the electron-hole recombination rate. Additionally, the large surface area creates more occasions for reactive group decoration and enhances the chemical reaction and reduction processes, which is essential for DSSCs.

Many methods have been developed to prepare graphene, for example, mechanical exfoliation,[42] micromechanical cleavage,[44] graphitization of SiC,[50] solution exfoliation in organic solvents and surfactant solutions,[51,52] deposition from a gaseous precursor through chemical vapor deposition (CVD),[53-55] and roll-to-roll production of films grown on copper foil.[56] Among those methods, reduction of GO and CVD synthesis on metal substrates [54,55] are two most popular approaches because of their easiness, low cost, suitability for large-scale production, and accessibility by most

labs. rGO is commonly synthesized in two steps: first producing GO using Hummer's method or its derivatives,[57-61] and then reducing GO thermally or with reductants, such as hydrazine, to obtain rGO sheets with sizes usually in the range of 1~10 μm. This method is solution-processable and can produce a large amount of rGO sheets at one time. One concern associated with rGO is that the chemical reduction process often involves toxic chemicals and is not always environmentally friendly; however, some "green" reducing agents and environmentally friendly processes have been reported.[62,63] The CVD method is a better way to produce large-size graphene sheets with a high quality close to pristine graphene. A typical CVD process uses a carbon source, such as methane, and a substrate heated to high temperatures (such as ~1,000 °C) under an H_2 environment. Different substrates, such as nickel, copper, and SiO_2, are used with different chemistry for the deposition of a graphene sheet.[64] Mono-, bi-, and tri-layer graphene sheets with a desirable size can be produced by carefully choosing the synthesis conditions in a CVD process, such as time, temperature, and the type and size of a substrate.[54,55]

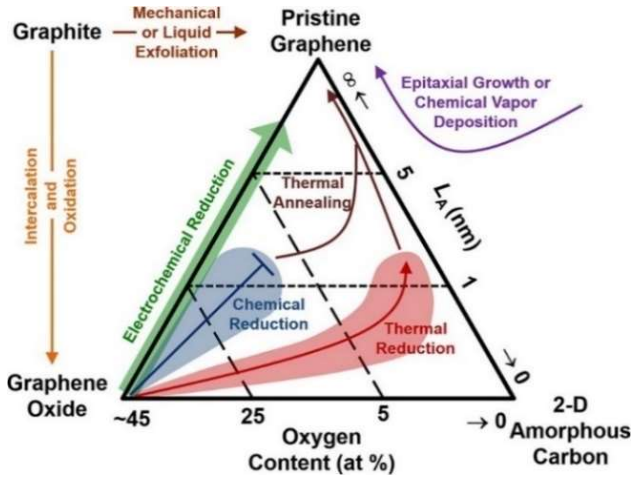

Figure 1-5 Production of graphene materials. The triangle qualitatively represents the material space encompassed by rGOs.[65] Copyright 2013 Joseph Roy-Mayhew.

Roy-Mayhew *et al.* compared graphene materials prepared by CVD methods and different reducing methods in Figure 1-5. CVD prepared graphene has a lower oxygen content and a larger lateral dimension than rGO from reducing methods. The variation of properties among graphene materials requires the selection of suitable graphene materials on the basis of intended applications. Since rGO sheets are usually small in size and soluble in various solvents, coating methods such as dip-coating and spinning coating are used to fabricate DSSC electrodes.[66-68] Also, because their surfaces are chemically modified, rGO sheets are used as additives to improve the electron transfer in semi-conducting material layers. [69,70] CVD synthesized graphene sheets have excellent transparency and electrical conductivity and can be directly transferred from the synthesis substrate to suitable transparent substrates and used as electrodes to collect electrons.[71-73]

The preparation method itself has a strong effect on the graphene properties. For example, intrinsic graphene is expected to have electron mobility as high as 200,000 $cm^2/(V\ s)$ at room temperature; [74,75] however, most reported values are always much lower, because various types of defects are present in graphene sheets synthesized from different methods. Firstly, holes and grain boundaries as shown in Figure 1-6 are common defects in a graphene sheet, which leads to inferior mechanical and optical properties. These defects may affect graphene properties in many ways; for example, lower mechanical and optical properties are unfavorable for improving the performance of the transparent electrode, while defects also lead to more active carbon atoms and a larger surface area, creating opportunities for catalytic applications in DSSCs. Secondly, functional groups introduced onto a graphene surface in many GO synthesis processes cannot be removed completely during reduction, which leads to higher surface resistivity of rGO compared with pristine graphene. Thirdly, layer stacking is a challenging issue for most methods, and few-layer and even multi-layer

graphene sheets usually co-exist with monolayer ones. Multi-layer graphene generally has lower transparency, although there are reports showing more layered graphene has better conductivity.[76]

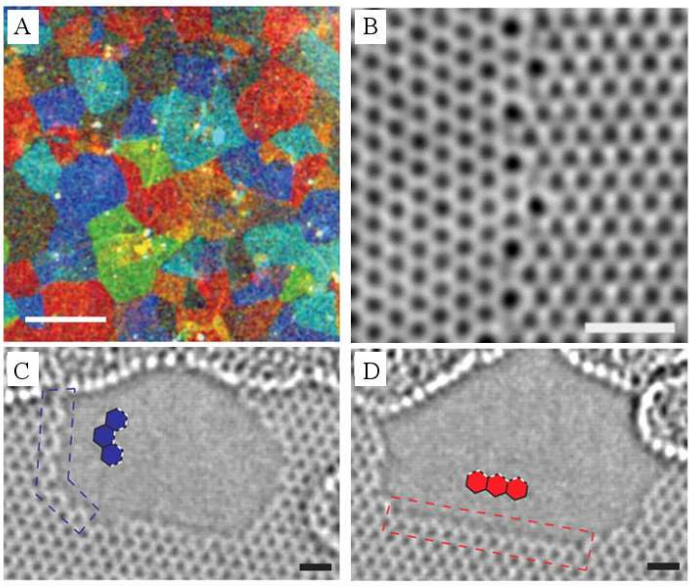

Figure 1-6 Common defects in graphene sheets. (A) CVD-grown graphene false-color DF-TEM image; it shows grain boundaries in one graphene sheet;(Lee et al., 2013b) Copyright AAAS, 2013. (B) Aberration-corrected TEM image showing the atomic structure of graphene boundary;[77] Copyright Nature Publication Group, 2013. (C) and (D) Aberration-corrected TEM images of holes on graphene sheet. (C) is armchair boundary and (D) is zigzag boundary.[78,79] Copyright AAAS, 2009. Scale bars: (A) 3 μm; (B) 0.8 nm; (C) and (D) 0.5 nm.

1.2.2. Applications of graphene in solar cells

Benefiting from its outstanding properties, graphene has been widely used in many applications. In solar cells, graphene's high conductivity, good optical transparency, and large Young's modulus have brought new opportunities for emerging solar cell developments. Meanwhile, the abundant carbon source and the simplicity of synthesizing graphene-based materials can potentially lower the cost of DSSCs and PSCs. Although the mechanisms for graphene to enhance the performance are yet to be fully understood, encouraging results have been obtained in applying graphene

materials to DSSCs and PSCs, which justifies the necessity to further investigate the use of graphene-based materials in solar cells.

Firstly, graphene has been a strong alternative for transparent conducting electrodes. The transparent conducting electrodes (or current collectors) of a solar cell are often fabricated on a quartz substrate coated with TCOs (e.g., ITO and FTO), which have good stability, excellent electrical conductivity (sheet resistance $R_S < 10\ \Omega\ sq^{-1}$), and good optical transparency (> 80% for visible light).[45,80] But the cost of TCO can be up to nearly half of the total cost of a DSSC cell.[81] ITO can form a high-quality film with a smooth surface on glass but is more expensive than FTO. Additionally, the thermal stability of ITO films is limited to 350 °C, above which SnO_2 crystals peel off from glass substrates.[81] This is a critical issue for DSSCs and PSCs, because the formation of mesoporous and compact TiO_2 layer requires an annealing temperature at 500 °C. But the surface of FTO films is reported to be uneven, and it is usually difficult to form high quality FTO films especially for organic materials.[82] Graphene has excellent electrical, optical, and mechanical properties that are attractive for making transparent conducting electrodes with a desirable performance. Some calculations show the work function of graphene is ~4.42 eV, which is close to that of an FTO (4.4 eV).[55,76,83] Figure 1-7 compares the bandgap positions of common semiconducting materials with a calculated graphene work function. There are very small offsets between most semiconducting material conduction band edges and the work function of graphene, implying that graphene can work as a low energy loss electron shuttle to collect electrons from these semiconductors.

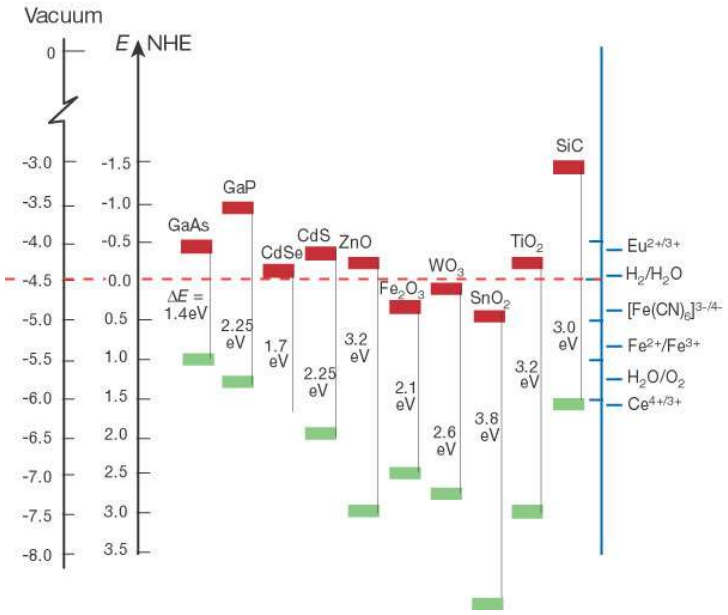

Figure 1-7 The band positions of several semiconducting materials in aqueous electrolyte at pH = 1. The red dashed line is about the work function of graphene.[84] Copyright Nature Publication Group, 2001.

Muellen *et al.* [73] pioneered in applying graphene as a transparent conducting electrode material. By dip-coating from a hot GO solution, their graphene electrode obtained a high conductivity of 550 S cm^{-1} and a transparency of more than 70% over a 1,000-3,000 nm range. The solid-state DSSC in this work had a power conversion efficiency (PCE) of 0.26%, which was lower than that of the FTO-based device (0.84%). This is mainly due to lower conductivity and optical transparency of rGO. For GO solution based graphene electrodes, the thickness of graphene layer can be controlled by the coating process, and electrode quality is greatly affected by GO/rGO properties and conductivities. The sheet resistance of these graphene electrodes commonly falls between 1 and 0.1 kΩ sq^{-1}, and the optical transparency at 550 nm is about 80%.[54,55,76,83,85] GO or rGO based electrodes can be easily fabricated on a large scale and can host different types of semiconducting layers. CVD provides another approach to preparing large-scale monolayer graphene sheets with a quality close to pristine graphene. Bae *et al.*[56] reported the roll-to-roll

production of 30-inch graphene films for transparent electrodes. Figure 1-8 schematically shows the roll-to-roll procedure of the graphene electrode preparation. The monolayer graphene electrode had resistance as low as ~125 Ω sq^{-1} and 97.4% optical transmittance. A four-layer stacked electrode showed resistance ~30 Ω sq^{-1} and transparency ~90%. These values are comparable with commercial TCO electrodes, although resistance is still high for transparent conductive electrodes.

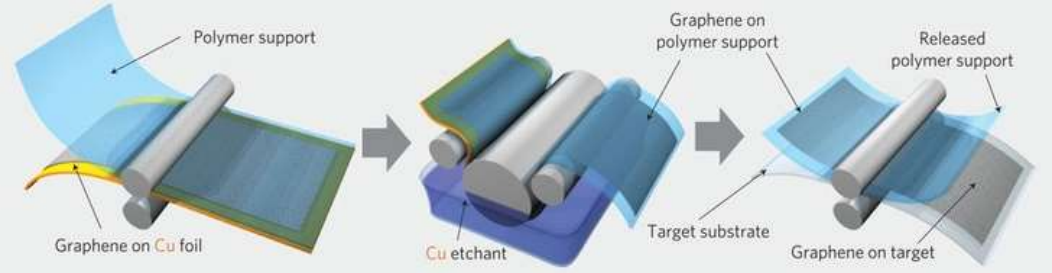

Figure 1-8 Schematic of the roll-based production of graphene films grown on a copper foil. The process includes adhesion of polymer supports, copper etching (rinsing) and dry transfer-printing on a target substrate. A wet-chemical doping can be carried out using a set-up similar to that used for etching.[56] Copyright Nature Publishing Group, 2010.

Graphene is also suitable to be used as a flexible transparent and conductive electrode. For example, Batmunkh *et al.*[86] processed GO in solution and created flexible graphene electrode to prepare flexible PSCs. After chemical processing, annealing and surface modification, the flexible electrode had a surface resistance as low as 1.96 kΩ sq^{-1} and transmittance of 42.3%. The efficiency of achieved PSC was ~0.6%. Yoon *et al.*[87] used single-layer CVD graphene as a flexible electrode to prepare PSCs, with molybdenum oxide as surface modification. The maximum efficiency reached 17.3%, and the cell retained >90% of its original efficiency after 1,000 cycle bending.

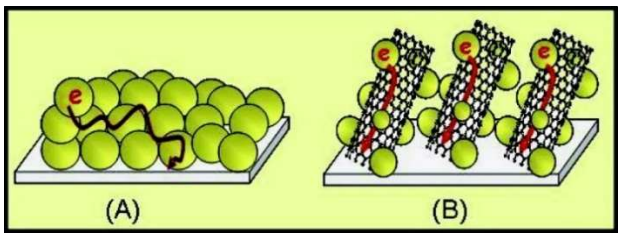

Figure 1-9 Electron transport through pure TiO_2 nanoparticles (A) versus across CNTs (B).[89] Copy right ACS Publications, 2007.

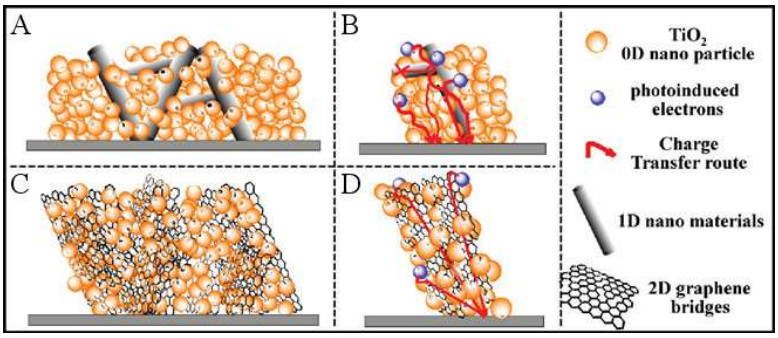

Figure 1-10 Comparison of material loading and electron transport across CNT (a, c) and through graphene sheets (b, d).[88] Copy right ACS Publications, 2010.

The second major application of graphene in DSSCs and DSSC-style PSCs is photoanode additives to improve the ETM performance. The photoanode serves as the overall energy conversion center and thus plays a critical role in the DSSC and DSSC-style PSC. As shown in Figure 1-1, the photoanode is composed of three essential components: a conducting substrate, a layer of semiconducting material, and sensitizers. Although it is still challenging to mass produce high-quality graphene at low cost, researchers can add a small number of graphene sheets as additives to semiconducting materials to enhance the electron transfer process in the photoanode. Similar works have been widely tested on CNTs and resulted in around 100% current increase.[88,89] Without carbon material support, electrons that are injected into TiO_2 nanoparticles or other nanostructures may transfer around and need a much longer transfer distance. As shown in Figure 1-9, a CNT provides a faster electron transfer path and significantly reduces the electron-hole recombination

rate in the TiO_2 material layer. Compared with CNTs in Figure 1-10, graphene nanosheets create a much larger surface area to anchor TiO_2 nanoparticles, and the photoinduced electrons can be captured and transferred in a more efficient way.

Yang *et al.*[88] reported that the short circuit current improved from 3.35 mA/cm^2 to 11.26 mA/cm^2 and total efficiency from 0.58% to 5.01% by introducing graphene additives into the TiO_2 photoanode of DSSCs. After synthesizing and reducing GO sheets, the rGO sheets ranged from 0.2 to 2 μm in size (about 1 μm on average). By dispersing TiO_2 P25 into polymer-supported graphene water/ethanol solutions, TiO_2 suspension was prepared for the photoanode formation. Different methods have been developed to improve the compatibility between graphene and semiconducting materials. Some published works are summarized and compared in Appendix A:. Bell *et al.*[90] and Wang *et al.*[91] studied the promoting effects of rGO and graphene additives, respectively. Wang's work clearly showed that the electron lifetime decreased from 17.6 ms to 6.4 ms by adding graphene, and ~0.7 wt.% graphene addition led to the highest efficiency. When the graphene ratio is lower than 0.7 wt.%, more graphene can further improve the electron transfer process; however, when the graphene is over 0.7 wt.%, more graphene in contact with TiO_2 may create more chances for recombination. He *et al.*[92] and Zhang *et al.*[93] also investigated the TiO_2 particle size effects and the layer thickness effects on electron mobility in graphene-TiO_2 composites. His work showed when the TiO_2 particle size decreases, a more continuous electron transport network is formed, resulting in a higher electron mobility in the smaller-sized TiO_2 based composite electrode.

Some works on planar PSCs using graphene-based materials as ETM also show significant advantages, compared with TiO_2 ETMs, including a lower processing temperature, a lower spectrum effect, and a faster electron transfer.[94] For example, Bi et al.[95] engineered a nanostructure with nitrogen-doped graphene and carbon quantum dots, in an inverted planar PSC. The nanostructure-based PSC demonstrated improved thermal and light stability compared with traditional organic ETMs.

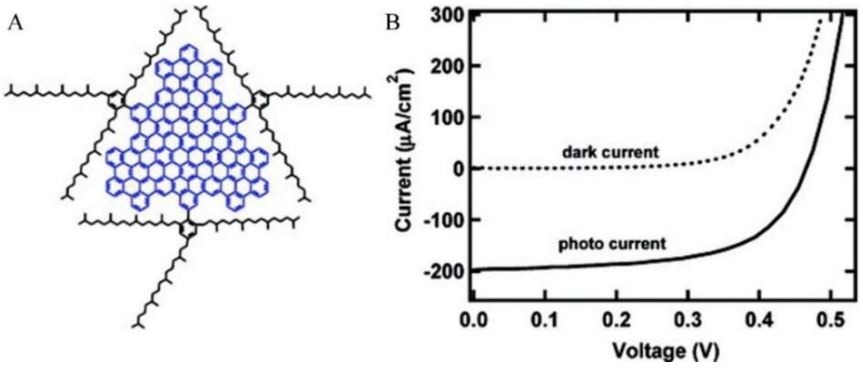

Figure 1-11 (A) Molecular structure of GQD. The graphene moiety is marked blue and the three solubilizing groups are black. (B) The current−voltage characteristics in the dark and under illumination, respectively.[96] Copyright ACS Publications, 2010.

The third important application of graphene in DSSC is to serve as a sensitizing material since a sizeable bandgap can be opened in graphene by quantum confinement. Indeed, as an alternative to dye molecules, sensitizers based on pure graphene have been demonstrated by Yan *et al*.[96] They synthesized graphene quantum dots (GQDs), each of which contains a graphene moiety with 168 conjugated carbon atoms and has an absorption edge of 900 nm. To overcome the insolubility and reduce aggregations common for quantum dots, they attached flexible long chains of 1,3,5-trialkyl phenyl moieties to the edge of the GQD. They used GQDs for the sensitization of TiO_2 in a regular

DSSC. As shown in Figure 1-11B, the DSSC exhibited an open circuit voltage of 0.48 V and a fill factor (FF) of 0.58, while the short circuit current was only 0.2 mA cm^{-2}.

So far, GQDs alone as sensitizers have not achieved a high efficiency; however, as a co-sensitizer, GQDs can significantly improve the performance of common dyes. Lee *et al.*[97] fabricated GQDs by simply oxidizing herringbone-type carbon nanofibers and analyzed the photoluminescence behavior of GQDs mixed with N719 dye at different ratios. The prepared GQDs possess an upconversion PL property to transfer longer wavelength photon energy to the center of highest efficiency of dye molecules and further improves the efficiency. The power conversion efficiency of the solar cell was reported to enhance from 7.28% to 7.95%. Recently, using graphene to create graphene-perovskite hybrids has drawn more attention in PSC research. By introducing graphene to perovskite crystals, new strategies can ensure high PSC performance by controlling perovskite crystallization and the passivation of charge trap states.[94] Hadadian *et al.*[98] introduced nitrogen-doped rGO into mixed metal-halide perovskite absorber and increased perovskite grain size by 150%. The resulted cell showed negligible hysteresis and improved performance compared with pure perovskites. Fang *et al.*[99] also introduced GQDs with a diameter of ~20 nm to reduce the charge recombination in perovskite crystals. The electron exaction time reduced from 1.09 ns to 0.93 ns and overall efficiency was enhanced by 8.2% with respect to pure perovskite cells.

The fourth major application of graphene in DSSCs is to use it as a redox catalyst for counter electrodes. Pure graphene nanosheets are known to have low redox reaction activity. Kaniyoor and Ramaprabhu[100] reported a counter electrode design of thermally exfoliated graphene with a sheet resistance close to that of Pt-based electrodes. The power conversion efficiency (PCE) was about

2.8% for graphene nanosheets compared with 3.4% for Pt. To improve the catalytic performance, functionalized graphene nanosheets (e.g., rGO and graphene with other functional groups) have been widely studied. Roy-Mayhew *et al.* reported the increased oxygen groups on the graphene nanosheets can increase the redox reactivity.[101] Creating a composite or hybrid is a popular option to utilize the high conductivity of graphene with other high activity materials, such as polymers[102,103], metal oxides[104,105], Pt-based materials[106,107], TMD materials[108], and other carbon materials[109]. For example, Zhu *et al.* used electrophoretic deposition to create hybrids of CNT and rGO for counter electrodes in DSSCs.[110] A peak performance with 60% CNT and 40% rGO was observed. Although many studies attempted to produce counter electrode materials that can compete with Pt-based counter electrodes, very few can reach a comparable performance.[111]

Recently, the fifth application of graphene in solar cells has been successfully demonstrated by using graphene-based materials as HTM in PSCs. Arora *et al.*[17] reported a CuSCN based PSC using GO as interface between HTM and gold electrode to retain over 20% efficiency over 1,000 h testing. The GO layer in this cell addresses the charge accumulation between HTM and gold, and significantly extends the life span of PSCs. Furthermore, all carbon-based HTM introduced by Wang *et al.*[112] used CNT/graphene/GO composite, and demonstrated an efficiency of 13.3% with high stability.

1.2.3. Other 2D nanomaterials and their application in solar cells

Other than graphene, many emerging 2D materials have been explored for solar cell applications. Popular materials include hexagonal boron nitride, transition metal dichalcogenides (TMDs), other

Group V and IV hexagonal structures (for example, black phosphorene, silicene and germanene), and other carbon based 2D structures (for example graphdiyne).[113-116]

Among all rising 2D materials, TMDs are attracting more attention for solar cell studies. Firstly, TMDs are relatively easier to prepare in large quantities compared with other emerging 2D nanomaterials. For example, black phosphorene has been reported with outstanding semiconductivity suitable for photovoltaics, but current synthesis methods are limited to high temperature and pressure process with catalysis [117-119] or other high energy density preparation, like mechanical milling process[120]. Secondly, TMDs have relatively stable chemical properties. For example, black phosphorene, silicene, germanene and others can quickly degrade in ambient environment due to oxygen and water vapor.[115,121] Thirdly, TMDs have outstanding semiconducting properties and suitable band structures for photovoltaic applications. Reported by many researchers, TMDs are outstanding options for electrocatalytic applications[122,123], which is important for counter electrodes in DSSCs[124,125]. Also, TMDs can function as sensitizers in a photoanode of a solar cell.[126,127] The advantages of TMDs make it promising for catalytic applications and highlight the necessity to study TMDs for sustainable solar cell applications as well.

TMDs have been studied for catalysis or photovoltaics for a long time. In 1968, Evans and Thompson reported the photovoltage in thin MoS_2 crystals.[128] With the rise of graphene-based materials, TMDs draw attention because of their similar 2D structure and suitable electrical properties, especially the property transition through exfoliation. MoS_2 is the most studied TMD material, and its electron mobility in monolayer is reported at 0.5 ~ 3 $cm^2 V^{-1} s^{-1}$ (theoretical limit

410 $cm^2 V^{-1} s^{-1}$), while in bulk is 200 ~ 500 $cm^2 V^{-1} s^{-1}$, and the record high is 980 $cm^2 V^{-1} s^{-1}$.[129,130] The high mobility is desired for the catalytic performance. Besides that, monolayer MoS_2 is reported to have a Young's modulus of 270 GPa and a current on / off ratio in FET device of 1×10^8, which enables the material for semiconductor applications.[129] Other TMDs having properties similar with MoS_2 are summarized in Figure 1-12.[115]

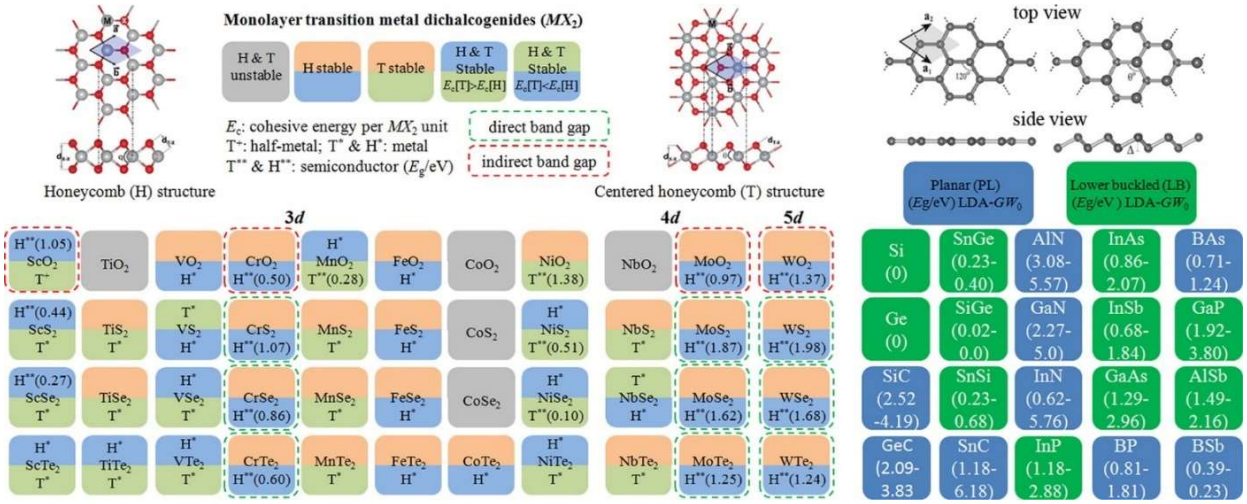

Figure 1-12 Property and stability summary of regular TMD candidates.[115] Copyright to ACS Publications, 2013.

Two significant advantages of TMDs should be noted. First, an indirect bandgap to direct bandgap transition can be observed; for example, MoS_2 has a bandgap of 1.2 eV in bulk and 1.9 eV in monolayer, as shown in Figure 1-13.[115] This transition gives an opportunity to fine tune TMD performance for catalysis by controlling the layer number during material preparation. Second, strain effect is significant on bandgap transition. As shown in Figure 1-14, the band structure changes rapidly with a tuned *a* constant in the MoS_2 monolayer.[115] Based on this property, by creating a heterojunction between MoS_2 and a substrate having different lattice constants, strains can be introduced to MoS_2 crystals, and the bandgaps can be tuned to fit different applications.

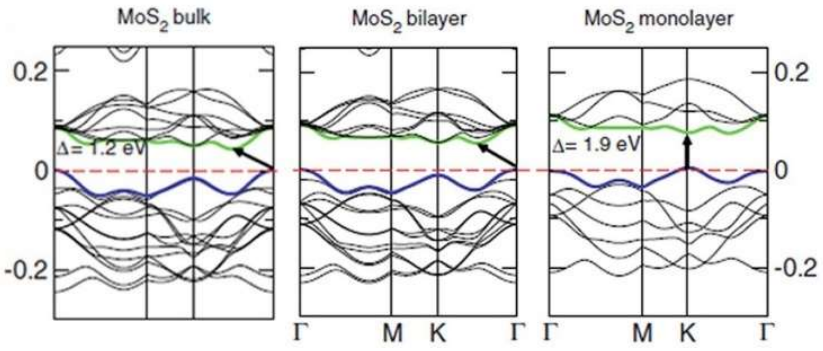

Figure 1-13 Band structure of different types of MoS_2.[131] Copyright to American Physical Society 2011.

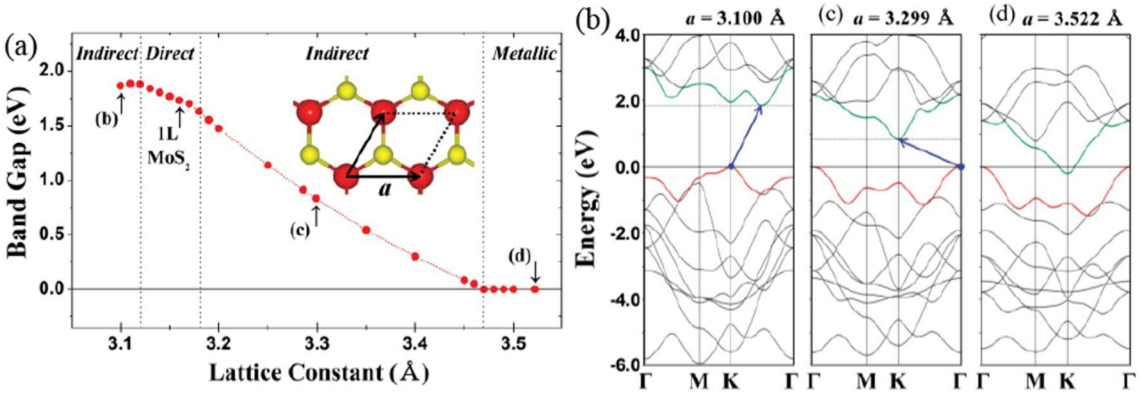

Figure 1-14 Strain effect on MoS_2 bandgap transition.[132] Copyright to American Physical Society 2012.

The outstanding and tunable electronic properties of TMDs make them attractive in solar cells and electrochemical applications. Al-Mamun *et al.* directly grew MoS_2 nanosheets on the FTO glass to use as a counter electrode in DSSCs and found the counter electrode prepared with the $(NH_4)_6Mo_7O_{24}\cdot 4H_2O$ and NH_2CSNH_2 molar ratio at 1:28 gave the highest efficiency comparable to the platinum electrode.[125] Yue *et al.* used a similar hydrothermal approach with glucose as the carbon source and created a hybrid material for the DSSC counter electrode.[133] The as-prepared material yielded an efficiency of 7.69%, which outperformed the standard platinum electrode with 6.74% efficiency. Similar studies used carbon nanotubes or other hybrid structures with TMDs.[124,134,135] The use of TMD materials has provided opportunities to reduce the cost by replacing the high cost platinum and maintain high performance for emerging solar cells.

1.3. Lead recycling and reformation for PSC applications

Lead products play an important role in history. However, the biological toxicity and environmental effects of lead require extra caution for its production, usage and recycling. Nowadays, the major production of lead is used in lead-acid batteries.[136] At the same time, drinking water from aged lead pipelines exposes general public to lead contaminants in daily life. To tackle risks and concerns of lead contamination, effectively recycling and reforming lead contents is essential for the public safety.

1.3.1. Current status of lead recycling from used batteries

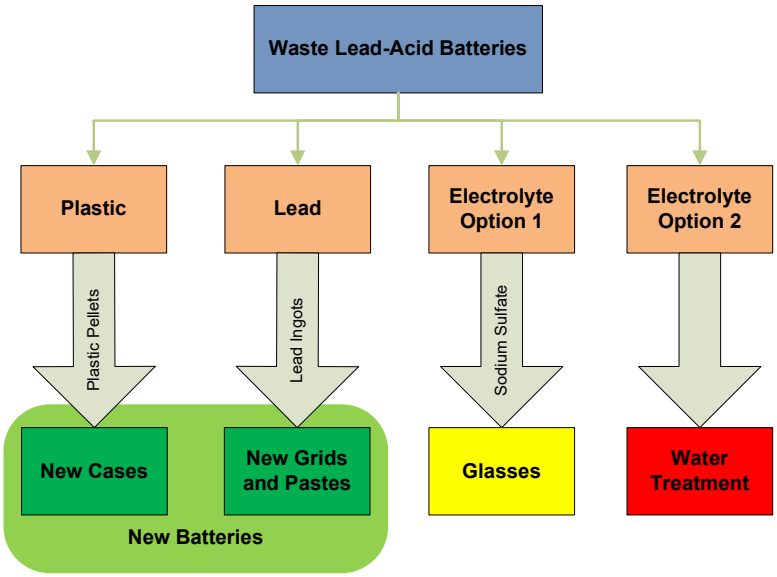

Figure 1-15 Summary of current lead-acid battrry recyling methods.

Lead-acid batteries have been used for over a century in automobiles, and huge amounts of used batteries are collected every year by recycling agencies. Because of the high value of metal lead and environmental concern of the lead-contaminated concentrated sulfuric acid, some recycling

methods have been developed. As shown in Figure 1-15, generally plastic cases and separators in a used battery can be refined and used in new batteries, while electrolytes are in a devalued recycling position or even not recycled. Remanufacturing has been introduced; however, it requires special equipment and the cost is higher than regular manufacturing, since the sulfuric acid concentration of waste acids (lower than 33%) is much lower than that of manufacturing processes (higher than 65%).[137] Neutralization is the major and only practical method to treat acid for recycling or waste deposit, which is impossible to regenerate acid. Product of sodium sulfate has been used in glasses, but the value is greatly reduced and the product always has high-lead-content risk. It is critical to find a new solution to handle concentrated sulfuric acid for lead-acid batteries.

Table 1-1 Comparison of common ion removal methods.

Techniques	Target Contaminates	Removal Rate	Operation Cost	Acid Concentration
Steam method	Any impurities	Close to 100%	High energy cost, high maintenance cost	Functioning at any concentration; benefiting when concentration is higher than 65%
Solvent extraction	Organics	Close to 100%	High maintenance cost	Operating at high concentrations (higher than 65%)
Chemical precipitation and producing other materials	Metal ions and organics	Acid is always not recoverable	Low	Operating at any concentrations
Forced decantation (ion exchanging or membrane filtration)	Metal ions	Depending on pH, initial concentration, time and temperature	Medium	Functioning well at low concentrations (pH from 1)
Adsorption	Metal ions and organics	Depending on pH, initial concentration, time and temperature	Low	Functioning well at low concentrations (pH from 1)
Electrochemical methods	Metal ions	High, but affect acid concentration	High energy cost, high maintenance cost	Suitable for nearly neutral solution

A comparison of common ion removal methods is given in Table 1-1, with green background marking advantage of the method, yellow marking possible issues, and red marking disadvantages. Forced decantation (filtration) and adsorption are two promising methods for acid treatment. Generally, high surface area, easy surface modification and stability in the acid are important requirements for filtration and adsorption ion removal methods. Hence, 2D nanomaterials, especially graphene-based nanomaterials, are great candidates for ion removal in concentrated sulfuric acid.

1.3.2. Current status of lead removal in drinking water systems

In drinking water systems, Pb^{2+} is frequently detected and can cause long-term health risk to people.[138,139] In US, the total lead concentration allowance in the drinking water is 15 ppb according to US Environmental Protection Agency (EPA)[140]; and the World Health Organization (WHO) has set the limit to 10 ppb, as well as many countries.[141] However, the aging lead pipelines in most municipalities sometimes leads to an unacceptable Pb^{2+} concentration, when water reaches households. The water crisis in Flint, Michigan starting in 2014, has driven a high demand for low-cost lead removal methods in drinking water.[142] With lead pipelines used widely in drinking water supplies, as well as lead contamination happening around the world in the water body, creating a selective removal method to reduce lead in water is crucial for human safety.

Currently, many water treatment technologies are widely studied and applied to purify water for drinking water system. Chemical treatment is the most widely used and robust method for common decontamination and disinfection.[143,144] However, when treating low concentration Pb^{2+}, this

method is limited by both the cost of chemicals and the low removal rate. Ion exchange, adsorption, ultrafiltration and reversed osmosis are widely studied and used to address this issue with commercial products available.[145] But the high maintenance cost and high-energy consumption limits the feasibility for low-cost daily use. Capacitive deionization (CDI) is an emerging energy-efficient water treatment technique to remove salt[146], heavy metal ions[147], and hardness[148] from water. In recent years, the efficiency of CDI has been significantly improved, and some commercial plants are constructed or already in use. Fundamentally, a CDI device is a capacitor. As shown in Figure 1-16, with or without ion exchange membranes, CDI cells use an electric field to separate ions. By applying voltage, double-layer capacitance can be built on electrodes in CDI devices, which attracts, accumulates, and removes ions. When the voltage is reversed or sets at 0 V, accumulated ions are discharged into a smaller volume effluent at a higher concentration.

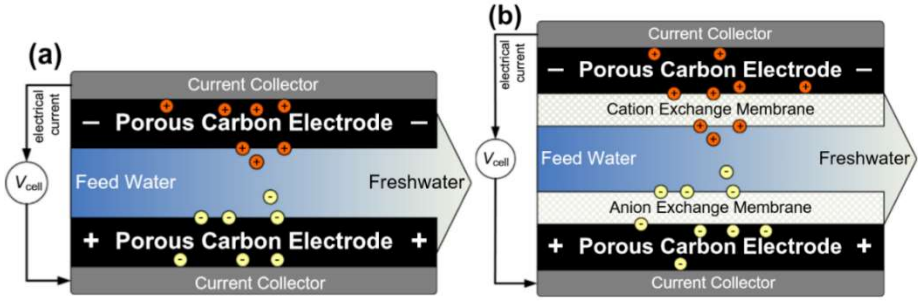

Figure 1-16 CDI theory schematic.[149] Copyright to Elsevier 2013.

Recycling methods for Pb^{2+} removal always require low cost, high surface area, flexible chemical modification and high conductivity, which are properties of 2D nanomaterials, especially graphene-based nanomaterials. Applying 2D nanomaterials can enhance the lead recycling efficiency and create future reformation possibilities.

1.3.3. Lead recovery and reformation for solar cells

Studies have shown lead plays a critical role in PSCs, which is the metal core of the perovskite crystal. Methods of refining solid lead from waste batteries have been developed for solar cell use.[150,151] This gives possibility to collect lead contaminants from waste acid and contaminated water and refine for solar cell study. As summarized in Figure 1-17, 2D nanomaterials make it possible to collect lead ions from waste acid from lead-acid batteries, as well as lead contaminants from drinking water. This process also enables the transformation of using lead for PSCs, reduces the stress of accumulating lead waste from retiring lead-acid batteries, reduces the risk of the secondary contamination to water body on earth, and creates a possibility of sustainable solar cell manufacturing.

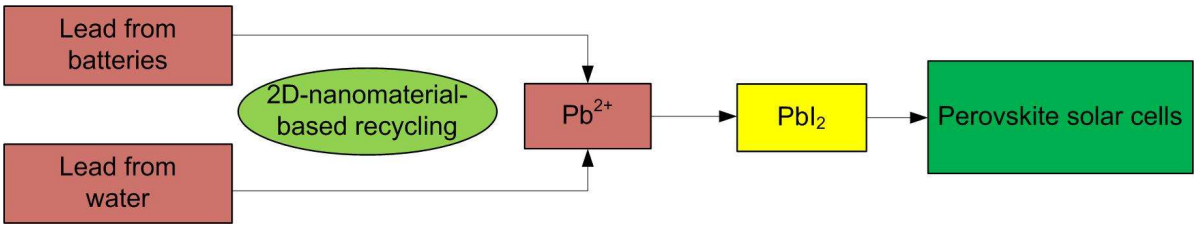

Figure 1-17 Summary of proposed lead footprint.

1.4. Research objective

This study starts with basic understanding of current solar cell research and recent advancement of 2D nanomaterials, and then explores applications of novel 2D nanomaterials based on their physical and chemical properties for emerging sustainable solar cell fabrication. With understanding of 2D material properties and their potential applications for solar cells, the dissertation aims to explore fabrication of solar cells with a lower cost but improved performance

and environmental sustainability. Therefore, the dissertation is organized based on the following tasks:

Task 1: Reduce cost of DSSCs by replacing Pt-based counter electrodes with 2D nanomaterial hybrids (Chapter 2).

Benefiting from the high conductivity of graphene and high catalytic performance of MoS_2, counter electrodes made of graphene-MoS_2 hybrids are prepared for DSSCs with a lower cost. Both graphene and MoS_2 have been extensively studied for catalytic applications, but the property tuning in the hybrid material is essential to explore. With a temperature-controlled hydrothermal method, different crystallization processes of the hybrid material can be compared. The physical and chemical property change in the process can be further understood.

Task 2: Investigate current PSC limitations and explore possibilities to improve PSCs with 2D nanomaterials (Chapter 3).

The optimized preparation of solar cells is required to use 2D nanomaterials in future applications. Using PSCs as a candidate, the critical requirements can be amplified by preparing semi-transparent solar cells. By studying the absorbance, crystallization and stability, the semi-transparent PSCs can be well prepared, and the understanding can assist better design of PSC fabrications in future research.

Task 3: Reduce HTM cost and improve stability for PSCs with 2D nanomaterial hybrids (Chapter 4).

The high cost and low stability of current HTMs in PSCs can be addressed by incorporating 2D nanomaterials into HTMs. Employing GO nanosheets as a charge transporter to inorganic HTMs, a low-cost and high-stability HTM alternative can be prepared. The feasibility study on 2D nanomaterials can increase the commercial potential of current PSCs as the next-generation energy source.

Task 4: Investigate lead recycling from waste sulfuric acid with 2D nanomaterials to reduce the PSC material cost and address environmental concerns (Chapter 5).

With better understanding of material properties, an environmentally friendly fabrication method for PSCs is possible. The physical and chemical properties of 2D nanomaterials and their hybrids can be utilized for heavy metal ion collection from waste sulfuric acid. Graphene and TMDs can be functionalized with active selective groups to lead ions, and the selectively removed lead from wastes can be chemically recovered into perovskite solar cell precursors. This attempt can lead to an increased value of wastes, and reduce the environmental concern at the same time.

Task 5: Explore lead recycling and reformation from contaminated water with 2D nanomaterial based capacitive deionization to increase commercial value of PSCs (Chapter 6).

The functionalized 2D nanomaterials can be used in lead collection from lead-contaminated drinking water. The collected lead ions in water can also be recovered and used in perovskite solar cells. This environmentally friendly approach can not only address general public concerns and prevent the secondary contamination to water body on earth, but also reduce cost of perovskite material and increase value of water treatment technology.

The study contributes to green PSCs and high-performance DSSCs and PSCs with a lower cost. By incorporating the 2D nanomaterials into the solar cell fabrication, the solar cell performance can be significantly improved; at the same time, by using 2D nanomaterials, lead ions can be environmentally friendly recovered and refined to PSC precursors.

Chapter 2. MoS_2-Graphene Hybrid Materials for DSSC Counter Electrode

2.1. Introduction

2D hybrid materials have been studied for use in photovoltaics, water splitting, sensors, batteries, and many other applications, often in the form of heterojunctions or 3D frameworks.[115,152-156] Benefiting from their unique 2D structures and tunable band-gaps, 2D hybrid materials can offer both a high specific surface area and a suitable work function.[115,157-160] For most electrochemical applications, such as in DSSCs and hydrogen evolution reactions (HERs), the high electronic conductivity and the strong redox reactivity of TMDs/graphene hybrids are extremely attractive. In these hybrids, graphene nanosheets possess high electronic conductivity and mechanical strength,[44,161] and serve as growth centers for TMD nanosheets. Earlier studies have shown that the hybrid structures offer enhanced catalytic activity with more active sites.[162]

Compared with traditional Pt-based catalyst materials, 2D hybrid materials offer a comparable performance and a much lower production cost, thus demonstrating their great potential to replace Pt for commercial use. Until now, the MoS_2/graphene hybrid has been studied as one of the most promising options because of its excellent electrocatalytic activity and unique 2D structure.[153,163,164] It is well known that poor intrinsic conductivity limits the overall electrocatalytic performance of pure MoS_2[123,165] and that the reactivity of pure graphene is relatively weak.[41,60,166] The MoS_2/graphene hybrid combines the benefits of reactivity and conductivity of the two constituent materials, thereby leading to significantly enhanced electrocatalytic performance.[116,167] Because both the composition and the structure of catalysts affect the material reactivity, it is important to create more active sites and maintain high conductivity when designing a hybrid. By choosing appropriate methods to tune the binding

between the two component structures, the resulting catalytic performance can be further optimized.

In recent years, hydrothermal methods have been widely studied as a low-cost and high-throughput route for synthesizing MoS_2/graphene hybrids. Previous research has reported that the crystallization of pure MoS_2 could change significantly at different reaction temperatures, with amorphous MoS_2 nanospheres at low temperatures (120-150 °C), flower-like MoS_2 balls with a high catalytic performance at mid-range temperatures (160-240 °C), and large MoS_2 nanoparticles at high temperatures (230-260 °C).[168,169] However, when the seed of crystallization changes to graphene, the crystallization condition of MoS_2 is not well understood, and thus further understanding of the crystallization condition is needed to optimize the material catalytic activity. In this work, we use a facile hydrothermal method to prepare MoS_2 nanoflakes grown onto graphene nanosheets at different mid-range temperatures. MoS_2 crystallization on graphene nanosheets can be clearly identified by various crystal characterization methods, and the effects of the crystallization on the resulting catalytic performance are studied by DSSC performance and HER reactivity.

2.2. Experimental methods

A series of MoS_2/graphene hybrids were prepared by the hydrothermal method. Carbon powders for GO synthesis was purchased from Bay Carbon, Inc. (Part No.: SP-1). Commercial TiO_2 paste SA (Part No.: Ti-Nanoxide T/SP), iodine electrolyte (Part No.: Iodolyte HI-30) and thermoplastic sealing film (Part No.: Meltonix 1170-25) were purchased from Solaronix. All other materials were purchased from Sigma-Aldrich.

Graphene oxide nanosheets were prepared per published procedures from a modified Hummer's method.[170] After washing and drying the as-prepared GO at 65 °C for 48 h, the solid flakes were then exfoliated and reduced by microwave at 900 W for 90 s under an argon environment; this process also reduced the graphene oxide.[171]

To prepare the MoS_2-graphene hybrids, 10 wt.% graphene (2.8 mg) was dispersed in 20 mL DI water by ultra-sonication at 250 W for 30 min. Then, sodium molybdate dihydrate ($Na_2MoO_4 \cdot H_2O$, 42 mg) was added in and stirred for 30 min to be well-absorbed onto the MEGO surface. Finally, thiourea ($SC(NH_2)_2$, 84 mg) was added and stirred for 30 min, and excessive thiourea was added to the solution to further reduce MEGO.[153] The suspension was then transferred to 50 mL autoclaves for hydrothermal reactions at temperatures of 150 °C (MG-150), 180 °C (MG-180), 210 °C (MG-210), and 240 °C (MG-240) for 24 h. After synthesizing, obtained suspensions were transferred to 50 mL centrifuge tubes. The solids were separated after standing steadily for one day and then the suspensions were centrifuged at 11,000 rpm for 40 min. The MoS_2/graphene hybrids were obtained after washing with DI water three times and then dried under vacuum at 70 °C overnight.

The structure of prepared materials was studied with a Hitachi (S-4800) field-emission scanning electron microscopy (FE-SEM). The energy-dispersive X-ray spectroscopy (EDS) mapping data were obtained using a Bruker detector on the Hitachi S-4800 FE-SEM. A Hitachi (H 9000 NAR) transmission electron microscope (TEM/HR-TEM) was used to study the hybrid junction of the MoS_2/graphene hybrid prepared at 180 °C. XRD was carried out using a Bruker D8 Discover X-

ray diffractometer. Raman spectroscopy was taken with a Renishaw Raman spectrometer (Inc 1000B) with an He-Ne laser (633 nm).

2.3. Results and discussion

2.3.1. Material characterization

Figure 2-1a-h shows FE-SEM images of the MoS_2 structure grown on the graphene surface. The perpendicularly-oriented, flower-like MoS_2 nanoflakes were observed at all temperatures and the uniform coverage was proven by EDS element mapping (Figure 2-2). As shown in Figure 2-1 a-d, the MoS_2 nanoflakes grew bigger with the increasing synthesis temperature. Observed under a low magnification as shown in Figure 2-1 e-h, the coverage of MoS_2 nanoflakes is significantly larger, as the MG-240 hybrid started losing the layer-by-layer feature and began forming the nanoparticles, while the MG-210 hybrid loosely maintained the layered structure. Previous studies have shown that the edges of nanosheets are active sites for catalytic reactions, suggesting that edges, defects, and kinks are responsible for high catalytic performance. Therefore, highly branched morphology is preferred for most catalytic applications.[152,172]

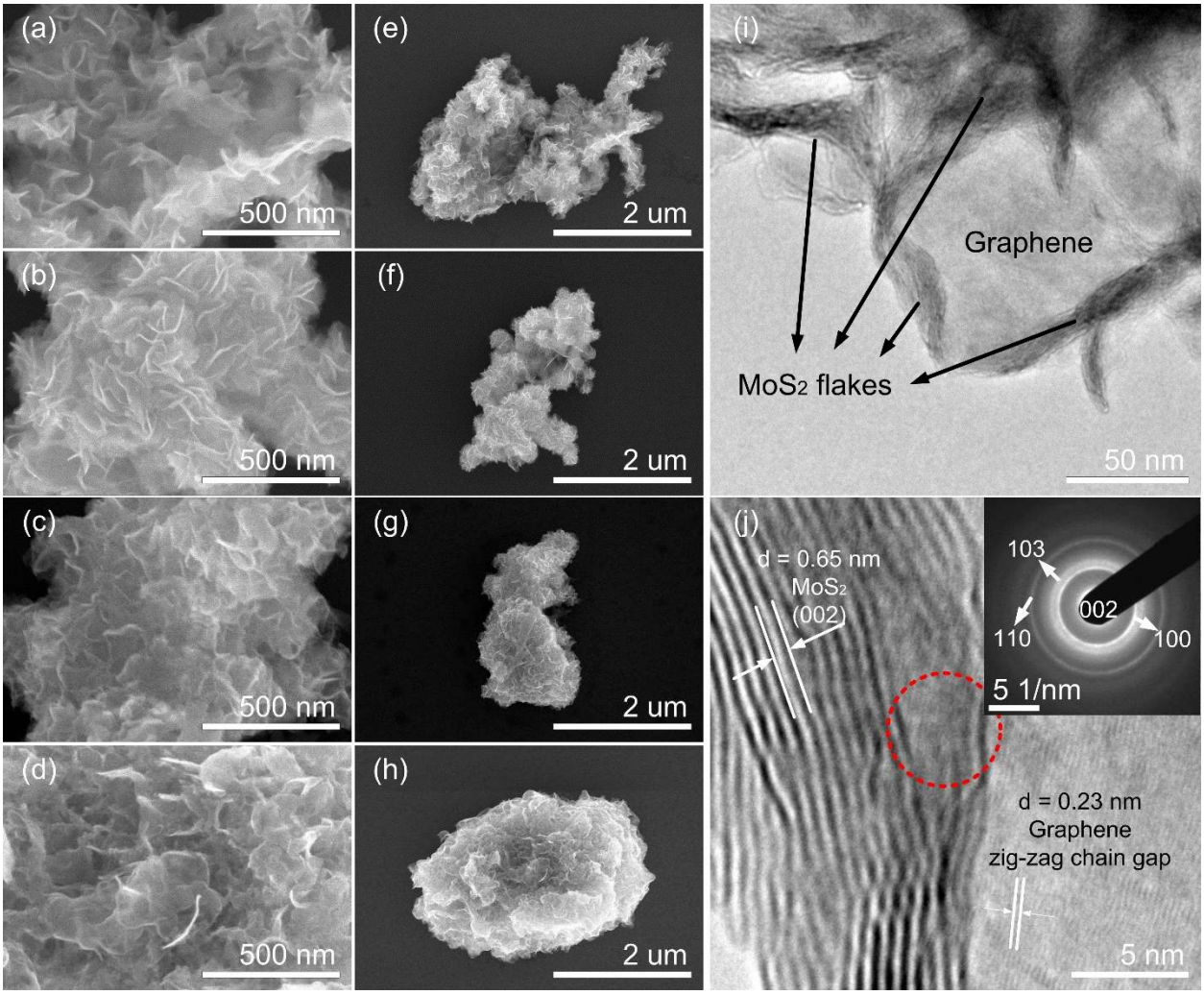

Figure 2-1. FE-SEM images of MoS_2/graphene hybrids at 150 °C (a, e), 180 °C (b, f), 210 °C (c, g), 240 °C (d, h), and TEM and HR-TEM images of the MoS_2/graphene hybrid at 180 °C (i, j). The inset of (j) is the corresponding SAED pattern marked by the dashed circle. Lattice information is marked in (j).

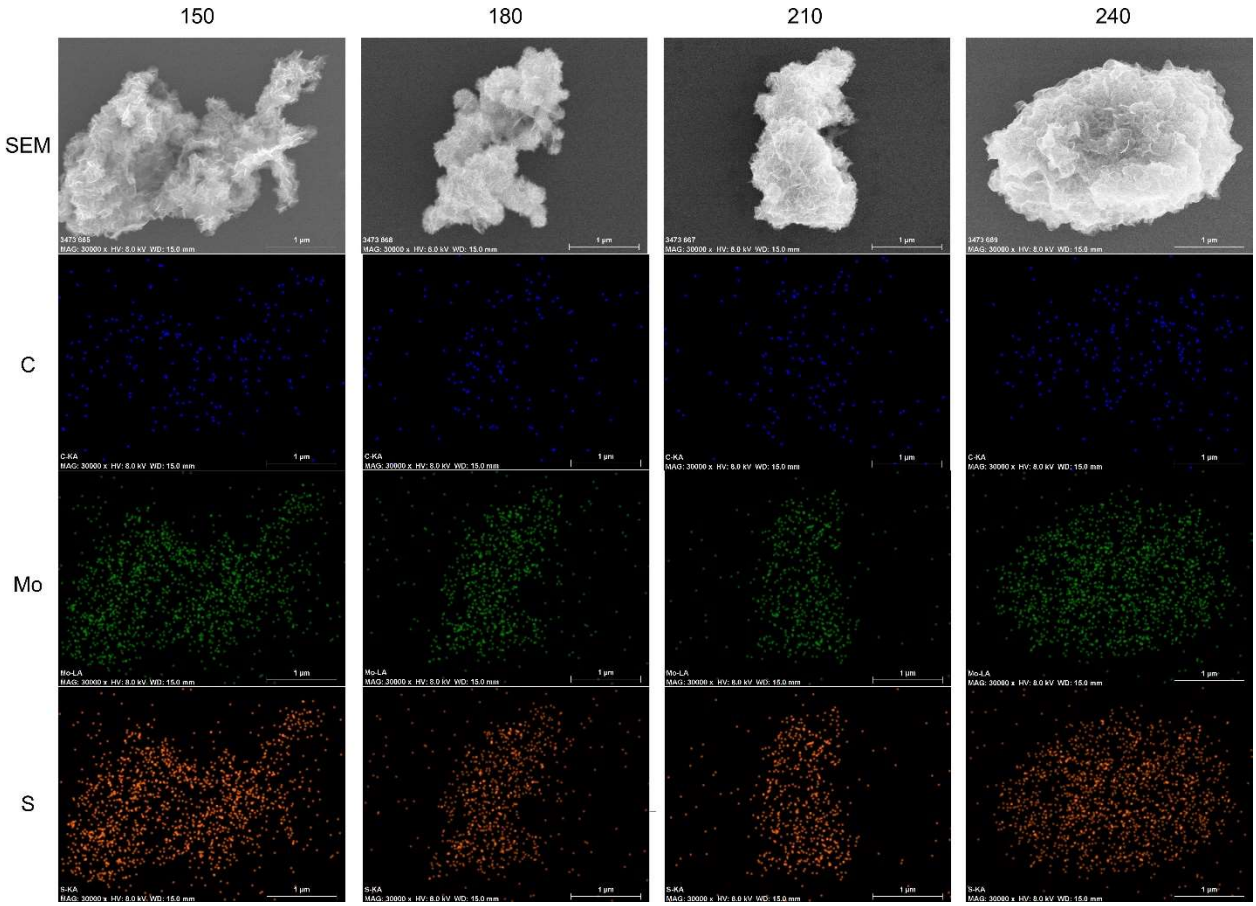

Figure 2-2 EDS results with FE-SEM images for four samples at each temperature. The distributions of C, Mo, and S elements are uniform, proving the complete coverage of MoS_2 on a graphene surface.

To gain further insights into MoS_2/graphene hybrids, TEM and high-resolution transmission electron microscopy (HRTEM) images were obtained and analyzed. Using an MG-180 hybrid sample to study its branch structure, a laminar structure of MoS_2 (crossing black stripes) loaded on the surface of graphene (a flat gray area) was observed, as shown in Figure 2-1i. Zooming to the center of Figure 2-1i, two different types of crystals are clearly observed in the HR-TEM image by their significantly different lattice spacings (Figure 2-1j). The lattice spacing of 0.65 nm matches well with that of MoS_2 in 2H-crystal (002) face, and the 0.23 nm lattice spacing is close to that of the zig-zag chain gap in a single-layer graphene nanosheet[173]. The few-layer MoS_2

nanosheets crossed over to each other in the small area, representing the formation of small nanoflakes and the creation of edges and defects. The seamless stitching of the graphene nanosheet to MoS_2 nanosheets, marked by the dashed circle in Figure 2-1j, also was studied by selected area electron diffraction (SAED). Several diffraction rings can be well indexed to the planes of 2H-MoS_2, with graphene diffraction not clearly shown due to the smaller quantity. The intimate contact of the two types of crystals suggests an efficient electron transfer within the hybrid.

To gain deeper understanding of the crystallization change at different reaction temperatures, the X-ray diffraction (XRD) and Raman spectra of the MoS_2/Graphene hybrids (Figure 2-3) were studied. Overall, the as-prepared hybrids showed a 2H-MoS_2 phase. The flat XRD pattern from 10 to 35° of MEGO was caused by the stacking of nanosheets while in storage. For the MG-150, MoS_2 peaks were not clearly visible because of the limited amount of crystal formation on the graphene nanosheets. When the temperature was increased, the XRD peaks sharpened and a small angle shift was observed between 30° and 55°. The peaks of the MG-180 hybrid stand out due to the weak peaks for (103) and (105) of the 2H phase, the broadened and shifted (100) peak, and, importantly, an additional (006 + 104) peak. The rearrangement in the crystals indicates possible 1T phase existence.[174] The weak signals from the MG-150 showed poor crystallization quality, which indicates more defects. Similar trends also can be observed by Raman spectra (Figure 2-3b) with helium-neon laser exciting at 633 nm. MG-150 and MG-180 gave extreme weak MoS_2 Raman signatures, because of poor crystallization quality. The intensity of A_{1g}, $E_{2g}{}^1$ and E_{1g} peaks increased with the increasing temperature. Also, the out-of-plane Mo-S phonon mode (A_{1g}) is preferentially excited for the edge-terminated perpendicular orientation of MoS_2 nanosheets, and the high intensity of A_{1g} shown in the MG-210 and MG-240 hybrids indicates the perpendicularly-

oriented structure formed on graphene nanosheets.[152] The C peaks come from the second order longitudinal acoustic mode at the M point (2LA(M)) of the MoS_2 Brillouin zone, which indicates improved crystallization quality at high temperature[175]. Another interesting observation is the increased intensity of the D to G band (I_D/I_G) of graphene with increasing temperatures, as shown in Figure 2-3b. This indicates a stronger van der Waals interaction between MoS_2 nanosheets and graphene nanosheets, which enhanced the breathing mode of the hexagonal ring of graphene.

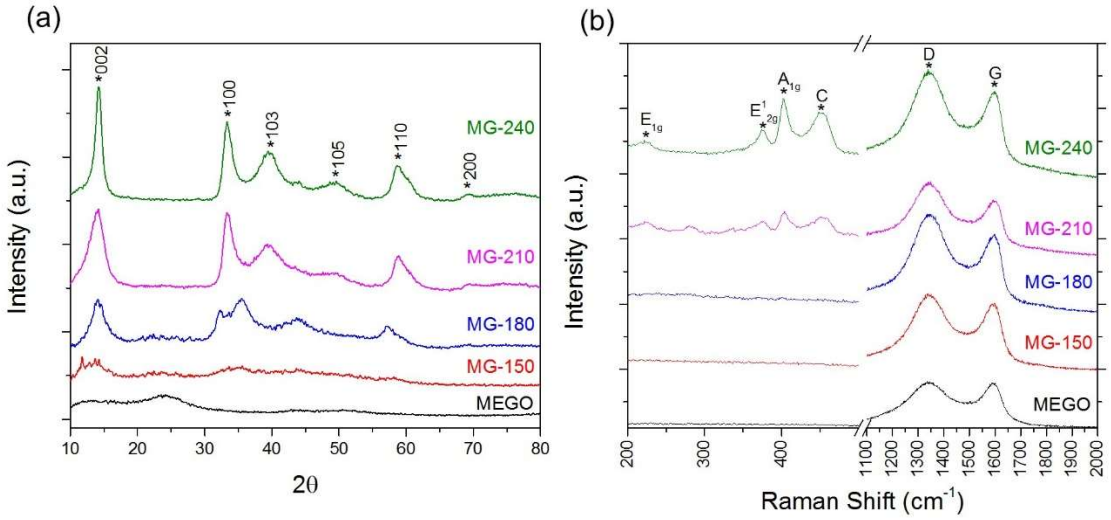

Figure 2-3. (a) XRD spectra of MoS_2/graphene hybrids prepared at 150 °C, 180 °C, 210 °C, and 240 °C compared with MEGO; (b) Raman spectra of MoS_2/graphene hybrids and MEGO. 2H peaks of MoS_2 are labeled in the patterns.

Additional study using X-ray photoelectron spectroscopy (XPS, Figure 2-4) also proved the improvement of crystal quality and phase transition with the increase of temperature. The sharpening peaks from MG-150 to MG-240 indicates the crystal improves from a poly-state to a crystalized state. Also, a graduate shifting of the Mo 3d peaks can be observed from MG-180 to MG-240, and the binding energy of MG-180 appears ~0.63 eV lower than that of MG-240. This indicates that the possible crystal phase change from 1T to 2H occurs from 180 °C to 240 °C.[174,176]

The peak positions of MG-150 are close to MG-210, which can be explained by the broad peaks with more lattice defects, and the loosely organized structure plays a more important role. Summarizing XRD and Raman data, both crystallization quality and phase transition are two notable factors by temperature variation in MoS_2/graphene hybrids hydrothermal preparation.

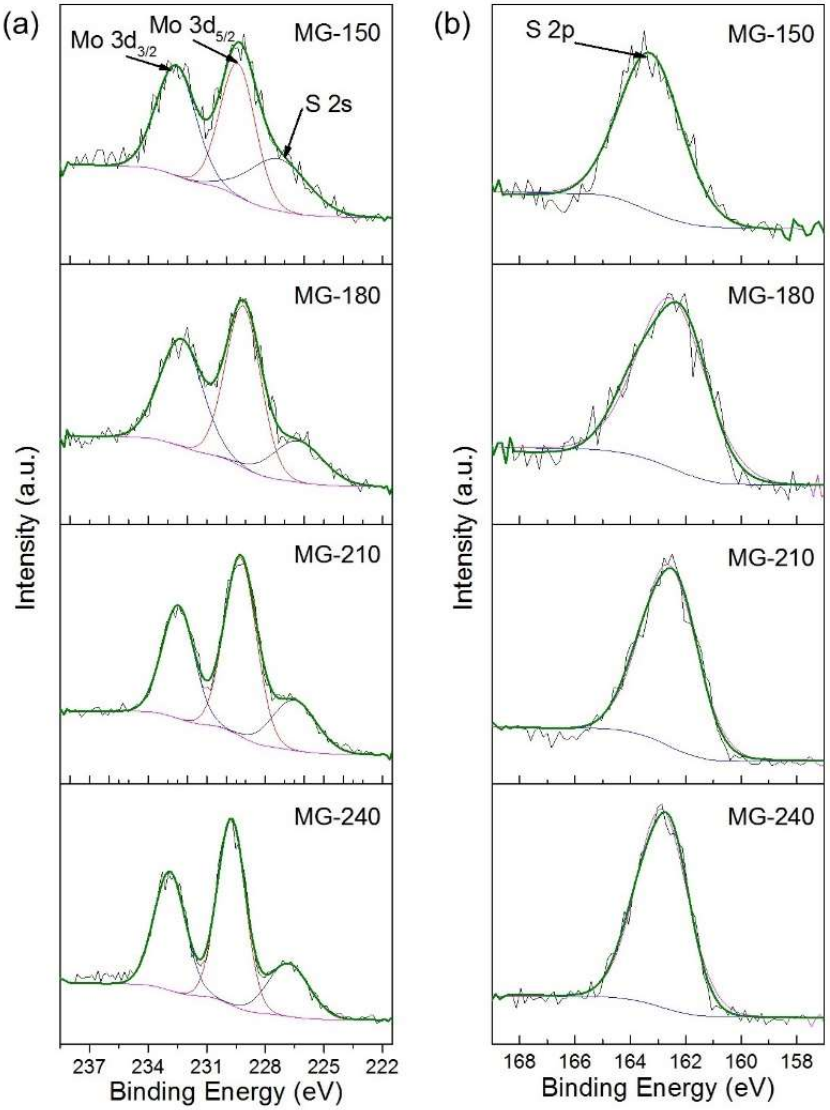

Figure 2-4 XPS spectra of MoS_2/graphene hybrids prepared at 150 °C, 180 °C, 210 °C, and 240 °C, with (a) focuses Mo 3d orbits and (b) shows S 2p orbits.

Earlier investigations acknowledge that defects in crystals can increase catalytic reaction rate, and the 1T phase of MoS_2 is always preferred. However, a significantly worsen crystal quality leads to poor charge transfer and lower catalytic performance.[123,177] It is necessary to determine a preferred temperature to balance the factors. Earlier investigations studied the mechanism of MoS_2 formation, and the analysis is applicable here as well.[161,178] Firstly, thiourea dissociates to free thiol groups and amino groups and reduces Mo(IV) and partially reduces GO; secondly, the free radicals adsorb onto reduced GO surface and start forming MoS_2 crystals along (002) face based on HRTEM results; defects are easier to form at low temperature due to lower chemical kinetics, which exposes vacant Mo or S to the environment. A density functional theory (DFT) calculation shows that reduction reactions are tend to happen along Mo-Mo grain boundaries rather than point defects in lattice,[179] and the Mo-Mo grain boundaries are more abundant in low-temperature prepared defect-rich hybrids. The importance of 1T phase of MoS_2 for catalytic reactions has also been studied for pure 2D crystals. Earlier DFT calculations suggest the 1T-MoS_2 shows metallic properties and has a significantly higher catalytic reactivity compared with semiconducting 2H-MoS_2.[174,176,180] Studies also indicate the strong dependence of the crystal formation on temperature.[181] Pure 1T-MoS_2 nanosheets are always prepared by chemical exfoliations by alkali metal,[174] to obtain a higher ratio of 1T phase. Considering the costs and stabilities of 1T phase, hydrothermal methods are more suitable for catalytic reactions, which typically require ~220 °C to have the best efficiency for pure MoS_2.[169] MoS_2/graphene hybrids in this work show lower temperature requirements at 180 °C, and this can be explained by the faster seeding process with graphene as supporting media and crystal constant alignments during crystallization. A first-principle study of MoS_2/graphene heterojunction shows that the work function of graphene (4.3 eV) matches well with the conduction band (4.2 eV) of monolayer MoS_2, and the calculated charge

carrier density in MG hybrids is over 3 orders of magnitude higher than the intrinsic value of graphene. Furthermore, the electron-hole pairs are well separated in the structure, which promotes a higher reactivity.[167,182,183]

2.3.2. Catalytic performance comparison

The electrocatalytic activity of MoS_2/graphene hybrids was first investigated in DSSCs. DSSCs have a sandwich structure with a sensitizing material-coated semiconducting layer as the photoanode, a pair of redox as the electrolyte, and a reducing catalyst as the counter electrode.[184] A DSSC has a separate photoanode and a counter electrode, which creates an opportunity to maximize the counter electrode catalyst without breaking the cell chemistry. By applying the MoS_2/graphene hybrid as the counter electrode in DSSCs, both the conductivity and the catalytic reactivity relevant to its electrochemical properties can be directly characterized.

In this work, we prepared N719-sensitized TiO_2-based photoanode, I_3^-/I^- electrolyte, and MoS_2/graphene hybrid counter electrodes for DSSC measurements, as shown in Figure 2-5(a). The J-V characterization was conducted under a simulated one sun illumination (AM 1.5G, 100 mW/cm^2, Newport, 94021A) with a Keithley 2420 source meter. The system was calibrated with an Si-reference cell (Oriel, P/N 91150V). To prepare DSSCs, first, FTO glasses were sequentially cleaned with acetone, isopropyl alcohol, and DI water. Then, the glass blades were fixed onto the bench with Scotch® tape and a commercial TiO_2 paste was doctor-bladed onto the surface. After gradually heating to 500 °C over 30 min, the substrates were treated in a 40 mM $TiCl_4$ aqueous solution for 30 min at 70 °C, and then dried at 500 °C for 30 min. After cooling down to room temperature, the substrates were transferred to 0.5 mM N719 ethanol solution and soaked for 24

h. Detailed steps can be found in earlier publications.[185] The counter electrodes were also fabricated by the doctor-blading method. First, a 20 mg sample and 5 μL Triton x100 were dispersed in 500 μL DI water. Then the obtained slurry was bladed onto a clean FTO surface and then annealed at 500 °C for 30 min in an argon environment. Pt-based counter electrodes were fabricated by blading 0.01 M H_2PtCl_6 ethanol solution with the same steps. To assemble the cell, the prepared counter electrodes and photoanodes were sealed with commercial thermoplastic sealing film, and then a commercial electrolyte was injected into the cells.

The solar cell performance is summarized in Table 2-1 and compared in Figure 2-5(b). Both MG-150 and MG-180 hybrids showed a significantly improved response compared with hybrids obtained at higher temperatures. All catalysts maintained the open-circuit voltage (V_{OC}) at around 0.7 V, which is close to that of the Pt-based catalyst, while the short-circuit current (i_{sc}) dropped to 8.47 mA/cm^2 for MG-210 and 7.71 mA/cm^2 for the MG-240 hybrids. The increased FF for high temperature hybrids results from the lower i_{sc} and V_{OC}. It is clear that i_{sc} is the dominating factor to reach higher efficiency, which is dependent on fast charge transportation in the hybrids. Comparing the MG-150 and MG-180 catalysts, the MG-180 hybrid gave a higher i_{sc}, which suggests either a better conductivity or a higher reactivity, and agrees with weaken charge transportation prediction by excessive defects in MG-150 hybrid. The low performance of the MG-240 hybrid is predictable because of the over-stacking of MoS_2 nanosheets, shown in FE-SEM images of Figure 2-1, which limits the electron transfer between the graphene and MoS_2 crystals.

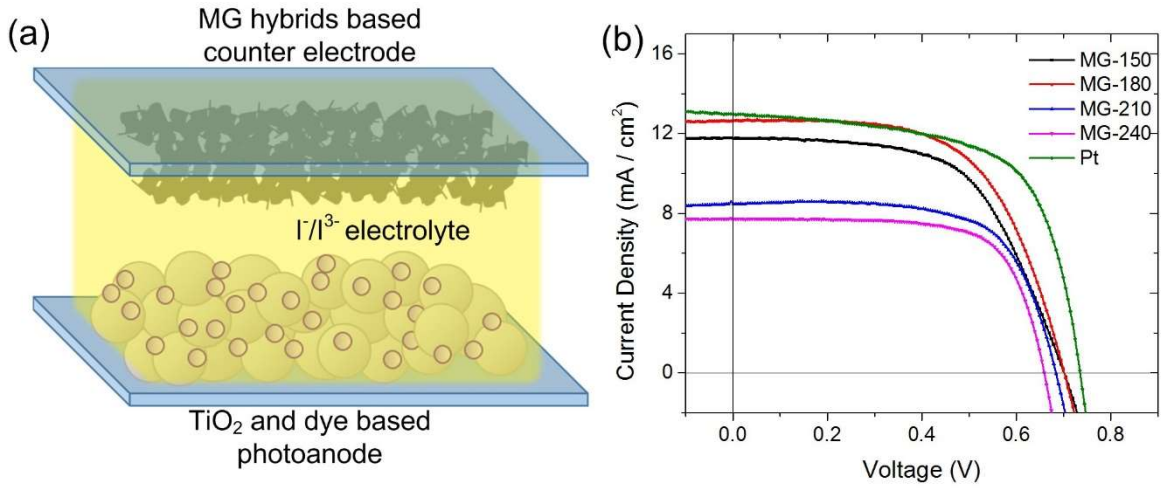

Figure 2-5. (a) Schematic of the DSSC with as-prepared hybrids as counter electrode catalyst. (b) J-V curves of DSSCs with MoS_2/graphene hybrids as the counter electrode. The Pt-based counter electrode showed the best performance while the 180 °C hybrid was close to that with a lower FF. V_{OC} started dropping when the preparation temperature increased to 210 °C and 240 °C.

Table 2-1. DSSC performance data comparison.

Counter Electrode	V_{OC} (V)	i_{SC} (mA/cm^2)	FF (%)	Efficiency (%)
MG-150	0.700	11.7	59.2	4.87
MG-180	0.701	12.6	60.4	5.34
MG-210	0.683	8.47	67.4	3.90
MG-240	0.659	7.71	70.2	3.57
Pt	0.735	13.0	64.0	6.10

To further understand the improved performance of the MG-180 hybrid in DSSCs, the conductivity and reactivity must be investigated separately. To study the electrochemical properties, the MG-150, MG-180, and MG-210 hybrids were chosen to measure the HER performance in a three-electrode setup. All measurements were carried out in 0.5 M H_2SO_4 aqueous solution using a CHI 760D electrochemical workstation. Tests were performed in a

standard three-electrode glass cell, with the Pt wire as the counter electrode and glassy carbon electrode (GCE). To fabricate GCEs, 5 mg of material was mixed with 50 μL Nafion® ethanol solution (5%) and 450 μL DI water. The mixture was well dispersed and a 5 μL suspension was dropped onto a glassy carbon electrode with a diameter of 3 mm and then fully dried. All HER tests were operated in the 0.5 M H_2SO_4 aqueous solution using a saturated Ag/AgCl electrode as the reference and Pt wire as the counter electrode. The electrochemical performance of samples was tested by fabricating glassy carbon electrodes with a controlled diameter of 3 mm and the tested potentials were converted to the reversible hydrogen electrode (RHE) scale via the Nernst equation. The linear sweep voltammetry (LSV) was tested from 0.2 to -0.8 V (vs. Ag/AgCl) at 5 mV/s; later the Tafel plot was calculated from LSV. Cyclic voltammetry (CV) was scanned between -1 V and 1 V (vs. Ag/AgCl) at 0.05 V/s. The electrochemical impedance spectroscopy (EIS) was measured at a frequency ranging from 0.1 to 10,000 Hz at a constant potential 0.5 mV (vs. Ag/AgCl). The stability was evaluated for 20,000 s at a constant potential -0.5 V (vs. Ag/AgCl).

The MG-150 and MG-180 hybrids gave very close onset potentials of about -176 mV and -179 mV, respectively, and the MG-210 showed an onset potential about -287 mV, estimated from the low-current density region in the LSV (Figure 2-6a). The shaking tail of the MG-180 hybrid at a lower potential was caused by the generation and accumulation of hydrogen bubbles, which suggests the high performance of the MoS_2/graphene hybrid. The Tafel plots (Figure 2-6b) of the three catalysts show a 74.5 mV/decade slope for the MG-180 hybrid, which is much lower than those of MG-150 and MG-210, indicating a faster increase of the HER rate with increasing overpotentials. The better performance of the MG-180 hybrid over the MG-150 hybrid explains the importance of better crystallization for charge transfer. This can be observed by EIS analysis

(Figure 2-8). The MG-180 hybrid exhibited a smaller semicircle, indicating more efficient charge transfer between graphene and MoS_2. Meanwhile, the impedance of the MG-180 hybrid quickly increased, presenting the possibility of higher porosity of the same mass of materials. BET (Brunauer–Emmett–Teller, Figure 2-9) tests indicated that MG-180 has a specific surface area of 73.5 m^2/g, higher than those of MG-150 (49.5 m^2/g) and MG-210 (73.4 m^2/g). The result agrees well with the highly branched structures shown in the FE-SEM images. The Tafel slope of 137 mV/decade for the MG-150 hybrid also explains its slightly lower efficiency in DSSCs. CV results (Figure 2-7) showed that the MG-180 hybrid has a larger difference of reduction/oxidation potential and a higher peak current, suggesting more active sites in MG-180 hybrids and higher reactivity in electrochemical reactions.

Besides the HER reactivity of the MG-180 hybrid, a stable performance was also demonstrated by a constant potential of -0.5 V for 20,000 s (Figure 2-6c). A comparison of as-prepared hybrids with exfoliated MoS_2 and amorphous MoS_2 at the same current density highlights the outperformance of the MG-180 with a lower overpotential (Figure 2-6a).[153,186] Therefore, 180 °C offers a preferred balance of the active defect sites, 1T phase of MoS_2 and branched structures for catalytic activities.

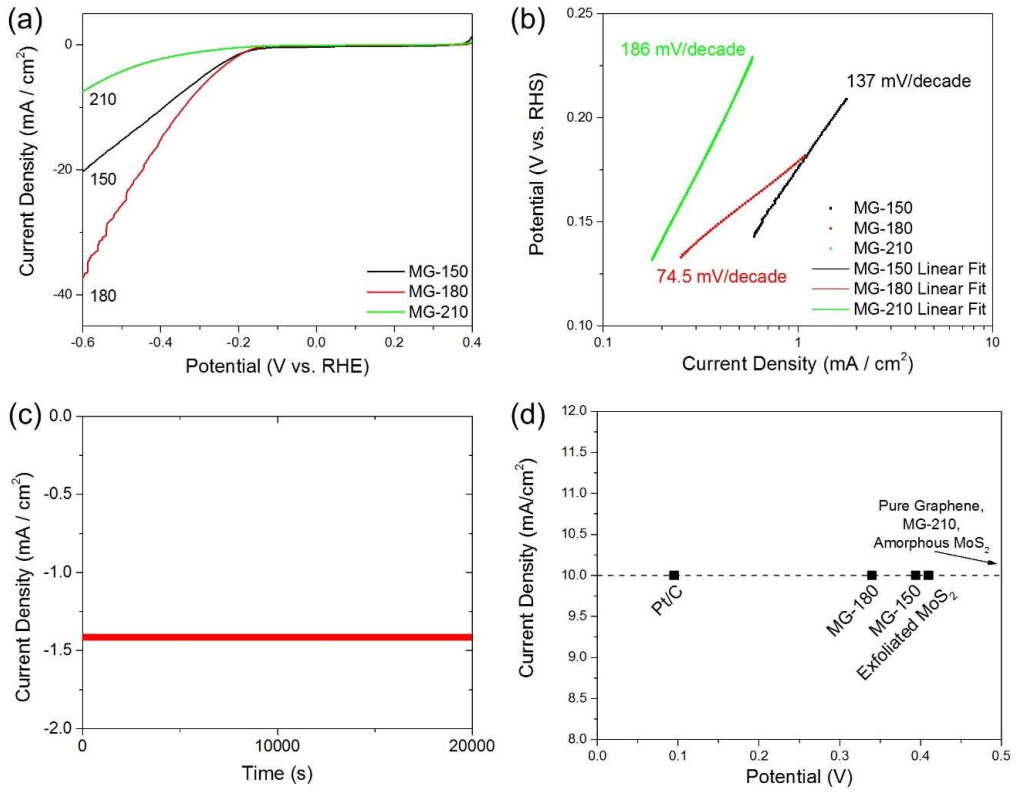

Figure 2-6. (a) Polarization curves after infrared (IR) correction, (b) corresponding Tafel plots of MoS_2/graphene hybrids prepared at 150 °C, 180 °C, and 210 °C, (c) I-t scan of MG-180 for 20,000 s, and (d) comparison of overpotentials at 10 mA/cm^2 for MG-150, MG-180, and MG-210 with Pt/C, exfoliated MoS_2, and amorphous MoS_2.

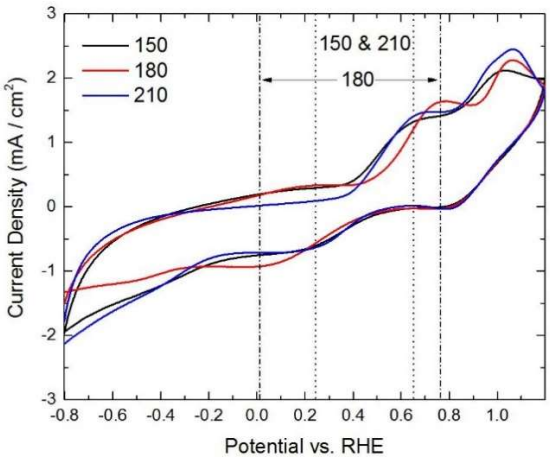

Figure 2-7 Cyclic voltammetry scans of MoS_2/graphene hybrids prepared at 150 °C, 180 °C, and 210 °C. The MG-180 hybrid gave a larger potential between the reduction and oxidation peaks than at 150 °C and 210 °C, indicating a more reliable reduction. At the same time, the higher current density at each peak exhibited high reactivity, which might come from more active sites in the 180 °C hybrids.

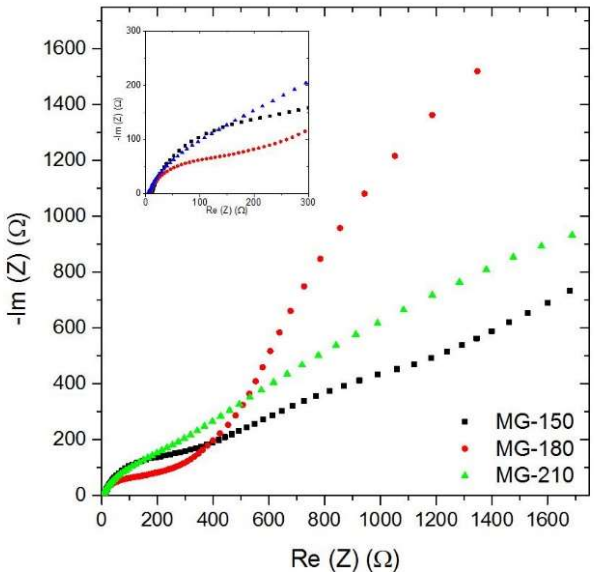

Figure 2-8 EIS Nyquist plots of MoS_2/graphene hybrids prepared at 150 °C, 180 °C, and 210 °C, with zoom-in view shown in the insert. The MG-180 hybrid exhibited a smaller semicircle and higher impedance, indicating faster charge transfer in the structure and higher porosity of the same mass of materials.

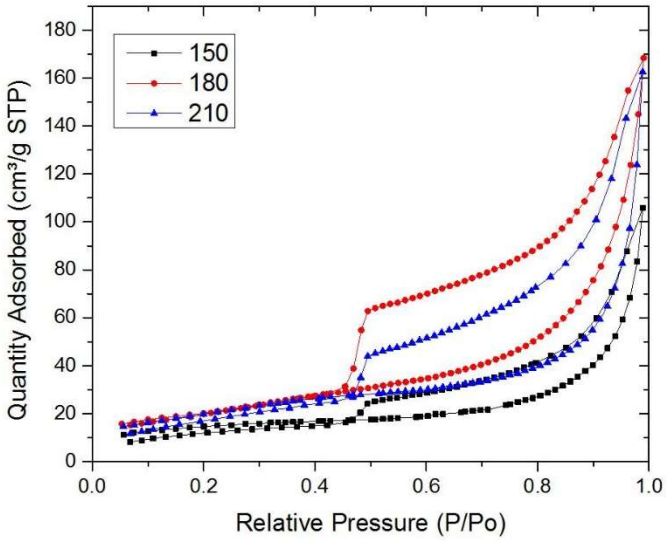

Figure 2-9 BET isotherm linear plot of MoS_2/graphene hybrids prepared at 150 °C, 180 °C, and 210 °C. Similar adsorbed quantity at P/P_0= 1 of MG-180 and MG-210 can be understood by the similar surface profile, while the MG-210 hybrid has more stacking which leads to small pores and shows less mesopore effect on the trace of adsorption and desorption. The low surface area of the MG-150 hybrid proves that MG-150 hybrid has fewer layers and less active sites than that of high temperature ones.

2.4. Conclusions

In summary, the crystallization condition of MoS_2/graphene hybrids was studied by structure characterizations and performance measurements of DSSCs and HER. Benefiting from the excellent reactivity of MoS_2 and the high conductivity of graphene, the hybrids show stable and improved performance compared with their constituents. The MoS_2 in the hybrid shows a crystal phase change from 1T in the low-temperature region (below 180 °C) to 2H in the high-temperature region (above 210 °C), along with crystal quality improvements which reduces defect sites. The existence of the 1T phase improves the reduction reactivity and charge transfer ability of the hybrid. The controlled defect sites also improve the catalytic reaction rate. Although the defect benefits and 1T phase improvements are hard to distinguish in this study, the conductivity of excessive defects can be ruled out. The morphology of MoS_2 on graphene is essential for maintaining high catalytic performance, and perpendicularly-oriented structures in flower-like shape is preferred. This work provides a fundamental guideline and understanding for the rational design and construction of 2D hybrid materials for electrocatalytic applications.

Chapter 3. Semi-Transparent Perovskite Solar Cell Development

3.1. Introduction to smart windows and semi-transparent PSCs

2D nanomaterials have been proved useful for improving solar cell performance and reducing the cost of DSSCs due to their outstanding properties. To apply 2D nanomaterials in emerging solar cells, it is essential to understand the limitations of current materials and their synthesis methods, and explore the possibility of using 2D nanomaterials to address potential issues. Creating semi-transparent solar cells can solve buried issues in regular cells by reducing overall material loading. At the same time, solar energy is widely distributed, and to improve solar energy usage, it is essential to maximize the coverage of solar cells on Earth. Modern buildings, especially high towers and office buildings, have been extensively using glass walls with colored glass to enhance indoor experience and ensure privacy. This design leaves only cement walls or roof areas to mount solar cells and introduces light pollution in the city. Considering the major area of a building exposed to the sun light, windows are better options for collecting solar energy. Replacing colored glasses with semi-transparent solar cells can maximize the solar energy usage.

However, solar cells always require perpendicular light incidence to maintain high performance. Mounting as windows on a building restrains the alignment of the solar cells. For a building, major energy consumptions are heating, cooling and lighting. High performance insulating materials have been used in walls, while windows are the most uncontrolled part. Here, a smart window is designed to passively adapt to sunlight conditioning and control heating. The window is built with multilayer photonic crystals on the back of a semi-transparent PSC. The PSC in this case sacrifices its performance to enable visible light transparency. The multilayer photonic crystals are here to tune the light path at different incident angles and achieve photon management. This work is

collaborated with Dr. Cheng Sun's group in Northwestern University. The photonic crystal design and simulation is carried out by the Northwestern University team, while our own research is mainly focused on the perovskite solar cell.

To achieve semi-transparency and maintain a high efficiency, a solar cell needs to reduce light absorption rate and reach high quantum efficiency. Silicon-based solar cells (1st generation) and thin film solar cells (2nd generation) are not transparent due to the requirement of crystallized silicon plate. DSSCs (including quantum dots, organic dyes and inorganic dyes) are known to have limited quantum efficiency, and the record is about 16% after two-decade research. Perovskite solar cells have been proved as high performance semi-transparent cells. At the same time, perovskite crystals have relatively high absorption rate in infrared light region, which is one of the contributing factors and the most important advantage for high-performance perovskite solar cells.

However, regular PSCs are designed to ensure the maximized light absorption to maximize the efficiency. Although there have been reports on semi-transparent PSCs, these cells are almost always in tandem with other solar cells only to utilize different incident light bands and to maximize absorption in visible light region. In this study, it is essential to improve transparency to create the semi-transparent structure, improve the crystallization to control loss of efficiency, and understand the stability to fulfill the durability requirements of windows.

3.2. Experimental methods

The semi-transparent PSCs for smart windows were developed in two steps. First, the transparency, crystallization and stability of PSCs were studied to obtain a suitable recipe for the smart window

application. Second, multilayers of metal oxides were deposited on the back of as-prepared semi-transparent solar cells as photon management layers to improve the solar cell performance.

Titania paste (T/SP) and lead iodide were purchased from Solaronix SA and Acros Organics respectively. Tris(2-(1H-pyrazol-1-yl)-4-tert-butylpyridine)cobalt(III) tri(bis(trifluoromethane)sulfonimide) (FK209 cobalt(III) TFSI salt) was purchased from Dyesol LTD. Silver (Ag), silicon dioxide (SiO_2) and titanium dioxide (TiO_2) sources for evaporation were purchased from Kurt J Lesker. All other materials were purchased from Sigma-Aldrich.

FTO glass substrates were used as substrates for the cells. First, FTO glasses were polished by zinc powder and 2M hydrochloride solution, and cleaned by ultrasonication sequentially in acetone, isopropyl alcohol and deionized water for 30 minutes each. After drying, the substrates were treated in oxygen plasma for 5 minutes. A 20-40-nm-thick compact TiO_2 layer was then deposited onto FTO substrates by spin-coating precursor solution (80 μL Ti-isopropoxide and 6 μL of 2 M HCl in 1 ml anhydrous ethanol) at 5,000 rpm for 30 s and annealing the substrates at 500 °C for 30 minutes.

The design phase of the semi-transparent PSCs was heavily on the optimization of scaffold layer thickness, perovskite precursor parameters, and the deposition profile. In the design phase, a scaffold layer of mesoporous TiO_2 nanoparticles was deposited by spin-coating a 2:9-ethanol-diluted commercial titania paste at a selected speed for 30s, and gradually heated to 500 °C over 30 min following a previously published procedure.[187] The perovskite layer was deposited using a one-step method. The concentration and the composition of the precursor were determined during

the design phase of the semi-transparent PSCs. The spin-coating procedure was also studied during the design phase.

The finalized perovskite precursor was 0.8M $MAPb(I_{1-x}Br_x)_3$ by controlling x at 0.15, with 264 mg PbI_2, 66 mg $PbBr_2$ and 127 mg CH_3NH_3I in 1 mL solution. The concluded solvent was a mixture of gamma-butyrolactone (GBL) and dimethyl sulfoxide (DMSO) at 7:3 v/v, and spin-coating was used to deposit the solution with 5s increasing speed, 10s 1,000 rpm spin, 5s increasing speed, 15s 5,000 rpm and 5s stopping. Toluene was drop-casted when 10s was left in a spin coating process.[188] The as-prepared samples were then dried at 100 °C for 10 minutes and perovskite crystals formed on the surface.

To complete the solar cell fabrication, hole transport layer was spin-coated at 5,000 rpm for 30 s with a mixture of 72.3 mg spiro-OMeTAD, 28.8 µL 4tB, 17.5 µL lithium TFSI salt in acetonitrile (520 mg/mL), 29 µL FK209 cobalt(III) TFSI salt in acetonitrile (300 mg/mL) and 1 mL chlorobenzene. After coating, the samples were kept in dry oxygen environment for 24 hours. Finally, 10-nm-thick Ag was thermally evaporated on the substrate as a counter electrode to finish the bare semi-transparent PSC fabrication.

Table 3-1 Multilayer material deposition sequence and thickness

Material	SiO_2	TiO_2	SiO_2	TiO_2	SiO_2	TiO_2	SiO_2	TiO_2	SiO_2	TiO_2
Thickness (nm)	468.8	433.0	95.8	174.3	74.6	112.2	77.2	128.0	122.2	76.5

To complete the design of smart windows cells, the finished bare cells were placed in an e-beam evaporator. SiO_2 and TiO_2 layers were deposited with a rate of 1 nm/s and 0.35 nm/s, respectively and the thickness profile was set as a sequence shown in Table 3-1.

To find out the solar cell performance, J-V curves were measured using a solar simulator (Newport 94021A) under AM 1.5G illumination. The electrical profiles were scanned and recorded by a source meter (Keithley 2420). A homemade mask was used to control the active area to 0.35 cm^2 and an angular stage was created by 3D printing to control the tilting angle of cells at 0°, 15°, 30°, 45° and 60°. The cross sections of the cells were studied with a Hitachi (S-4800) field-emission scanning electron microscopy (FE-SEM).

3.3. Results and discussion

3.3.1. Transparency improvements

To reduce regular PSC absorption and fulfill the semi-transparency requirement, four different approaches were tested. Firstly, decreasing perovskite precursor concentration was a straight-forward option. Regular precursor concentration was reported to be ~1 M.[6] To test the effects of reduced concentrations, the sequence of 0.75 M, 0.5 M and 0.25 M was prepared as the only variable in controlled experiments. During this process, a significant loss of efficiency was observed when the concentration reduced to 0.5 M. Compared with literature data reported by Snaith *et al.*[23], reduced concentrations always lead to the inconsistency of perovskite film and further lead to short circuit. Lab tests showed efficiencies around ~1% for 0.25 M precursor concentration, ~5% for 0.5M precursor concentration, and ~7% for 0.75 M precursor concentration. To ensure repeatable and reliable performance, the precursor concentration was set

the lowest at 0.75 M. After reducing concentrations, the resulting transparency of as-prepared PSCs was still low.

Reducing scaffold layer thickness was another possiblity to improve tranparency. Increasing spin-coating speed of scaffold layer was considered to reduce the film thickness and perovksite material loading. Standard spin-coating speed of scaffold layer was controlled at 6,500 rpm,[6] which resulted in a thickness of around 100 nm. When increasing the speed to 7,000 rpm and 8,000 rpm, the scaffold layer thickness decreased slightly and was still obeserved close to 100 nm by elipsometry testing. At the same time, high spin-coating speeds introduced problems for film qualities and uneven layers with thicknesses varying from 30 nm to 500 nm were observed, due to the turbulence in the chamber during high-speed spinning. By revewing PSC structures, as shown in Figure 1-2, the plannar-style PSCs came to favor with the removal of scaffold TiO_2 layer in DSSC-style PSCs. By Removing scaffold layer and preparing planar PSC with pre-selected concentration, the transparency increased significantly and the approach was considered for the final design.

To further imporve the transparency, bandgap tuning was tested as well. As summarized in Figure 1-3, different perovskite crystals have different band positions, which create opportunities to increase visible light transparency by tuning bandgaps. To retain the perovskite crystal structure without significant defects, lead halides can be modified by introducting different halides. 10 wt.% $PbCl_2$ was first added to PbI_2 precursors; however, the sacrifice of efficiency was huge. This can be understood by the big size differences between iondine and chlorine, which leads to the instability of perovskite crystals. By introducing 10~15% $PbBr_2$ instead of $PbCl_2$ to the PbI_2 precurosr, the transparency of PSCs was significantly improved and the performance was

maitained.[25] To finalize transparency improvement, a 10~15% $PbBr_2$ in $PbCl_2$ precursor with 0.8 M concentration was used and planar-style PSC was constructed.

3.3.2. Crystallization quality control

For use in windows, crystallization quality is important. Otherwise, the uneven surfaces may project uneven light paths. At the same time, due to thinner films compared with regular cells, poorer crystallization can lead to significant quantum efficiency loss in the cell. Here different approaches were investigated to ensure the glassy-crystallization quality.

Reported by Nazeeruddin group[189], 10 wt.% exceeding PbX_2 precursors were used to react with the CH_3NH_3I precursor. Theoretically, this method can reduce the evaporation loss of CH_3NH_3I during fabrication. Excess PbX_2 captures the freed CH_3NH_3I radicals during the crystallization process, which potentially controls the quality of crystallization. However, low efficiencies were recorded with excess PbX_2 in the crystal. This can be explained by the reduced overall quantity of crystalized perovskite materials. In the as-prepared semi-transparent PSCs, the quantity of perovskite was lower than regular cells, and the reduced amount led to the significant current decrease.

Another approach to improve crystallization was the solvent engineering method, introduced by Seok group.[188] This method combined GBL and DMSO as initial solvent for spin coating and toluene as the second solvent before the end of spin-coating processes. The toluene used in the process has a lower solubility of perovskite crystals and creates a solvent extraction to improve

surface quality. Solvent engineering improved the crystallization quality significantly and was later used in the semi-transparent PSC fabrication.

3.3.3. Stability study

To understand potential issues with as-prepared PSCs, stability was studied and summarized. As shown in Figure 3-1, after being exposed to the uncontrolled lab environment for 24 hours, the surface degradation was visible and can be summarized in three ways.

First, the perovskite layer can quickly react with water vapor, and CH_3NH_3I in the crystal structure can be etched away during storage. The yellow dots (PbI_2) were observed by naked eyes and scattered in the dark brown area (perovskite), which was caused by the regional degradation of perovskite crystals. Second, silver used in semi-transparent PSCs were controlled to 10-nm thickness, and can be easily oxidized during storage. The degraded black spots not only reduced local light incidence, but also served as a catalyst to further degrade covered active materials and neighboring silver regions. Third, the spiro-OMeTAD used in the HTM can be etched away by oxygen and water. At the same time, the HTMs used in PSCs are known sensitive to heat, which can experience significant degradation during later multilayer deposition. As shown in Figure 3-2, the semi-transparent PSC maintained the normal V_{OC} after exposure to high temperature, but the current decreased significantly in the high voltage region. All these concerns promoted immediate deposition of multiple layers after fabrication of semi-transparent solar cells in order to protect active materials.

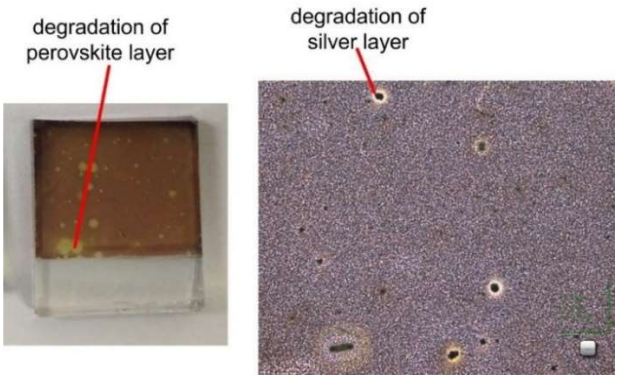

Figure 3-1 Current issues with degradation of semi-transparent PSCs.

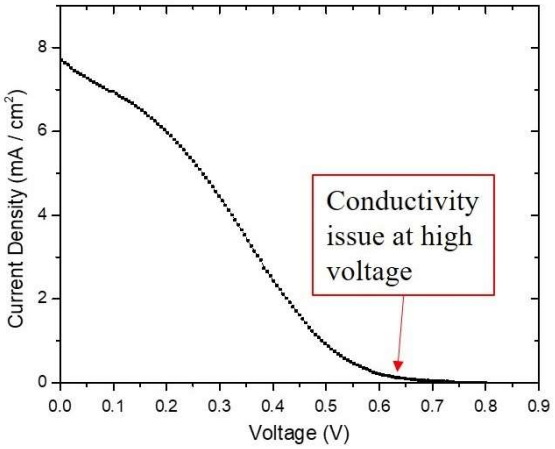

Figure 3-2 The semi-transparent PSC performance after HTM is exposed to high temperature for multiple layer deposition.

3.3.4. Solar cell testing and discussion

The cross-section of the coated semi-transparent perovskite solar cell is shown in Figure 3-3a. The photovoltaic section is around 1 μm thick and the wave-shape surface profile comes from the spin-coating process.[190] A zoom-in view of the multi-layer coating is shown in Figure 3-3b, where the thickness of each layer matches very well with Table 3-1 and the high thickness uniformity of the films benefits from the high quality of the e-beam evaporation. A picture of the fabricated semi-transparent solar cell is shown in Figure 3-3c. The windows are clearly observed through the cell in the picture and the as-prepared cells exhibit similar feeling of the color glasses used in buildings.

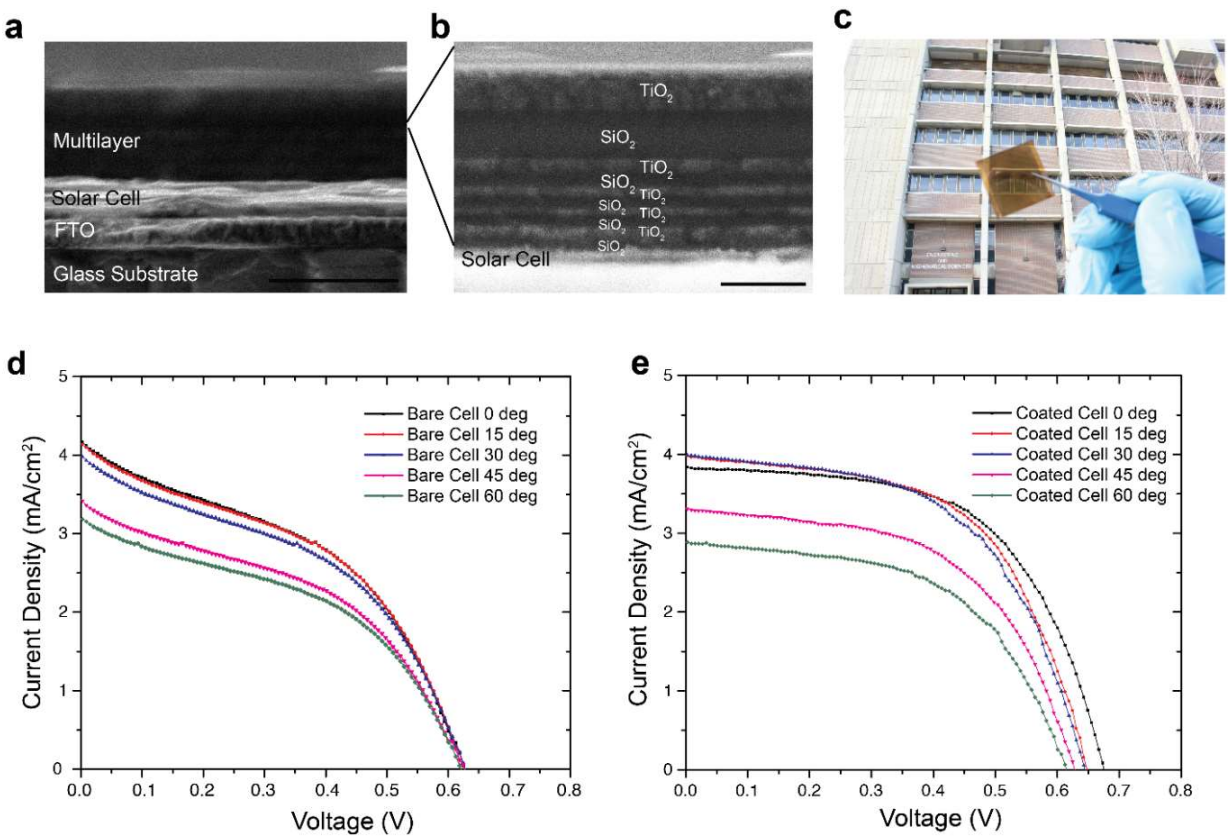

Figure 3-3 (a) Field-emission scanning electron microscopy (FE-SEM) image of the photonic structure cross section of the semi-transparent perovskite solar cell. The scale bar is 3 μm. (b) FE-SEM image of the 10-layer multi-layer photonic structure with alternating layers of SiO_2 and TiO_2. The scale bar is 1 μm. (c) Photo of the fabricated semi-transparent solar cell (d) Current density-voltage curves for bare perovskite solar cell. (e) Current density-voltage curves for cell coated with multi-layer photonic structure.

Table 3-2 Tested important cell parameters shown in Figure 3-3

	Open Circuit Voltage (V)		Short Circuit Current Density (mA/cm^2)		Fill Factor (%)		Efficiency (%)	
	Bare	Coated	Bare	Coated	Bare	Coated	Bare	Coated
0°	0.625	0.675	4.19	3.85	43.0	57.8	1.17	1.57
15°	0.626	0.647	4.17	4.00	43.2	56.3	1.17	1.52
30°	0.627	0.644	4.01	3.97	42.8	54.9	1.13	1.46
45°	0.624	0.627	3.42	3.32	43.0	54.0	0.96	1.17
60°	0.621	0.614	3.21	2.90	43.5	53.9	0.90	1.00

The performance comparison of bare cells and coated cells are given in Figure 3-3d and Figure 3-3e with important parameters given in Table 3-2. With angle tilting from 0º to 60º, both types of cells show a decrease in i_{sc}, which can be predicted from lower absorption of incident light. At the same time, the V_{oc} remains the same for all cells, and this proves the high crystal quality of prepared perovskite layer. The i_{sc} for both bare and coated cells are comparable at the same tilting angle, but the FFs for coated cells are clearly higher than those of bare cells, with an increase from 42.8 ~ 43.5 to 53.9 ~ 57.8. However, i_{sc} quenching has been observed consistently during all tests, before and after e-beam coating multi-layer materials. This can be explained by the radiation during deposition, which heated the cells and quickly aged the organic HTMs. A normal semi-transparent solar cell without suffering high temperature deposition process shows comparable performance to published works (Figure 3-4).[191-193]

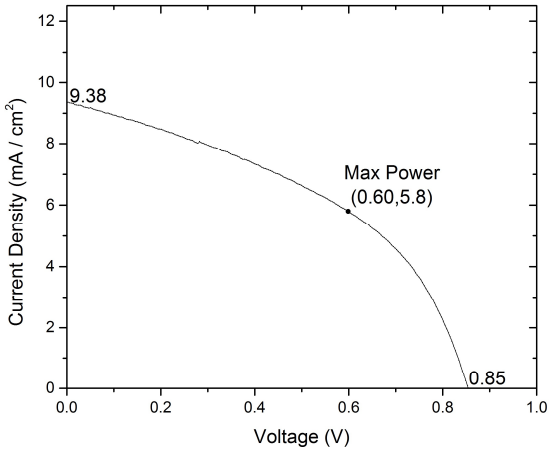

Figure 3-4 A normal semi-transparent solar cell without suffering a high temperature shows comparable performance to published works. This indicates a better multilayer deposition method is important.

To further investigate the coated semi-transparent PSC, spectral response and quantum efficiency are analyzed. The spectral response shown in Figure 3-5, exhibits a wide absorption, especially a long tail in IR bands, which is essential for room temperature control from solar radiation. The similar response comparable with literature publications indicates the stable performance of perovskite crystal after high-temperature coating process. The integrated current based-on AM 1.5G solar radiation and external quantum efficiency (EQE) performance is similar to the i_{sc}, which indicates the mismatch factor for this cell is negligible. To verify the hysteresis of coated semi-transparent PSC, forward and reverse scans are compared in Figure 3-6. The resulted current curve is considered close to each other with or without solar radiation, which indicates the hysteresis is not significant in this structure. Furthermore, statistic results of the coated cells at 0° tilting are given in Figure 3-7. The big variations for all parameters indicate the stability issue of coated cell. Overall, a yield of 19.4% success rate is achieved, for total fabrication of 98 cells.

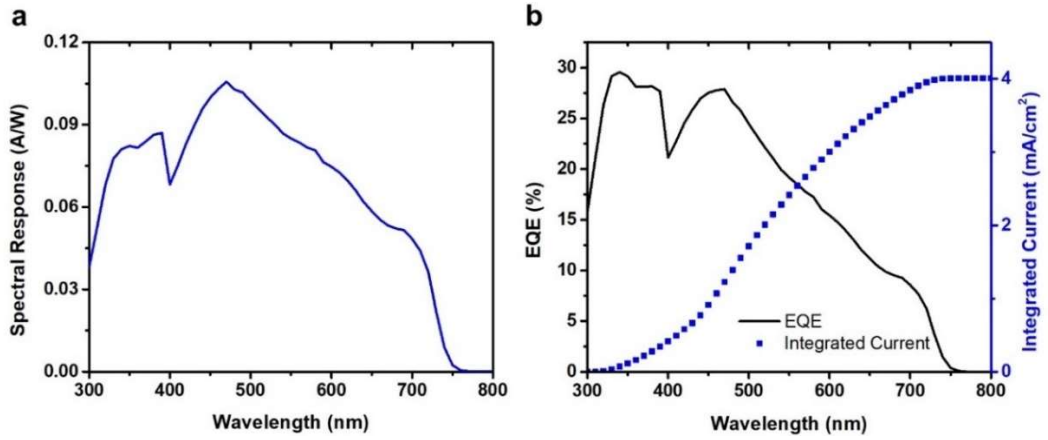

Figure 3-5 (a) Spectral response and (b) external quantum efficiency of coated semi-transparent solar cell part in the smart window. The integrated current is close to the coated cell at 0° tilting. The spectral mismatch factor is negligible in this study.

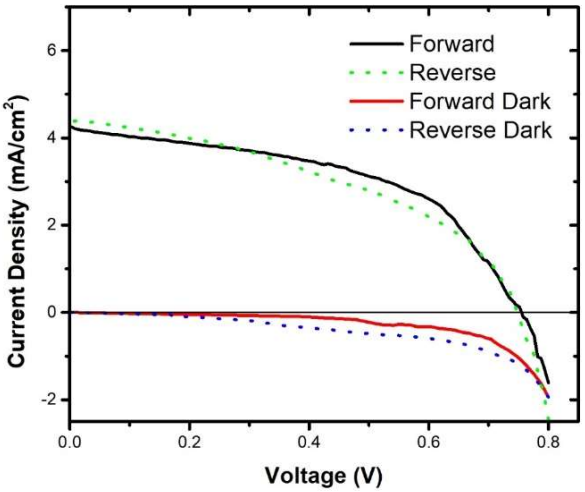

Figure 3-6 Forward (short-circuit to forward bias) and reverse (forward bias to short-circuit) scans of coated semi-transparent solar cell under AM1.5G light incident or in dark environment. The responses of forward and reverse scans are considered close. The scan speed is 0.07 V/s.

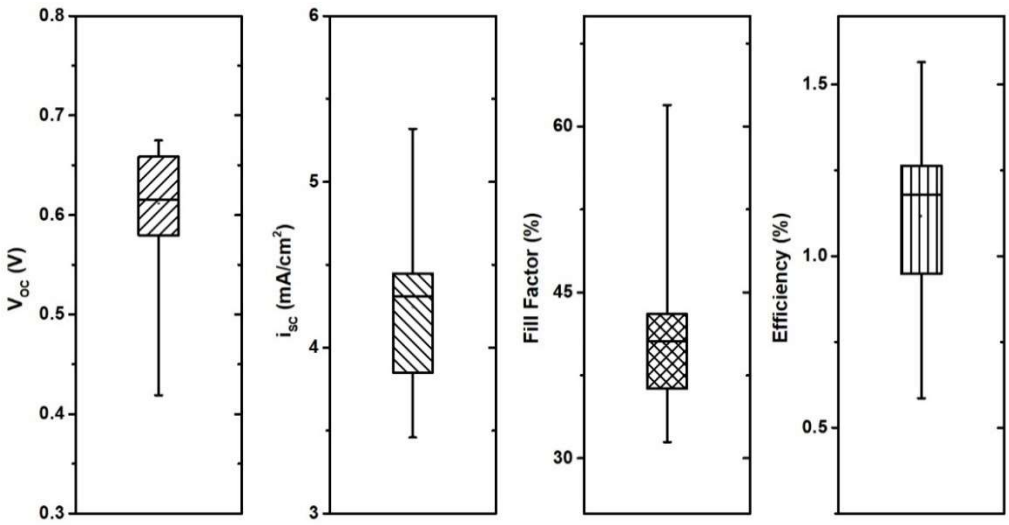

Figure 3-7 Current-voltage metrics of 19 coated cells at 0° tilting testing condition. The statistical results were calculated from coated semi-transparent solar cells with 0° tilting during testing. 98 coated cells were prepared for testing, with a yield of 19.4% success. The stability is limited because of the spiro-OMeTAD aging during coating process.

3.4. Conclusions

The semi-transparent PSC was successfully prepared for smart windows use, but many challenges were shown at the same time. First, the degradation during coating process severely quenched the conductivity of HTM films, which leads to a low current density. A low-temperature coating method is preferred. For example, it is possible to use ALD to complete the ten-layer photon management coating. Secondly, because of the low loading of solar cell materials, a small degradation was relatively significant in this study. Both degradation problems could be solved by using better HTM films. A hydrophobic HTM will resist water vapor etching of perovskite crystals. In addition, a good HTM conductivity can help reduce silver back-contact coverage and further improve the cell transparency without efficiency loss. This work highlights the importance of low cost and high performance HTM design, and offers suggestions for important aspects to design HTMs. The stability issue discovered in this study can be addressed by applying selected 2D nanomaterials that are relatively stable, e.g., graphene-based materials. Also, a high conductivity can be achieved with a suitable surface modification to accept holes and prevent electron-hole recombination. The transparency, crystallization and stability of PSCs were also studied for future high-performance PSC fabrication.

Chapter 4. CuS/GO-Crumpled 2D Nanohybrids for Hole Transport Material Design in Perovskite Solar Cells

4.1. Introduction

PSCs currently are significantly limited by HTM choices. Hysteresis issues, low stability and high cost are common problems for most HTMs. HTMs can be categorized into three main groups: small organic molecule, polymeric and inorganic HTMs.[37] Spiro-OMeTAD is the most widely used HTM and is a type of small organic molecule HTM. In 2013, Graetzel *et al.*[6] used spiro-OMeTAD to create a PSC with efficiency of 20.8%. Since then many derivatives of spiro-OMeTAD have been reported including pp-, pm- and po-spiro-OMeTAD, and many other designs.[38] However, a common issue for this type of HTM is the low stability, especially the water vapor etching.[194] The polymeric HTMs are also widely studied as an alternative for spiro-OMeTAD, but the extreme high cost hinders the possibility for wide use. The inorganic HTMs such as CuI, CuSCN and NiO, always have a low cost.[195,196] However, a huge disadvantage for inorganic HTMs is that the solvent used for HTM deposits can always partially dissolve perovskite layers, which results in compromised stabilities.[37]

Recently, a CuSCN-based HTM was reported with GO decoration at gold and HTM interface and the cell the efficiency improved to >20% and maintained over 95% of initial performance after 1,000 h testing.[17] The thermal stability of CuSCN HTM was also evaluated by Jung *et al.*,[197] which showed a stable performance in 125 °C with 40% relative humidity over 100 h. The new results indicate it is necessary to sacrifice perovskite layer with partial damage but use CuSCN instead of other HTMs. However, current coating methods require precise timing to reduce the damage to perovskite layer, which can be difficult for reliable commercial production. At the same time,

graphene has been reported as an essential interface material to address the charge accumulation in CuSCN crystals, which requires additional coating steps. Although high performance of CuSCN HTM has been reported, an improved solution is yet to be discovered.

The objective of this study is to tackle current HTM issues, and create a low-cost and easy-to-load HTM alternative. It is interesting to notice that CuSCN can degrade to CuS, when temperature is over 300 °C.[198-200] CuS has been widely reported as an efficient p-type semiconductor with Hall mobility of 7.24 $cm^2V^{-1}s^{-1}$ and the carrier concentration of $+2.5\times10^{21}$ cm^{-3}, which is suitable as HTM for PSCs.[201-203] Lei *et al.* reported a facial solvothermal approach to enhance a polymer solar cell with CuS as HTM.[204] A few earlier reports also discussed the high capability of CuS as an effective HTM for PSCs.[205] The high performance for both CuSCN and CuS indicates that employing a crumpling method with graphene nanosheets through heating can create high performing HTM without additional coating and thermal degradation concern. The crumpling method has been reported to generate high performance battery and catalyst materials.[206-208] Taking advantage of the crumpling and shrinking effect of quick-drying 2D nanosheets during heating, the crumpling method can load active materials, carry modification reaction and create hybrid structure at the same time.[206] In this work, a feasible crumpling method to treat CuSCN with GO and form CuS/GO-crumpled nanohybrids is discussed, which can later be coated without partial dissolving perovskite layers. The CuS/GO-crumpled HTM is discussed from material study to PSC performance analysis.

4.2. Experimental methods

4.2.1. Materials

Titania paste (T/SP) was purchased from Solaronix SA and diluted by anhydrous ethanol (v/v 2:9) for coating. PbI_2 was purchased from Acros Organics (>98% purity). MAI was purchased from Dyesol LTD. Gold (Au) sources for evaporation were purchased from Kurt J Lesker. GO was prepared from a modified Hummer's method.[170] All other materials were purchased from Sigma-Aldrich.

4.2.2. Hole transport material preparation

CuSCN was first dissolved into NH_3 aqueous solution (28-30 wt.% NH_3 basis) at a concentration of 10 mg/mL. GO powders were then added into the solution at a concentration of 1 mg/mL. The obtained suspension was sonicated in a 70 W water bath for 15 min to ensure the layer separation for GO, and then stirred for 30 min to ensure the surface adsorption.

A spray pyrolysis process was used in this study.[206] An ultrasonic nebulizer (Sonaer, 241T, 2.4 MHz) was used to generate solution droplets containing GO and CuSCN. The droplets were carried by 1 LPM argon and ammonia mixed gas (10:1 v/v) into a horizontal tube furnace preheated at 650 °C. The rapid heating in the tube furnace quickly dried the GO sheets and crumpled them with CuSCN during flight in the furnace.[207] The reaction product was captured by a 0.65 μm Millipore® DVPP membrane at the end of flow path.

To prepare a coating solution, the obtained gray-green powder was sonicated in chlorobenzene to form a 35 mg/mL suspension. For comparison, CuSCN in NH_3 or diether sulfide (DES) solution was also prepared at 35 mg/mL.

4.2.3. Solar cell fabrication

First, FTO glass substrates were washed in Hellmanex® III (~2% v/v in DI water) for 30 min by sonication, and then sequentially rinsed in DI water and isopropyl alcohol to remove any residuals. After drying in dry airflow, the substrates were treated in oxygen plasma for 15 minutes.

Titanium (diisopropoxide) bis(2,4-pentanedionate) (75% in isopropanol) was diluted in anhydrous ethanol (1:9, volume ratio) to prepare blocking layer precursor, and then was spin coated onto FTO glass at 5,000 rpm for 30 s. After annealing at 500 °C for 30 minutes. A layer of mesoporous TiO_2 precursor was spin-coated onto the substrates with a 2:9-ethanol-diluted commercial titania paste at 2,000 rpm for 10 s and at 4,000 rpm for 20 s. Then the coated glass was gradually heated to 500 °C over 30 min following a previous published profile.[187] A lithium treatment was carried out by spin-coating 10 mg/mL LiTFSI acetonitrile solution at 3,000 rpm for 20 s, and drying at 450 °C in air.

The perovskite layer was deposited using a one-step method. The solvent was a mixture of dimethylformamide (DMF) and DMSO at 4:1 v/v. The concentrations of all precursors were controlled at 1 M for MAI, 0.2 M for MABr, 1.1 M for PbI_2 and 0.2 M for $PbBr_2$. Spin-coating was used to deposit the solution with 5 s increasing speed, 10 s 1,000 rpm spin, 5 s increasing speed, 20 s 6,000 rpm and 5 s slowing down. Chlorobenzene was drop-cast when 15 s was left in a spin coating process.[188] The as-prepared samples were then dried at 100 °C for 15 minutes and perovskite crystals formed on the surface.

Hole transport layer was spin-coated at 5,000 rpm for 30 s with a prepared solution. For comparison studies of CuSCN in DES or ammonia, the solution was drop casted onto the substrate after the spin speed reached 5,000 rpm in 1~2 s. Finally, 60-nm-thick Au was thermally evaporated on the substrate as current collector.

4.2.4. Solar cell testing

All cells were kept in a dry box ($CaCl_2$ as drying agent) before testing. No pre-conditioning was used for all measurements. The J-V curves were measured using a solar simulator (Newport 94021A) under AM 1.5G illumination in ambient air environment at 23 °C. The solar simulator was calibrated using a Newport 91150 reference cell. The electrical profiles were scanned and recorded by a source meter (Keithley 2420) at the rate of 20 mV/s. A non-reflective mask was used to control the active area to 0.12 cm^2.

The EQE was tested using a Newport quantum efficiency testing kit, equipped with a 300 W xenon arc lamp, Oriel Cornerstone™ 260 1/4 M double grating monochromator (Newport 74125) and Merlin™ Radiometer System (Newport 70104).

4.3. Results and discussion

The CuS/GO-crumpled HTM material was first analyzed by SEM. As shown in Figure 4-1(a), the thin films of reduced GO flakes cover small crystal balls. Evaluated by EDS distribution, the thin film shows mainly carbon signature, which can be verified as GO flakes, while the crystal balls contain mainly Cu and S. EDS spectra also indicate a close to 1:1 Cu/S atomic ratio, while oxygen and nitrogen atomic ratio at 0%. This indicates a high ratio of CuSCN decomposition to CuS. To verify the CuS formation without GO interfering, pure CuSCN in ammonia solution was processed

through the spray pyrolysis, and the image is shown in Figure 4-1(b). Without the coverage of GO, the CuS crystal balls are individually stacking. The size of pure CuS crystal balls is similar to that of CuS/GO-crumpled nanohybrid, and ranges from ~100 nm to ~500 nm. To understand the coverage of this process, the HTM coated surface was studied using SEM and shown in Figure 4-1(c). Instead of forming a film to fully cover the cell surface, like traditional spiro-OMeTAD HTM, the coated surface was covered by aggregated nanohybrids. The gaps on the background indicates an insufficient coverage, which can lead to a lower performance, while this can be addressed in the future study.

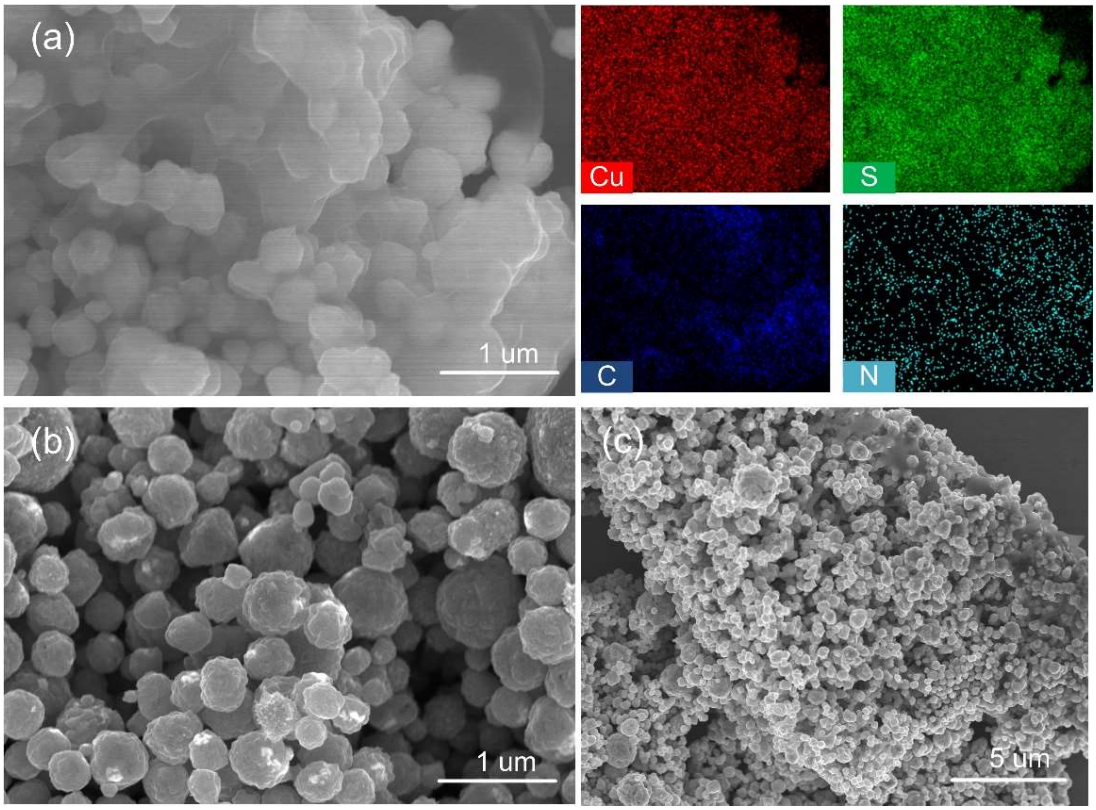

Figure 4-1 (a) SEM image of CuS/GO-crumpled HTM under x25K magnification, and the EDS elemental mapping of Cu, S, C and N in the same region. (b) SEM image of pure CuS under x25K magnification. (c) SEM image of the surface of the as-prepared CuS/GO-crumpled HTM.

The commercial CuSCN, CuS and CuS/GO-crumpled HTM were characterized using XRD to determine the phase change in the crystals. As shown in Figure 4-2, after 650 °C treatment, CuSCN peaks are significantly quenched, as peaks at 27° and 32° show a significant decreased intensity. Additionally, a new peak at 47° appeared. After comparing with standard database, new peaks match CuS (101), (102), (103) and (006) peaks around 25° to 35°, (110) peak at 47° and (108) peak at 54°.[209] No GO peak or wide background can be found in the CuS/GO-crumpled nanohybrid, which suggests the nanohybrid has a high monolayer ratio of GO and the crumpled GO nanosheets is efficiently separated by CuS crystals.

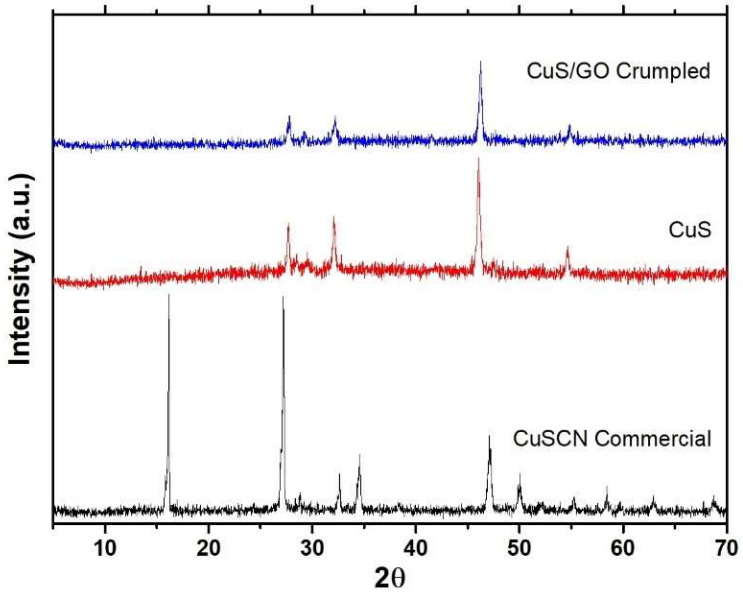

Figure 4-2 XRD results of CuS/GO crumpled HTM compared with commcercial CuSCN and CuSCN through the same process.

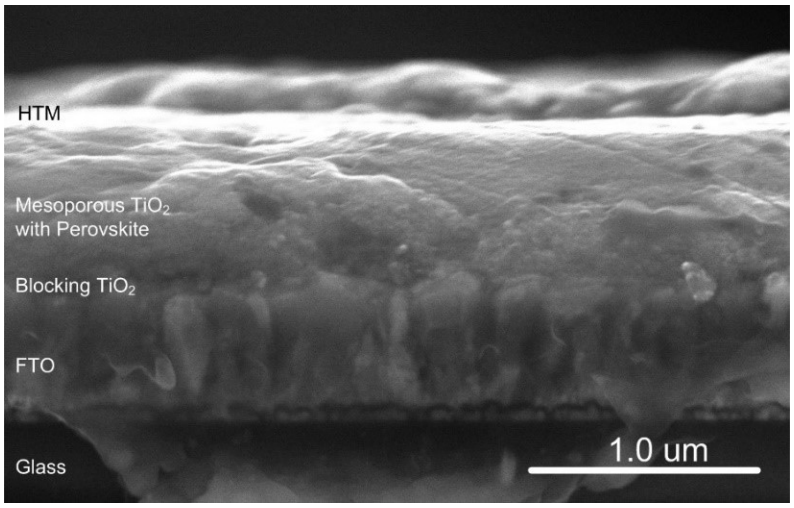

Figure 4-3 Cross section of fabricated PSC. From bottom to top, each layer can be identified as glass substrate, FTO layer, blocking TiO_2 layer with a very thin profile, mesoporous TiO_2 with perovskite layer, and the CuS/GO-crumpled HTM layer. The Au back count is not in the cross section image.

After assembling the PSC, the cross section is taken by SEM to study the coating thickness. As shown in Figure 4-3, the perovskite layer has a thickness of ~600 nm with mesoporous TiO_2 as ETM, which is comparable with published results and considered sufficient for stable PSC performance. The CuS/GO-crumpled HTM shows a coated thickness of around 100 nm. However, from the cross section view, the coated HTM resulted a non-uniform coating, which can result in unstable current during tests. The phenomenon is observed and shown in Figure 4-4(a). The main parameter for the scan is given in Table 4-1. The low FF also indicates an improved coating method instead of spin coating is necessary.

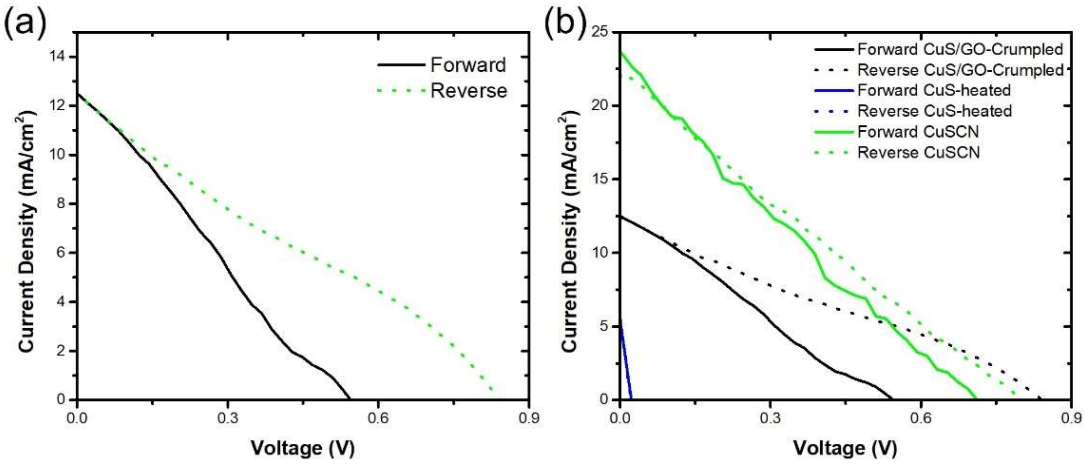

Figure 4-4 (a) J-V scan of PSCs with CuS/GO-crumpled HTM and (b) the comparison of PSCs made from CuS/GO-crumpled HTM, CuS-heated HTM and standard CuSCN HTM.

Table 4-1 Main parameters of J-V curve for PSC with CuS/GO-crumpled HTM.

	V_{oc} (V)	J_{sc} (mA/cm^2)	V_{max} (V)	J_{max} (mA/cm^2)	Fill Factor (%)	PCE (%)
Forward	0.55	12.47	0.27	6.41	25.2	1.73
Reverse	0.84	12.43	0.55	5.03	26.5	2.77

The J-V curve shown in Figure 4-4(a) suggests that the hysteresis issue is present in current CuS/GO-crumpled HTMs, with a 1.9 V difference in V_{oc}. This indicates a high contact resistance between HTM and perovskite layer,[32] which is also observed from PSCs with standard CuSCN HTMs and a smaller difference in Figure 4-4(b). Although ETM is considered as the root of hysteresis, the inefficient charge transfer of HTM can worsen hysteresis effect in the current cell structure. The close V_{oc} of reserved scan for both standard HTM and CuS/GO-crumpled HTM indicates the conduction band of as-prepared HTM is well aligned with the valence band of perovskite layers. To reduce the hysteresis effect, improving coating quality is an effective method. Meanwhile, the CuS/GO-crumpled HTM enables the perovskite layer to deliver an i_{sc} of 12.4

mA/cm^2, which is also validated through integrated current shown in Figure 4-5(b). The spectral mismatch factor is 0.88 after calculation, which is considered normal for current coating quality. Figure 4-4(b) compares the CuS/GO-crumpled HTM with the standard CuSCN HTM coating methods. With all cells coated in ambient air, the quality can be hindered due to the exposure to moisture, which results a low FF. The standard CuSCN gives a higher short circuit current than CuS/GO-crumpled HTM, which suggests a more completed coverage and more efficient charge transportation. At the same time, the result of pure CuS after decomposition from CuSCN shows extremely low performance, and this demonstrates the importance of GO nanosheets in this nanohybrid structure. Additional spectral response analysis shown in Figure 4-5(a) demonstrates a steady high absorption in visible region. This agree with initial design that CuS/GO-crumpled HTM has suitable band position for HTM applications.

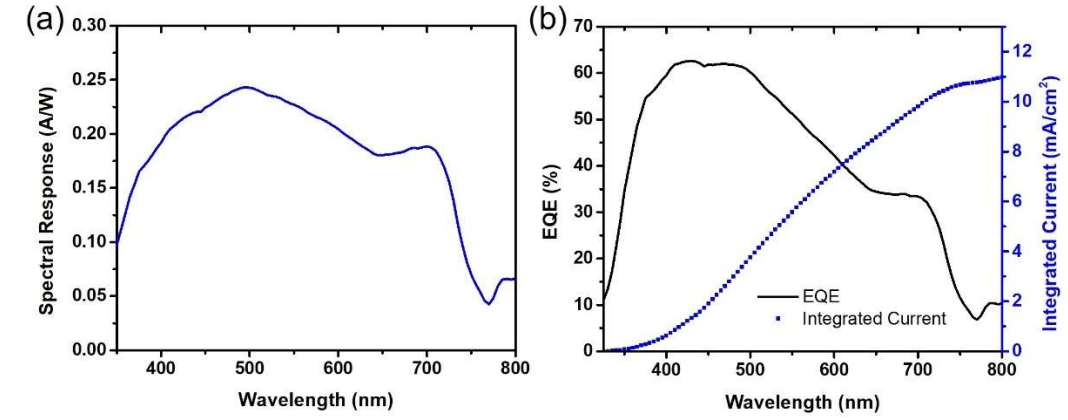

Figure 4-5 (a) Spectral response for the PSC with CuS/GO-crumpled HTM and (b) EQE of the cell and the integrated current.

4.4. Conclusions

This study explores the possibility of using crumpled 2D nanomaterial hybrid structures for HTM applications in PSCs. A feasible CuS/GO-crumpled HTM fabrication method is discussed and the

resulting material is successfully demonstrated in PSCs. The prepared HTM is stable in ambient environment with tolerance to heat and water vapor. However, current CuS/GO-crumpled HTM shows lower performance compared with standard PSC of CuSCN coated with DES as solvent. From initial analysis, this is a result of limited coverage with current coating methods. Additional work on doctor-blade coating or spray coating method may address this issue for a higher FF and i_{sc}. For general PSC preparation, a PSC can be directly coated when HTM is prepared through the spray pyrolysis process, which can significantly reduce the coating time. This study demonstrates the feasibility to use 2D nanomaterial as a platform to prepare the HTM for PSC studies.

Chapter 5. Environmentally Friendly Lead Removal and Recovery from Waste Lead-Acid Batteries

5.1. Introduction

The confliction between public concern of lead contamination and the dependence of lead in PSCs inspires ideas on collecting lead contaminants for solar cell use. At the same time, recycling methods for lead-contaminated sulfuric acids are required for the retiring lead-acid batteries. Collecting lead wastes, refining material purity and reforming perovskite precursors are essential for environmentally friendly solar cell studies. As summarized in Figure 1-15, sulfuric acids are not effectively recycled currently, and recovery methods are important for battery industries.[210] Typical lead-acid batteries have sulfuric acid concentrations of around 10 to 35 wt.%,[211,212] and the acidity is much higher than that of wastewater[145]. Although a few recycling methods have been reported, the extremely high cost and low treatment volume is not acceptable for battery recyclers.[210] Novel acid recycling methods are required for sustainable battery manufacturing.

In a strong acidic condition, due to a high concentration of protons, such as in a waste sulfuric acid, high selectivity is extremely important. Earlier studies showed that different surface groups have very different selectivity to certain ions. Dias *et al.* summarized some common surface treatments for different ions.[213] Generally oxidization groups on the surface are targeting organic compounds, Cu, Cd and Cr contaminants. The functional groups are oxidized by ozone or hydrogen peroxide and nitric acid, and the functional pH range is typically 2~12. Sulfuration is a common approach to target Hg, Pb, Cd, Cu, As and Zn, and is typically treated in S, H_2S, SO_2 and other sulfur sources. Nitrogenation is usually treated in strong nitrogen ratio environment by NH_3, HCN, urea and more. The product is commonly targeting contaminants like organics, Pb, Hg, Cd

and Cu. There are other types of surface modification, like ligand functionalization. Specific ligands are designed for certain contaminants, and show high selectivity. Popular ligands targeting Fe, Cu, Co and Ni work in the environment with pH at 4~10, which is relatively narrow, and a few ligands work in pH between 1 to 6.

Combining the understanding of 2D nanomaterial properties and the ion removal system designs, the ion removal performance in strong acidic conditions was studied through three different approaches, including adsorption, filtration and capacitive deionization (CDI). Ideally, filtration is preferred by most companies, because of the continuous treatment and high volume capacity. However, adsorption typically gives better performance, because of long time exposure. CDI process is new in this field and shows high potential for selective removal. In this study, the targeted ions in the acid were Pb(II), Fe(III), Zn(II), Cu(II), Mn(II), Co(II) and Ni(II), and these ions were closely studied for removal rate and Pb(II) recovery was also considered. The sulfuric acid recovery was limited by the strong acidic condition. However, starting from raw waste sulfuric acid, a recycling method to reform PSC precursor was successfully demonstrated.

5.2. Experimental methods

5.2.1. Acid preparation and treatment designs

Waste lead-acid battery acid was obtained from a partner company's recycling center and sampled on November 26th, 2014. All chemicals used in this study were purchased from Sigma-Aldrich. Whatman™ glass microfiber filter (GF/F, pore size 0.7 μm) was used to filter out the suspension in the acid. To understand the consumed acid condition, both solids and filtrate were studied. Specific gravity (*sp. gr.*) was tested for the filtrate to determine the original sulfuric acid

concentration. The obtained solids were directly dried at 65 °C for 24 hrs, and XRD was used to study the composition.

For a filtration process, a Chemglass® 40/35 filtration setup was used. Two types of filtration processes were tested. The first type used 50 mg powder active materials, which were sandwiched between two Whatman™ GF/F glass microfiber filters in the setup. 50 mL pre-filtered acid was filtered through the filtration setup and collected for inductively coupled plasma atomic emission spectroscopy (ICP-AES) tests. The second type used an in-house prepared active membrane, which was tested by direct filtration of different volumes.

For an adsorption test, 50 mg of each active material was dispersed in 50 mL sulfuric acid sample and mildly stirred for 24 hrs. The stirring speed was controlled around 100 rpm to 300 rpm to prevent significant precipitation of active materials, and varied among different materials because of the density difference among materials. At the end of the adsorption, the suspension was filtered through Whatman™ GF/F glass microfiber filters and the filtrate was tested by ICP-AES to identify ion concentrations.

To initialize the acid treatment, commercial activated carbon (AC) materials were tested in filtration or adsorption systems, in order to build a baseline for treatment studies. Norit Row 0.8 SUPRA, Norit CA1 and Norit SX2 were selected based on their surface functional groups. From commercial reports, Norit Row 0.8 SUPRA is a popular oxidized AC, prepared by Soxhlet extraction. In brief, 9g raw AC is reacted with 5M HNO_3 for 3 hrs with reflux. Obtained solids are then washed by distilled water until neutral pH, and dried at 110 °C for 24 hrs. Norit Row 0.8

SUPRA is popular in water treatment and has strong oxidation groups. Norit CA1 and Norit SX2 are both nitrogenized ACs. Norit SX2 is made from peat and is a multi-purpose activated charcoal, which is steam activated and acid washed. Norit CA1, activated from wood and is very suitable for the purification of highly colored and/or foaming liquids in the food and beverage industry. Norit CA1 combines an excellent adsorptive capacity with excellent filtration characteristics. To compare with untreated ACs, C2889 (raw AC without any treatment) and C5510 (raw AC after acid washing) were also purchased as control groups.

Different active materials were later prepared to utilize different surface modifications and tested through the same procedures. All treated acids were tested through ICP-AES to obtain ion concentrations. The accumulated carbon wastes were combined with initial filtered precipitates, and refined to obtain PSC precursors at the end.

5.2.2. Nitrogen-doped carbon xerogel preparation

Carbon xerogel (CX) has been reported to remove Pb, Zn and Cu in water treatment, and nitrogen-doped CX (NCX) was reported with the performance 1.97, 1.67 and 1.64 times of that of CX.[214] Because NCX materials have good stability in strong acidic conditions and can form high surface area 3D structures, NCX was prepared here for waste sulfuric acid treatment.

The preparation method is summarized in Figure 5-1. In brief, NCX was prepared by carbonization of phenolic resin with melamine modification. 0.0584 g sodium carbonate was used as catalyst in the condensation reaction, and 9.09 g resorcinol and 1.5 L 37% formaldehyde water solution were introduced to the reaction for CX preparation. To form nitrogen groups, 3 g melamine was added

for NCX preparation. After washing and drying the obtained solids, the carbonization process was controlled at 700 °C in argon environment. The heating rate was set at 2 °C/min during the temperature increase, and natural cooling was used during the cooling-down phase. The prepared NCX was characterized by FE-SEM to study the morphology and BET to find the surface area. Filtration and adsorption were tested to compare the ion removal performance.

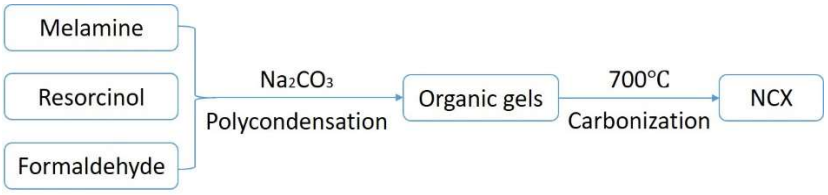

Figure 5-1 Preparation method for nitrogen-doped carbon xerogel.

5.2.3. Sulfur-rich MOF preparation

Based on the surface functionalization summary at the beginning of the section, it is reasonable to consider sulfur-rich adsorption materials with functionalized ligands to target Fe, Cu, Co and Ni ions, and MOF is a possible choice.[215] Abney *et. al.* reported the In core sulfur functionalized MIL-68 MOF nanoboxes for removal of heavy metal ions in water.[216] To control the cost, as In precursors are expensive, Al cores were also prepared in this study, and sulfur functional groups were maintained.

To prepare MIL-68 in this study, 1.05 mmol $In(NO_3)_3$ or $Al(NO_3)_3$ and 1.05 mmol terephthalic acid were dissolved in 5 mL of DMF, and then heated at 100 °C with stirring for 1 hr. After cooling, white solids were collected by filtration, washed by DI water, and dried at 65 °C for 24 hrs. To prepare sulfur inserted MIL-68, the dried powder was then suspended in 10 mL water, and 5 mmol of Na_2S was added. The suspension was agitated overnight, and then centrifuged and washed by

water. The obtained solids were studied by FE-SEM and XRD to understand the crystal characteristics and tested through adsorption.

5.2.4. GO membrane preparation

GO has large amount of oxygen groups and can be easily modified by other functional groups. Because oxygen groups are of interest for ion removal, GO was tested for acid treatment. To enhance the interaction between ions in the acid and the GO surface, a membrane design was used, as demonstrated in Figure 5-2, based on published methods.[217]

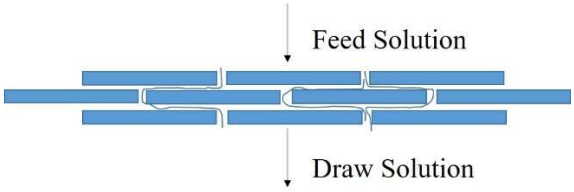

Figure 5-2 Schematic of forced interaction with GO during filtration

To prepare GO membranes, aqueous GO solution was firstly prepared at concentrations of 20, 40 and 60 mg/L. Then the solution was filtered through a cellulose membrane (Pall) while a vacuum drawing force was applied on the back of the cellulose membrane. After the filtration, GO films were dried and obtained at 65 °C. Before using the membrane, the cellulose back layer was dissolved by floating on water to release GO membrane. To prevent the dissolution of GO from interfering later tests, large flakes of GO were used and a Whatman™ Anodisc™ 25 membrane (alumina-based, pore size 20 nm) was added below the GO membrane to serve as a substrate. For each membrane, 20 mL waste sulfuric acid was filtered, and both single pass (one-time filtration) and double pass (two-time filtration) were tested. Also, to compare the membrane design and adsorption design, the same amounts of GO were tested following adsorption procedures.

5.2.5. CDI system preparation

CDI provides an extra electric field, which may potentially increase surface metal ion adsorption. To improve the adsorption kinetics in the treatments, CDI systems were designed and built to process acids. In this work, a sandwich structured CDI cell was designed, with two pieces of graphite foils as back electrodes and Norit SX2 AC as the active material. Considering lead ion is not the primary concern, lead plates were fabricated by our partner company and used as comparison electrodes.

The CDI cell was set flat with flow feeding top-down. CHI 760D electrochemical station was connected to the chamber with working electrode on anode and counter electrode and reference electrode on cathode. A peristaltic pump was used to provide driving force and was set to 50 rpm with a flow rate at about 2~3 mL/s. 20 mL of original acid was tested for each experiment in a circular system. It took about 5 seconds for the CDI cell to fill up and about 15 seconds for the 20 ml acid to finish a circle. The voltage of 1 V was applied when acid flow stabled, and 2 mL sample was drawn by a syringe pump immediately after 5 min accumulation from the beginning and was considered the average of 5 min processing. Collected acid samples were later tested by inductively coupled plasma mass spectroscopy (ICP-MS) to find ion concentrations.

5.2.6. Solid lead reformation design

At the end of the study, all carbon wastes were combined and used as raw materials for refinements and recoveries. The chemical reactions were designed into three major steps, and the procedures are summarized in Figure 5-3.

To refine the lead solid wastes, firstly the solid wastes were heated at 1,000 °C. Carbon materials, polymer compounds and other contaminants were burned away at the high temperature and lead sulfates were decomposed following the reaction $PbSO_4(s) = PbO(s) + SO_3(g)$. Secondly, the obtained lead contents with small quantities of other metals were disolved in 10% nitric acid and solid impurities were filtered out. $PbO(s) + 2\ HNO_3(aq) = Pb(NO_3)_2(aq) + H_2O(aq)$. Thirdly, the dissolved lead ions can be precipitated out by potassium iodide and washed with ethanol. Other metal ions were considered to have higher solubility in water and ethanol, and were removed from precipitates. Water was strictly forbidden after ethanol washing, because of the requirements of solar cells. $Pb(NO_3)_2(aq) + 2KI(aq) = PbI_2(s) + 2KNO_3(aq)$.

Figure 5-3 Schematic of designed approach for ion collection and solar cell fabrication. Methods and images are obtained and organized based on earlier works.[150,151,218]

5.3. Results and discussion

5.3.1. Acid properties and commercial AC baseline

The original waste acid contains large amount of polypropylene, lead debris and other compounds from battery plates, as shown in Figure 5-4. Due to dissolved metal ions, the acid showed light

brown color after the filtration. The possible aggregates in the post-filtration acid were considered smaller than 0.7 μm and were suitable for the following ion collection process. Figure 5-5 shows specific gravity of the filtered raw sulfuric acid. The specific gravity was recorded at 1.14, and the corresponding concentration was ~20 wt.%. This acid was later used as originals for all treatments.

Figure 5-4 Raw waste acid pretreatment. Original waste acid was filtrated for later metal ion seperation. Filtered solids were introduced to lead material refinement.

Acid Volume (ml)	Mass (g)
10.0	11.1411
20.2	22.6553
30.5	34.4869
40.7	46.1772
49.6	56.5028
39.7	45.3211
33.7	38.4434
21.9	24.8013
7.6	8.4146

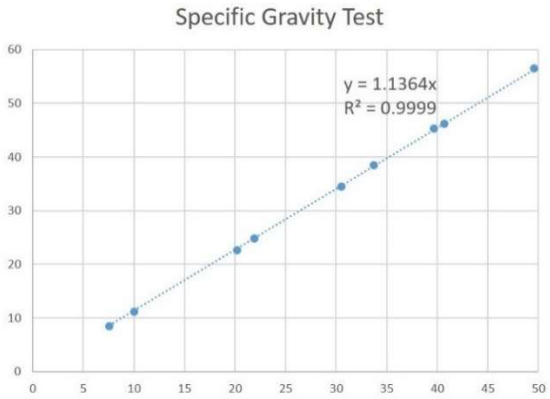

Figure 5-5 Specific gravity test for filtered sulfuric acid. Determined specific gravity is 1.14 in lab environment (20 °C), which corresponds to ~20 wt.% concentration.

The commercial AC performances in waste sulfuric acid are compared in Table 5-1, and the metal ion concentrations were tested by ICP-AES. The collected commercial ACs showed low performance or no performance at all. This can be explained by the surface modification activity in strong acids. General surface modifications were studied around neutral aqueous environment, and only limited functional groups were studied around pH ~ 1. In strong acidic condition, these functional groups may be disabled. Moreover, some ion concentrations increased after treatments. For example, Norit Row 0.8 Supra resulted in a significantly increased Mn concentration after both adsorption and filtration treatment. This may be because AC manufacturing uses biomass or impure carbon sources, and the metal ions in the AC were released in the strong acidic condition. The phenomenon can be explained by C5510 outperforming C2889 and Norit SX2 outperforming Norit CA1.

Table 5-1 Commerical AC performance used as a reference for adsorption and filtration.

	Fe (ppm)	Cu (ppm)	Zn (ppm)	Mn (ppm)	Ni (ppm)
Original	**152.26**	**60.09**	**19.45**	**0.25**	**4.28**
C2889 filtration	158.29	59.90	19.92	0.61	4.31
C2889 adsorption	161.85	59.47	19.84	0.92	4.26
C5510 filtration	152.93	60.06	19.94	0.25	4.31
C5510 adsorption	152.57	59.79	20.22	0.26	4.28
Norit SX2 filtration	152.00	59.51	19.85	0.26	4.27
Norit SX2 adsorption	152.03	59.16	19.84	0.26	4.26
Norit CA1 filtration	153.27	60.11	20.08	0.36	4.31
Norit CA1 adsorption	153.03	59.87	19.86	0.32	4.32
Norit Row 0.8 Supra filtration	159.94	60.09	20.09	0.69	4.34
Norit Row 0.8 Supra adsorption	168.42	60.04	19.52	1.29	4.31

Based on commercial AC comparisons, the challenge of any ion removal from concentrated sulfuric acid is significant. Also, the tests highlighted the importance of acid washing for acid treatments. Concluding from commercial AC tests, any ion removal of prepared materials was considered effective. Additionally, ICP-AES tests showed the original solution has a Pb(II) concentration of 1.25 ppm, which is significantly lower than those of Fe(II), Cu(II) and Zn(II). This is understandable, because most Pb(II) was precipitated and filtered during the initial filtration. To recover the acid, Fe(II) was the main issue.

5.3.2. Nitrogen-doped carbon xerogel performance

The obtained solids were aggregated together as blocks, after carbonization processes. FE-SEM images were taken and small ball structure was found under a high magnification, as shown in Figure 5-6. BET plots of NCX (Figure 5-7) show the material contains both micropores ($P/P_0 < 0.1$) and mesopores (Type IV, $P/P_0 > 0.6$), which is a preferred distribution, as mesopores have better permeability and micropores help the adsorption process of ions. The BET surface area is 572.0 m^2/g, which is comparable with common ACs.

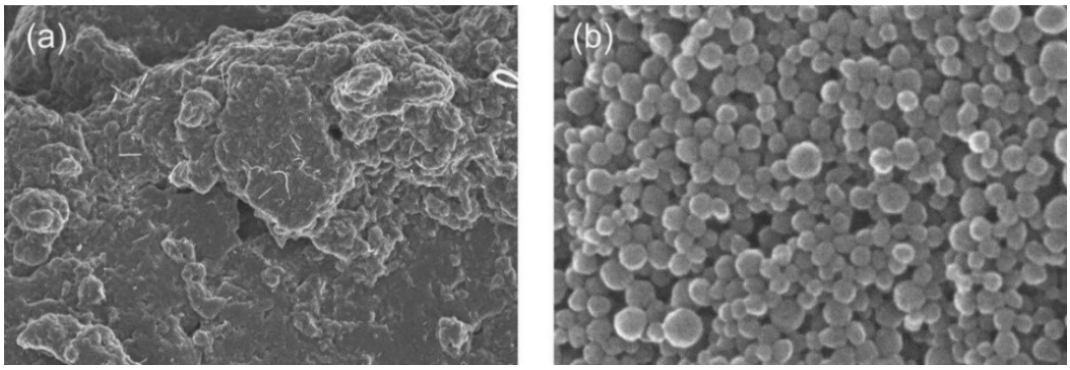

Figure 5-6 FE-SEM images of as-prepared NCXs. (a) at low magnification (×400) and (b) at high magnification (×500K).

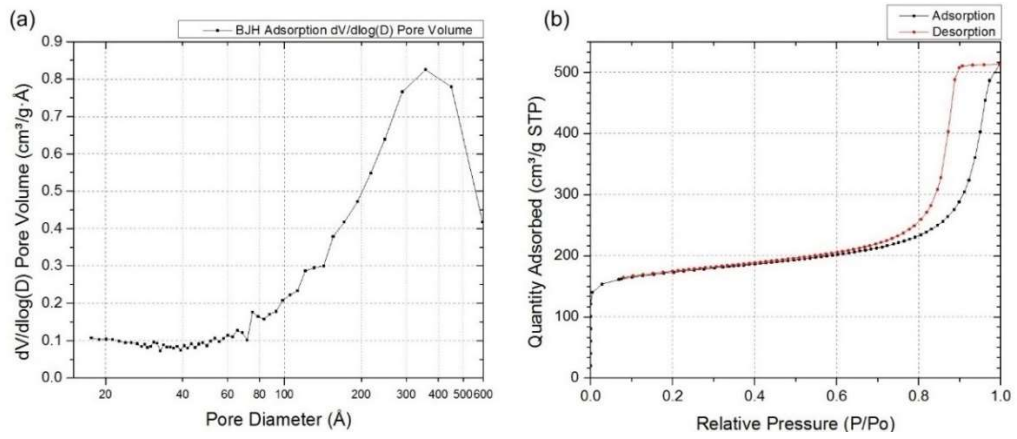

Figure 5-7 (a) BJH adsorption dV/dlog(D) pore volume and (b) isotherm linear plot of as-preapred carbon xerogels.

The ion concentrations after adsorption and filtration processes were tested by ICP-AES and reported in Table 5-2. No contaminations of reagent ions were observed. However, the removal of metal ions was still highly limited, and the as-prepared NCX only gave a small concentration decrease of Fe, which can be buried in the testing standard deviations. Similar to the trend of commercial ACs, the active sites on NCXs were occupied by high concentrations of protons in the strong acids. During the initial interaction between NCX functional groups and ions, the positively charged protons saturate the surface of NCXs more quickly, because protons have a much smaller diffusion constant than metal ions. The saturation time in the tests was shorter than filtration time, which leaded to a similar result between filtrations and adsorptions. To improve the removal performance, more quantity or more effective functional groups should be modified to the surface.

Table 5-2 Carbon xerogel based adsorption and filtration performance

	Fe (ppm)	Cu (ppm)	Zn (ppm)	Mn (ppm)	Ni (ppm)
Original	**152.26**	**60.09**	**19.45**	**0.25**	**4.28**
NCX filtration	149.93	59.39	19.56	0.25	4.23
NCX adsorption	151.91	59.68	19.90	0.25	4.26

5.3.3. Sulfur-rich MOF performance

Sulfur-rich MOF showed possibilities to increase the amounts of functional groups and test out other groups. In FE-SEM images, the indium core MIL-68 (Figure 5-8a) shows flake-and-rod structure and aluminum core MIL-68 (Figure 5-8c) starts forming cubic crystals. After being treated by sulfur, both MIL-68 crystals started aggregating together and forming larger particles (Figure 5-8b, d). Due to insufficient conductivity, significant charging can be observed for all samples. To verify their porous structure, BET was tested and found 58.19 m^2/g for indium core MIL-68 and 8.54 m^2/g after sulfur inserted. The aluminum core MIL-68 shows a high surface area of 1,244.4 m^2/g before and 81.43 m^2/g after sulfur insertion. All four MOF nanoboxes have major pore sizes smaller than 4 nm, which are mostly micropores.

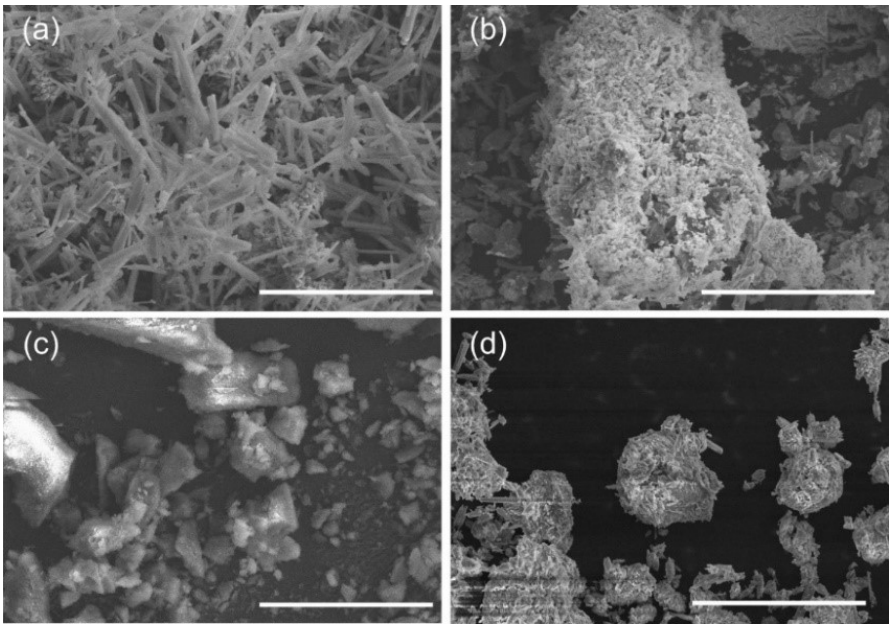

Figure 5-8 (a) MIL 68 (indium core); (b) MIL 68 (indium core) with sulfur; (c) MIL 68 (aluminum core); (d) MIL 68 (aluminum core) with sulfur; scale bar is 50 μm for all figures.

The XRD test was done to verify the sulfur insert. As compared in Figure 5-9, the crystallization conditions significantly worsened after treating in sulfur for both indium and aluminum cores, because of the random insert of sulfur ions.

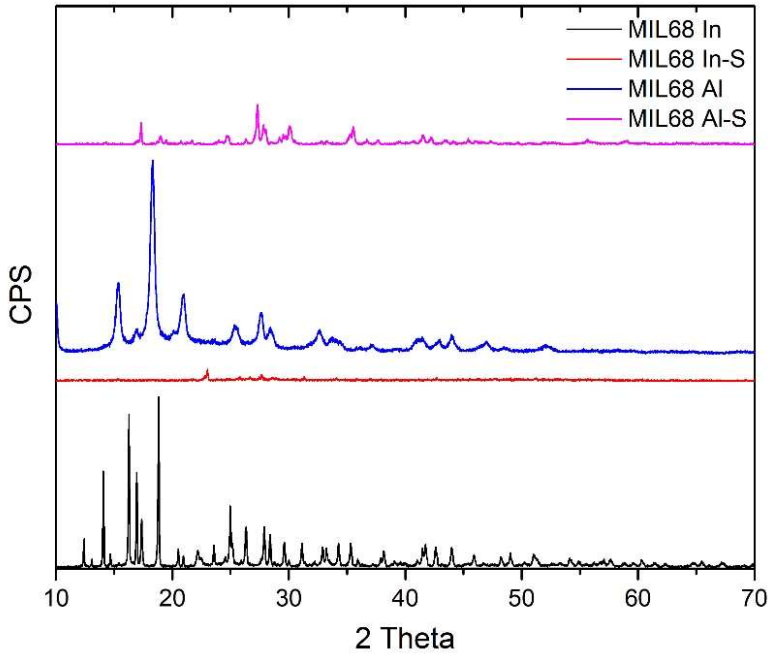

Figure 5-9 XRD comparison of four MOF materials.

ICP-AES was tested and specifically focused on Fe concentrations. The comparison shown in Table 5-3 demonstrates that the four types of MOF prepared here have little effect on iron removal. MIL-68 with aluminum core shows weak removal of Fe ions. However, due to the stability of MOFs in acid solution, weight loss of adsorbent was observed. The prepared MOFs outperformed commercial ACs, but the results were still unfavorable to perform possible ion removal and waste acid recovery. To further understand the ion interactions with surface functional groups, forced interaction is necessary.

Table 5-3 As-prepared MOF material adsorption performance.

Adsorption Material	Iron Concentration (mg/L)	RSD (%)
Original	**150.1**	**0.53**
MIL-68 (indium core)	150.5	1.03
MIL-68 with sulfur (indium core)	151.5	0.54
MIL-68 (aluminum core)	144.4	1.18
MIL-68 with sulfur (aluminum core)	149.2	0.30

5.3.4. GO membrane performance

GO membranes were designed to perform forced interactions between ions in the acid and oxygen groups on the GO surface. With a varied initial GO concentration, different thicknesses of GO membranes can be prepared. 20 mg and 200 mg GO membranes with an area of 15.9 cm^2 were compared in Figure 5-10. However, extra GO loading led to fragile membranes, and high-GO-loading membranes can be easily cracked and thus were considered unsuitable for acid filtration.

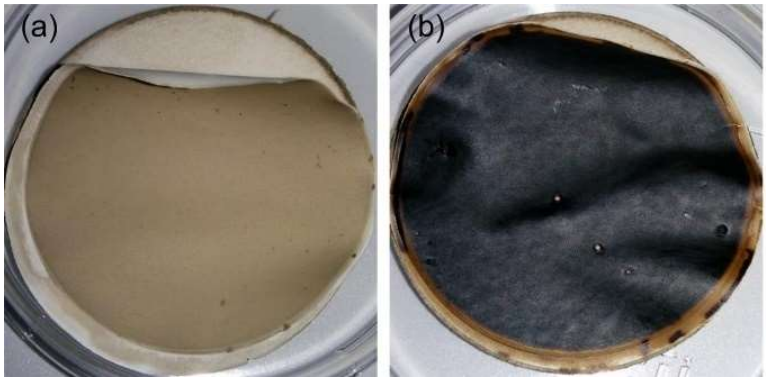

Figure 5-10 GO membrane with 20 mg (a) GO and 200 mg (b) GO.

To validate the designed forced interaction, the ICP-AES data are compared in Table 5-4. Ideally, double passes gave more interaction opportunities compared with single passes, and extra material

loading was expected to have enhanced removal performance. However, the GO membrane design did not work for ion removal in waste acid as well. Fe concentrations were slightly increased for double passes compared with single passes and for high-GO-loading membranes compared with low-GO-loading membranes. This can be explained by the evaporation of water during the filtration process. GO membranes have low penetration rates, which amplifies the evaporation factor in the processes.

Table 5-4 As-prepared GO membranes and their performance.

	Fe (ppm)	Cu (ppm)	Zn (ppm)	Mn (ppm)	Ni (ppm)
Original	**152.26**	**60.09**	**19.45**	**0.25**	**4.28**
GO with nitrogen doping	153.22	59.98	19.65	0.31	4.33
GO membrane 20 mg/L single pass	152.02	60.08	19.58	0.25	4.29
GO membrane 20 mg/L double pass	153.77	59.69	19.28	0.25	4.28
GO membrane 40 mg/L single pass	153.18	59.20	19.28	0.25	4.25
GO membrane 40 mg/L double pass	154.07	60.27	19.54	0.25	4.31
GO membrane 60 mg/L single pass	153.87	59.39	19.30	0.25	4.25
GO membrane 60 mg/L double pass	155.15	60.69	19.70	0.26	4.34

5.3.5. CDI removal of metal ions in waste acid

To improve the adsorption kinetics of the ion removal processes, CDI cells were designed and tested. The charging and discharging current vs. time for 1 cycle is shown in Figure 5-11. During

this test, AC coated electrodes failed during initial charging, because the coated material was peered off and suspended into the acid, and the discharge was unable to record. The failure of AC coating may result from dissolution of used PTFE binders. Pure graphite foil also failed after 2 min charging. This again raises concerns of material stability in strong acidic condition. Overall lead plates showed higher current, which is due to the high conductivity of the metal plates.

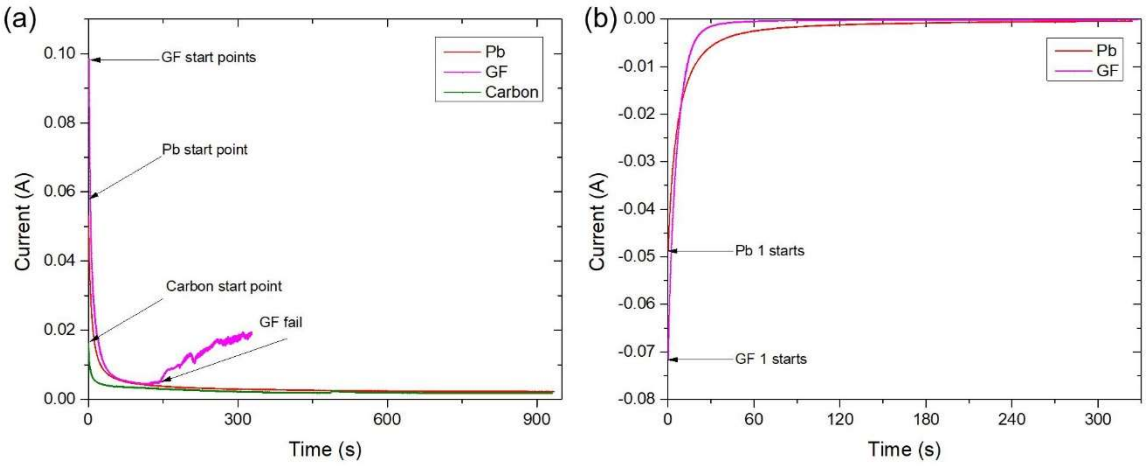

Figure 5-11 Charging at 1 V (a) and discharging at 0 V (b) for different electrodes in the CDI system. Pb: lead plate; GF: bare graphite foil; Carbon: Norit SX2 with 15% PTFE binder on GF.

Table 5-5 CDI ion removal performance in waste sulfuric acid.

	Mn	Fe	Co	Ni	Cu	Zn	As
Original	**0.297**	**155.1**	**0.0772**	**4.15**	**55.7**	**17.7**	**0.245**
Carbon paper (uncoated)	0.299	154.2	0.0711	4.46	55.1	18.2	0.235
Carbon paper (coated with Norit SX2)	0.300	151.6	0.0710	7.60	57.6	17.5	0.224
Lead plate	0.346	166.7	0.0788	4.52	45.2	19.8	0.252

CDI performance for the first 5 min average was tested by ICP-MS and results are compared in Table 5-5. No removal can be observed for any electrode materials, while contaminants were found

from the acid treated by the lead plates. These extra ions might come from the dissolved plate materials, which is always modified for battery use. The poor performance again can be understood by the dominating proton concentrations.

5.3.6. Reformed lead material characterization

Although the pure acid ion removal was not successful, the reformation of recycled lead materials was successfully demonstrated. Before the refinements, the contents of the obtained filtered precipitates were studied. XRD results in Figure 5-12 show that the solid wastes from consumed sulfuric acid were mainly in the form of $PbSO_4$ by peak-match studies. Weak $Pb_2Sb_2O_7$ peaks can also be observed because Sb is always used as a conditioner for Pb plates with high performance. The high content of $PbSO_4$ fitted the designed procedure for the refinements.

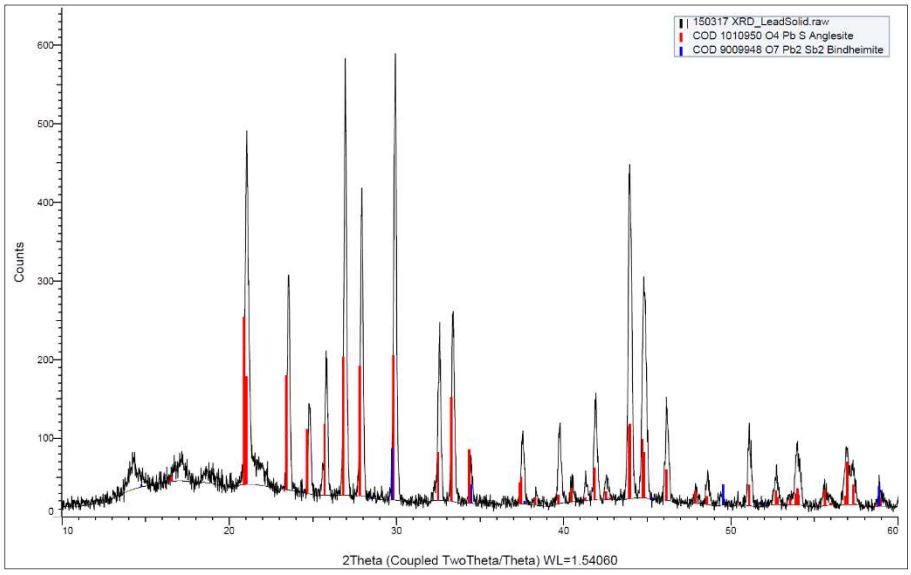

Figure 5-12 XRD peaks of collected waste solid. The red lines show the standard peak positions of $PbSO_4$ anglesite phase. The blue lines have a similar position and may be possible as Sb is sometimes used as additives in the lead-acid batteries.

After refinements and purifications, the production of PbI_2 was estimated around 25 mg per 100 mg raw waste from filtered precipitates. The most contents in the solid wastes are carbon or organic compounds. The collected PbI_2 is shown in Figure 5-13.

Figure 5-13 Reformed lead iodide for solar cells from waste lead solids.

To verify the purity of obtain PbI_2, XRD was performed and a comparison with commercial perovskite precursor is shown in Figure 5-14. The reformed PbI_2 shows identical peaks to commercial standards. Here the success of the reformation can be concluded.

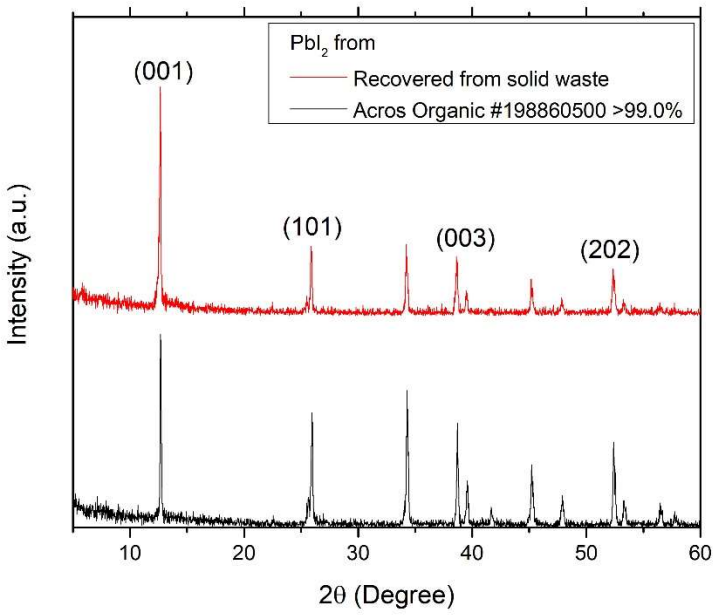

Figure 5-14 XRD comparison of commercial material and recovered material. Peak of (101) phase proves this is powerder sample, instead of thin film sample. Peak positions match very well and prove high purity.

5.4. Conclusions

The difficulties to collect metal ions in strong acidic condition can be summarized in following two major aspects. First, large quantities of protons in the fluid are competing with metal ions, and will always occupy and disable active sites in regularly designed adsorption and filtration systems. General water treatment suggests relatively higher adsorption kinetics for metal ions over protons, which is extremely difficult in concentrated acid, because the protons have a ~10^6 times higher concentration than that in water. A better designed CDI system can proactively improve the kinetics, but the material stability should be considered for strong acids. Second, most functional groups can decompose or dissolve in acid, which limits material options. For example, thiol-based MOF materials are widely reported with high heavy metal ion selectivity;[216] however, the framework dissolves in the acidic environment.

This work explored the difficulties for waste sulfuric acid recovery and designed an approach to utilize collected lead wastes for PSC use. Despite the limited performance of studied materials and structures, the results lay out the requirements and guidelines for future acid treatment methods using 2D nanomaterial properties and other material modifications. The explored approaches can be easily adapted to wastewater treatments in a low-cost and high-volume system.

Chapter 6. Capacitive Deionization Based Lead Recovery from Contaminated Water and Reformation for Perovskite Solar Cells

6.1. Introduction

Although CDI has shown little to no effect in removing Pb^{2+} in acidic solutions, CDI has demonstrated high potentials in removing heavy metal ions such as Pb,[219,220] Cr,[147,221] Cu,[222] Cd[223] and As[224] in low acidic aqueous matrix. With the significantly lower competition from protons in water than in acid, the selectivity of CDI is necessary to compare against other cations in water, for example Ca^{2+} and Mg^{2+}.

Various CDI architectures have been studied to enhance CDI performance in water treatment, such as flow-through and flow-between with ion-exchange membrane variations.[225] Flow-between model is widely used due to its simple configuration and its suitability for studying material performance.[226,227] At the same time, different water-feeding strategies such as batch mode and single-pass mode have been investigated; the batch mode requires cycling water in a tank for multiple cycles to achieve high removal performance, while a single-pass flow allows water to pass the system.[149] Compared with batch modes, the single-pass one is less investigated but closer to practical application due to its continuous feeding of constant ion concentrations.[228,229]

Improving CDI selectivity to Pb^{2+} is essential to both treatment of drinking water and lead recovery for perovskite precursors. Current techniques and studies of CDI are mostly focused on desalination. The preliminary data in acid study have shown strong selectivity of Pb^{2+} by using functionalized graphene materials. In the research of Liu *et al.*[230], nitrogen-doped graphene was used as the electrode material, and nitrogen groups were functioned as active removal probes. A

high selectivity was demonstrated by nitrogen-doped graphene, but the high annealing temperature to treat graphene led to a significant mass loss, which may result in high product cost. Sulfur treatment is another suitable approach based on previous study. GO can be easily reduced by thiourea through hydrothermal approach,[231] and a self-assembly of thiourea with GO has been reported using low temperature hydrothermal reaction.[232] The resulted rGO surface has been identified with rich sulfur groups and is suitable for water treatment.[233]

In this study, a flow-between and single-pass CDI device is designed, and sulfur-treated GO based active carbon material is prepared to remove Pb^{2+} selectively. Furthermore, the collected Pb^{2+} ions are successfully recovered to perovskite precursors with the same material characterizations and photovoltaic performance.

6.2. Experimental methods

6.2.1. Carbon material preparation and electrode fabrication

All chemicals were purchased from Sigma-Aldrich, unless otherwise mentioned. Lead(II) nitrate, calcium chloride dehydrates, and magnesium chloride hexahydrate were used as Pb^{2+}, Ca^{2+} and Mg^{2+} source. Graphene oxide was prepared through a modified Hummer's method.[170] The activated carbon was YP50F (Sanwa). Anion-exchange membrane (AEM, FAS-PET-130) was purchase from FUMATECH.

The sulfur treatment of carbon materials was carried out by adding 1:1 weight ratio thiourea to mixed carbon materials with different GO dosage, and prepared to 10 mg/mL solution in DI water. GO dosage was controlled at 0 wt.% (CS), 12.5 wt.% (12.5GCS), 25 wt.% (25GCS), 50 wt.%

(50GCS) and 100 wt.% (GS). Each 50 mL solution was then transferred to 100 mL autoclave and a hydrothermal reaction was carried out at 180 °C for 24 hrs. The product was then filtered through Whatman® GF/F glass fiber membrane and washed by DI water, before vacuum dried at 60 °C overnight.

Electrodes were prepared using a doctor blade method. Carbon slurries were prepared by mixing prepared carbon materials with carbon black and polyvinylidene fluoride (PVDF) binder (72:8:20, by weight) in N-methyl-2-pyrrolidone (NMP). The resulting slurry was coated onto a graphite foil, dried under vacuum at 80 °C overnight, and cut to 4.2×4.2 sq. in. to obtain single-side electrodes, as anode for CDI tests. A pure activated-carbon-based double-side electrode was created as cathode, and was sandwich between two cathode electrodes to complete a CDI cell.

6.2.2. CDI setup and testing

A simulated water was prepared with 10 ppm Pb^{2+}, 10 ppm Ca^{2+} and 10 ppm Mg^{2+} in Milli-Q® type 1 ultrapure water. The CDI performance was evaluated through a one-pass flow cell with layout show in Figure 6-1, and the flow rate was controlled by a peristaltic pump at 23 mL/min. Anion-exchange membrane was used in this study to enhance the discharge performance, while cation-exchange membrane was not used to fully expose the treated material. The voltage was applied through the CHI 670E electrochemical workstation. The conductivity was monitored real time with Horiba F74BW system and pH was recorded for each sample point. Collected samples were tested by Perkin Elmer optima 2100DV ICP-OES to analyze ion concentrations.

The CDI tests for each sample include two steps. The first step started with 5 min wetting, 1 h charge and 10 min discharge as the activation cycle. Water samples were collected at different time point, to understand overtime CDI behavior. The second step consisted 6 cycles of 8 min charge and 2 min discharge to evaluate cycling performance. Water samples were collected as an average for each charge or discharge to evaluate CDI cycling performance.

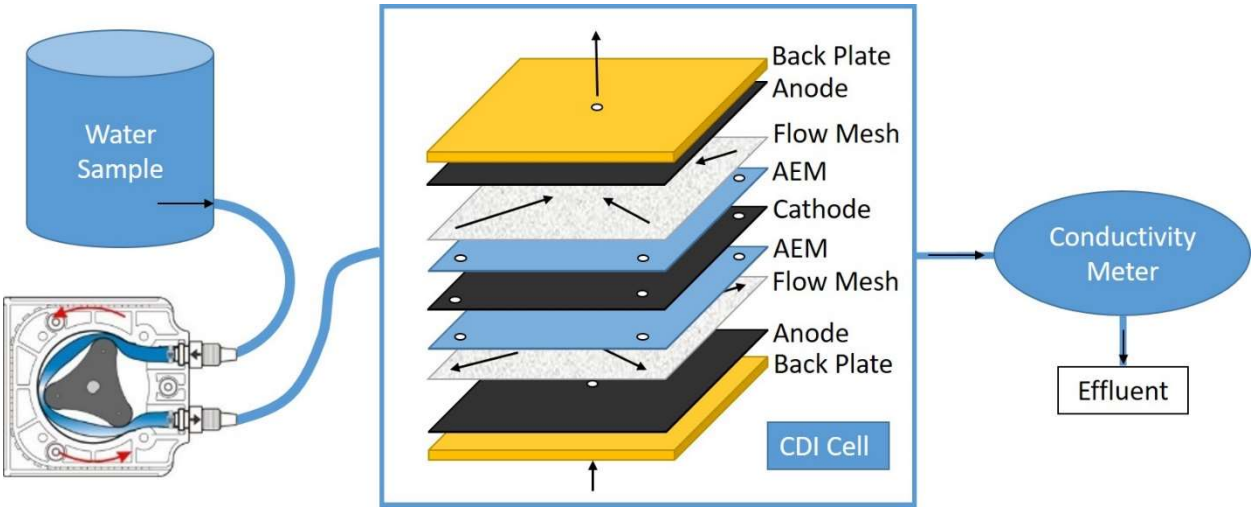

Figure 6-1 Schematic of CDI flow systm layout.

6.2.3. Material reformation and solar cell testing

Before the reformation process, the collected effluent was tested by ICP-AES, and the estimated Pb^{2+} concentration is ~50 ppm. For every 2 L effluent of CDI, 10 mL saturated sodium carbonated aqueous solution was added. After settling for 10 min, the solution was filtered through Pall® Metricel ® membrane (GN-6 0.45 µm 47 mm). The collected white precipitates were dissolved into 10 mL 20% acetic acid and then filtered through Millipore Fluoropore™ PTFE (0.2 µm 25 mm) membrane. Nitric acid was avoided in this process, to prevent the oxidation of I^-. To reform PbI_2, the filtrate was heated to 70 °C, and 0.177 g KI was slowly added over 30 s with stirring. The

KI was calculated with 25% overhead to not only ensure the precipitation, but also limit the formation of $[PbI_4]^{2-}$ complex. After cooling the solution to room temperature, the formed PbI_2 was filtered through PTFE membrane, and washed by IPA. The collected PbI_2 was then dried under vacuum overnight.

The recovered PbI_2 was combined with MAI and MABr (1:0.2 molar ratio) to prepare 1M $MAPb(Br_{1-x}I_x)_3$ precursor solution in GBL/DMSO (7:3 v/v). The solar cell fabrication process and tests are similar to that of Section 3.2 in Chapter 3. In brief, a blocking layer was constructed using Ti-isopropoxide as precursor through spin coating and annealing. Then a mesoporous layer was coated by spin coating a 2:9-ethanol-diluted commercial Titania paste, and gradually annealed. The perovskite layer was constructed by spin coating the recovered lead precursor solution, and surface engineered with drop casting of toluene. Spiro-OMeTAD was used as HTM, with LiTFSI, CoTFSI and 4tB as dopants. 60 nm Ag layer was thermally evaporated onto the back of the cell as current collector.

The solar cell made from recovered material was tested using a solar simulator (Newport 94021A) under AM 1.5G illumination in ambient air environment at 23 °C, with Newport 91150 as a reference cell. A Keithley 2420 source meter was used to scan the cells at the rate of 10 mV/s, and a non-reflective mask with area of 0.096 cm^2 was used to control the active area. The EQE was recorded with a 300 W xenon arc lamp as light source, Oriel Cornerstone™ 260 1/4 M double grating monochromator (Newport 74125) as light grader and Merlin™ Radiometer System (Newport 70104) as quantum counter.

6.3. Results and discussion

6.3.1. Electrode material comparison

The prepared sulfur treated carbon materials were first analyzed by XRD and Raman to study the modification. XRD was recorded with Bruker D8 Discover X-ray Diffractometer, and Raman was studied by Renishaw Inc. 1000B with helium neon laser at 633nm. Figure 6-2(a) shows the crystallization change before and after treatments. The intensity of peaks from activated carbon (AC) or GO varies, corresponding to different GO contents. Two wide peaks around 24° and 43° reveal the polycrystalline character of sulfur-treated carbon materials.[234] To understand the sulfur bonding with carbon material surface, Raman shifts are studied in Figure 6-2(b). Despite the high peaks of carbon signatures, three major C-S and S-H stretches are compared among different GO dosages. The weak peak intensity indicates a limited surface modification. A small increasing trend of S-H stretching intensity with increasing GO contents demonstrates an easier surface modification for GO and the importance of GO contents.

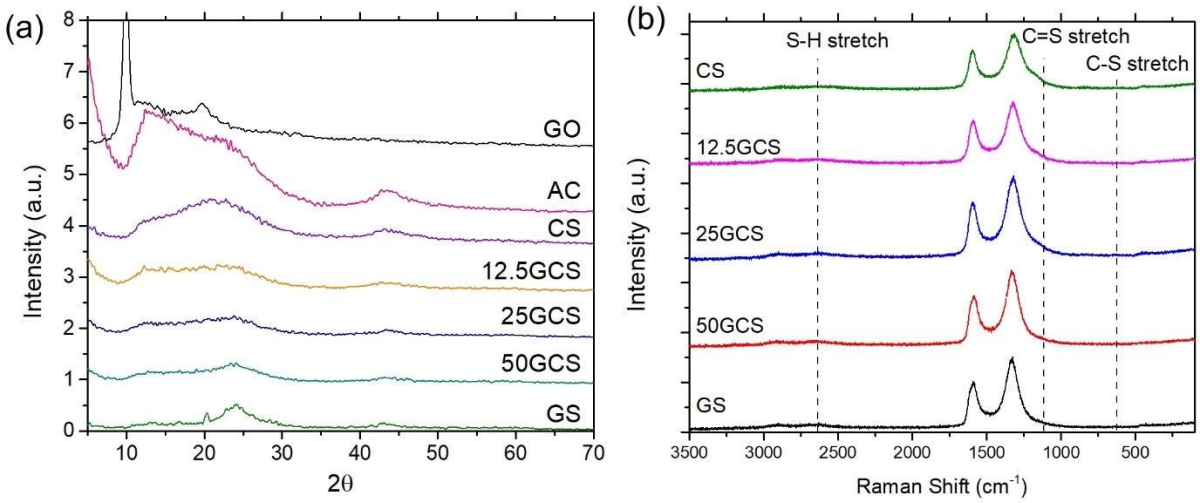

Figure 6-2 XRD (a) and Raman (b) study of sulfur-treated carbon composite with different GO dosage. Pure GO and activated carbon (AC) are compared in XRD study and demostrate the based line for peak positions without treatment.

SEM and EDS were then studied to verify the successful sulfur treatment. Using 25GCS as an example, the SEM image with GO, AC and carbon black is shown in Figure 6-3. The EDS mappings of C, O and S all show a uniform distribution. The sulfur content is then calculated from EDS spectra, and the atomic ratio of C, O and S for 25GCS is about 37:3.7:1. The low sulfur atom ratio agrees with the low Raman intensity. The atomic ratios of all prepared carbon materials are compared in Table 6-1 by normalizing atom percentage to S. In GS, a 8.7:1 C/S ratio is achieved compared with 219.6:1 in CS. Higher GO contents shows significantly higher S content, which is preferred for high selectivity. An interesting phenomenon is the O/S ratio remains close with the dosage of GO to AC. Because carboxyl and hydroxyl groups have positive effects on Pb^{2+} removal, existence of oxygen is not considered an issue in this study.

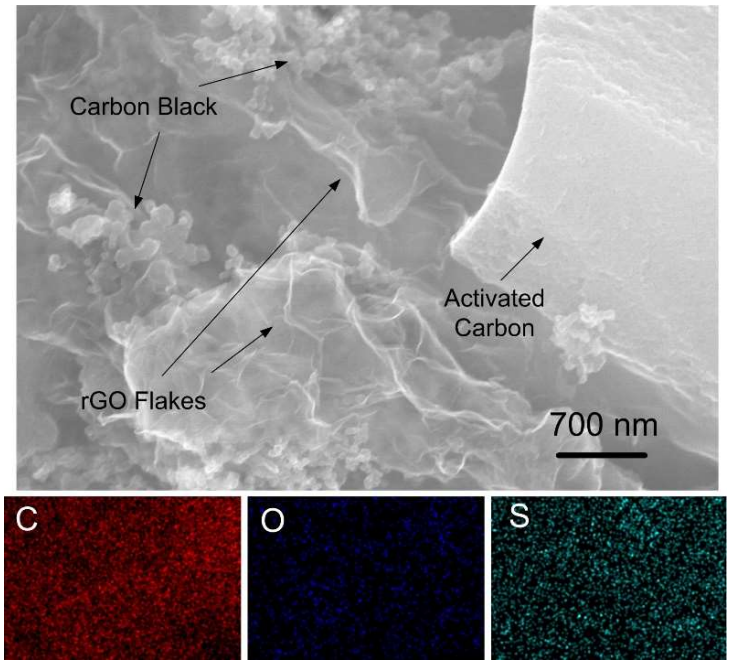

Figure 6-3 SEM image of 25GCS with EDS mapping of C, O and S to study elemental distributions.

Table 6-1 Atomic ratio of C, O and S determined from EDS by normalizing to S.

	CS	12.5GCS	25GCS	50GCS	GS
C	219.6	57	37	28.6	8.7
O	9.7	3.7	3.7	3.8	1.1
S	1	1	1	1	1

6.3.2. CDI performance comparison

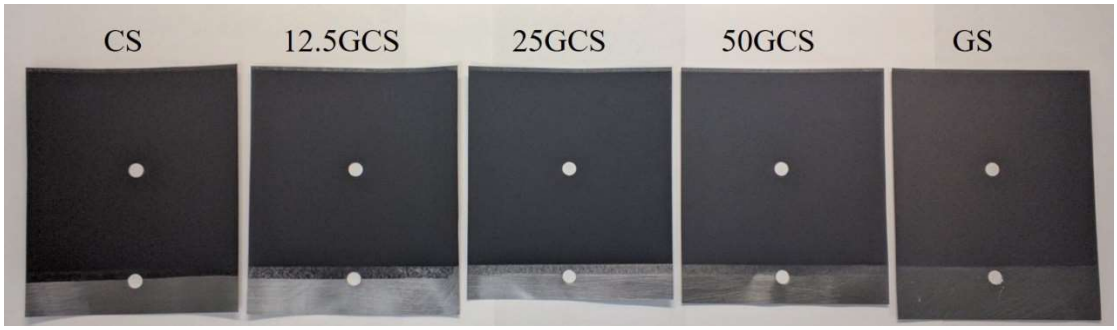

Figure 6-4 Coated electrodes for different content amount of graphene oxide. With the increasing graphene oxide amount, the color of coated surface turns from black to grey.

Table 6-2 Active material loading amount per unit area for each electrode

Material	CS	12.5GCS	25GCS	50GCS	GS
Loading (mg/cm^2)	2.10	3.51	2.07	2.13	0.73

To ensure a stable CDI performance, all coated electrodes were inspected visually for uniformity before tests. High GO content electrodes (GS and 50GCS) showed significant difficulties during the coating processes, due to the restacking effect of GO flakes. The stacked GO flakes result in small visible sheets on the electrodes, and can be dragged across or peered off, which decreases the coating quality. Figure 6-4 compares the coated electrodes with different GO contents. With the increasing GO dosage, the color of coated surface turns from black to grey, which is similar to the color change from carbon power to graphite. Active material loading is compared in Table 6-2.

Due to the coating difficulty, GS electrodes have a mass loading of 0.73 mg/cm^2 only, while other electrodes can be controlled around ~2 mg/cm^2. The limited coating quality and mass loading reduces the potential of using high GO contents for CDI tests.

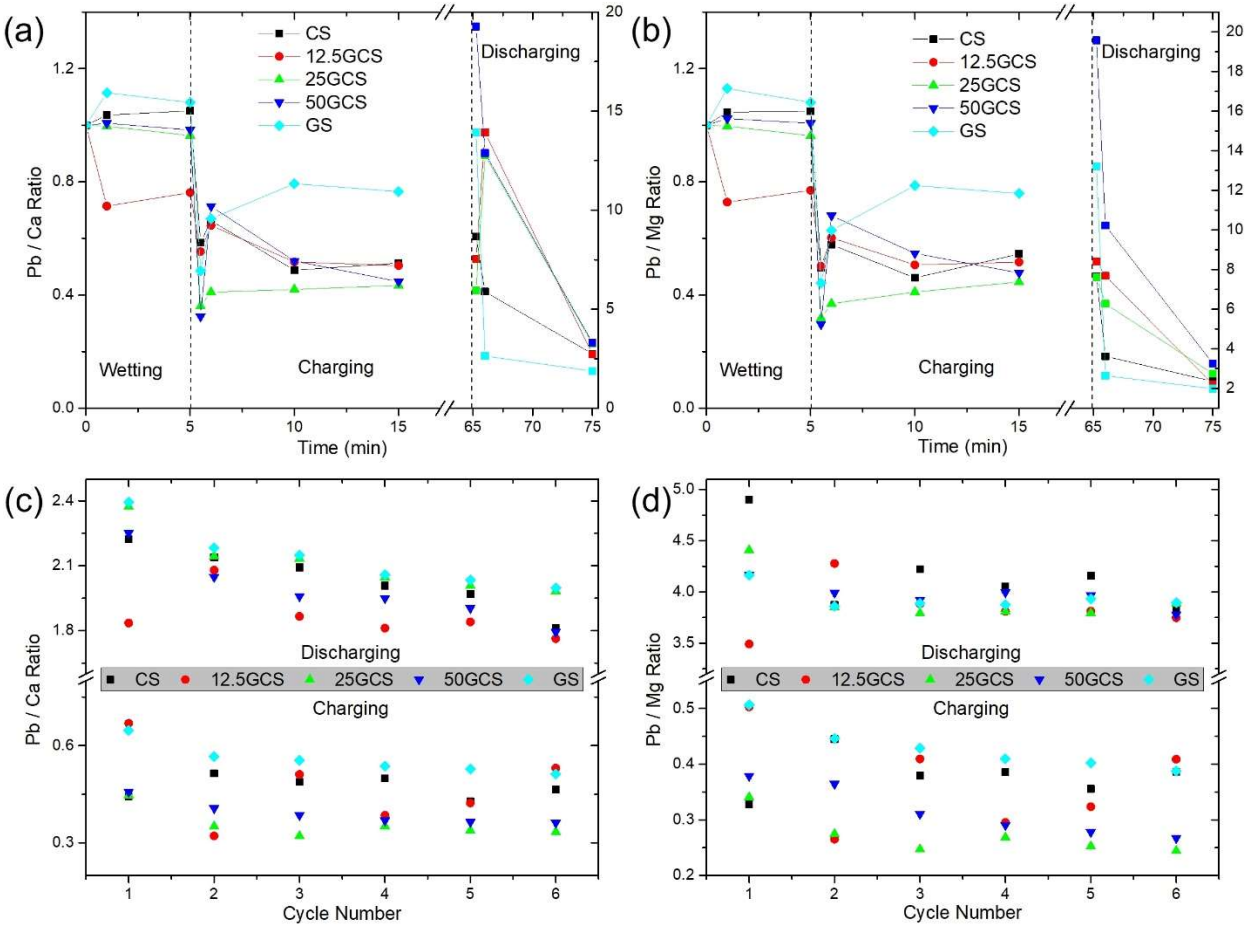

Figure 6-5 Selectivy of Pb against Ca and Mg for time-dependent studies (a, b) and cycling studies (c, d). (a, c) are Pb against Ca results and (b, d) are Pb against Mg results.

The selectivity of Pb^{2+} over Ca^{2+} and Mg^{2+} is studied by comparing the removal concentration following the definition in the research of Liu et al.[230] All data are reported in Figure 6-5. It is obvious that for all electrodes, Pb^{2+} removal rates are significantly higher than that of Ca^{2+} and

Mg^{2+}, which agrees with original material design. The selectivity performance against Ca and Mg shows similar trends, which can be explained by the similar chemical behavior of Ca and Mg. Among all five electrodes, 25GCS shows the highest selectivity of Pb against Ca and Mg for both over time and cycling studies. Earlier CDI studies[146] revealed that both micropores and macropores are essential for ion removal. Micropores offer additional surface area for ion collection and macropores provide channels for water flow. At the same time, higher GO contents can offer more active sites, but the surface area is limited. 25GCS balances the macropores ratio and the GO content. Additionally, GS demonstrates high selectivity at initial charging time, but the performance fades fast due to small mass loading. CS also shows selectivity to Pb, while the strength is limited by low sulfur-modified sites.

To study lead removal performance for each electrode, the overtime tests of all five types of electrodes are compared in Figure 6-6(a) for Pb^{2+} removal. The charging process is shown for the first 15 min, because the initial CDI behavior is more attractive for cycling study. During 5 min wetting process, a small variation in Pb^{2+} concentration is noted, which is resulted from the different adsorption kinetic and small variations in testing environment. The big difference for 12.5GCS can be explained by a bigger mass loading, which requires additional time for stabilization.

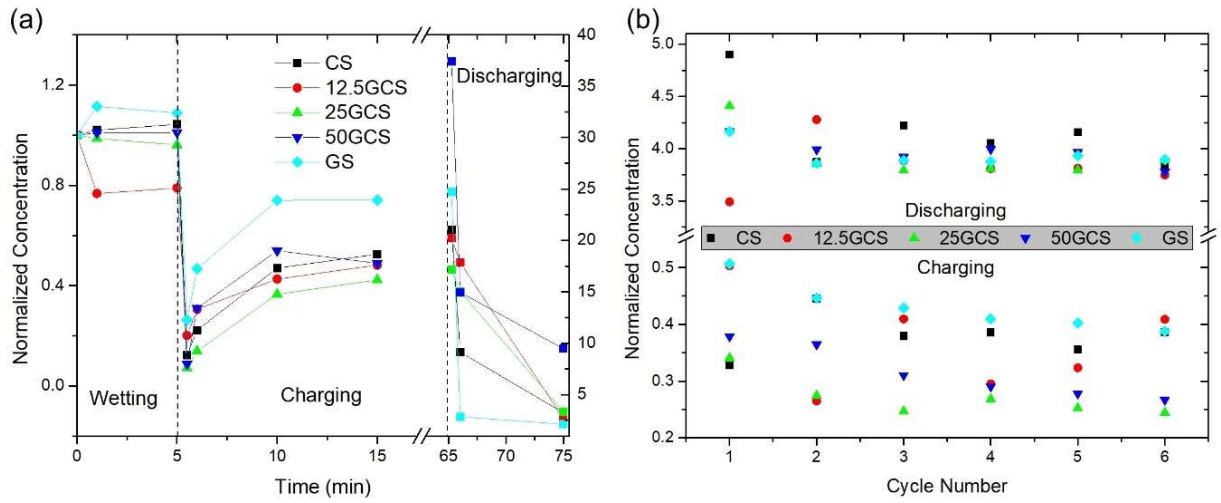

Figure 6-6 CDI results for (a) overtime results within 15 min charge and 10 min discharge and (b) cycling performance. All concentrations here are the lead concentration at each sampling point.

At the end of 5 min wetting, the Pb^{2+} concentrations are considered close to the original concentration, and a 1.2 V charging voltage is applied. GS electrodes show high removal of Pb^{2+} ions, which is benefiting from the high sulfur content; however, the removal rate quickly falls down due to the low coating quality and small mass loading. CS and all GO-doped electrodes shows a stable performance over charging period, while 25GCS maintains a high removal rate of Pb^{2+} over all time, which can be explained by good coating quality and high sulfur modification. During the 10 min discharge, all electrodes ejects over 100 ppm Pb^{2+}, which demonstrates the feasibility to use prepared electrodes to concentrate Pb^{2+} for easy recovery. The cycling performance shown in Figure 6-6(b) demonstrates a stable performance of 25GCS with a high removal rate for all cycles and stable discharge for recovery compared with other electrodes. This result agrees with previous analysis and proves that 25GCS has a suitable balance between coating quality and sulfur content, and is an outstanding candidate for lead recycling from contaminated water.

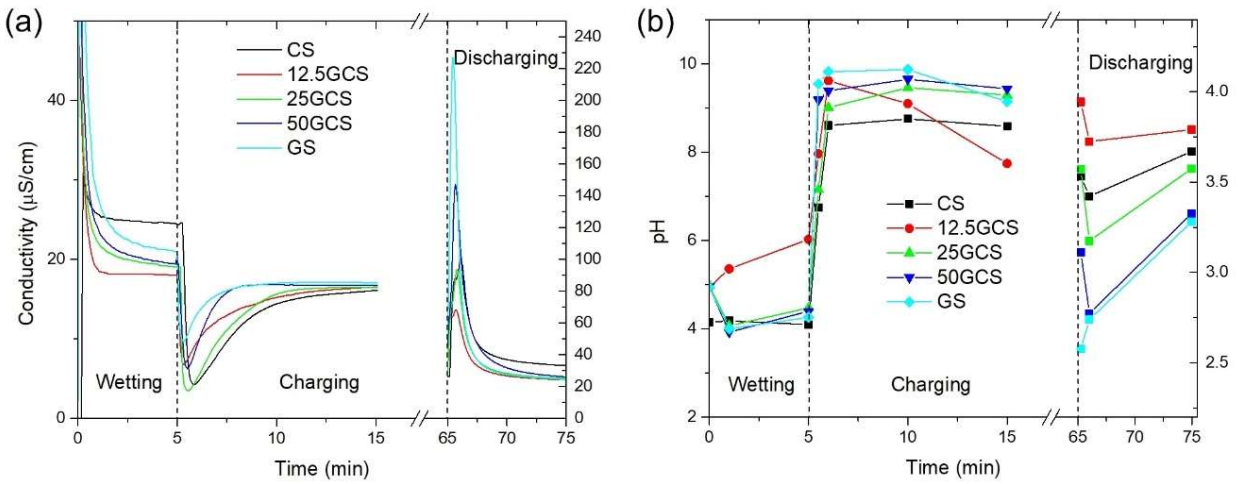

Figure 6-7 CDI behavior of different composites for (a) conductivity and (b) pH.

Conductivity and pH values are tracked for all tests to study the kinetics of removal. The conductivity in Figure 6-7(a) shows a similar trend to Figure 6-6(a), because conductivity is dependent on the total ion concentration in water, while Pb^{2+} concentration change is dominant in the total conductivity. The pH value in Figure 6-7(b) starts in acidic condition due to the hydrolysis of Pb^{2+} ions. With the high removal at the initial time points, pH quickly increases to ~10, which suggests the removal of Pb^{2+} may depend on the changing of hydrolysis environment of Pb^{2+} ions. The falling of pH value for 12.5GCS and GS also agrees with the decaying of Pb^{2+} removal rate, comparing Figure 6-7(b) with Figure 6-6(a).

6.3.3. Lead material reformation yield and solar cell performance

The effluent of discharge solution from previous 25GCS test was collected for lead recovery study. Before introducing any chemical agents, the concentration of accumulated solution was estimated around ~50 ppm through ICP-OES tests. For 2 L effluent, a total of 0.483 mmol Pb^{2+} is discharged, and the theoretic limit for PbI_2 formation is 222.6 mg. Considering the residual of PbI_2 in water

during the last filtration step, the maximum limit for collection is ~212.6 mg. The actual collected PbI_2 is 182.8 mg and a yield of 82% is achieved. For larger scale treatment, a higher quantity of effluent can be obtained. Because a big loss here is the dissolved PbI_2 in water in the last step, increasing the total accumulated effluent can increase the yield for future production.

The recovered PbI_2 is tested by XRD, and is compared with commercial PbI_2 in Figure 6-8(c). Matching XRD peak positions of recovered PbI_2 indicates similar crystallization quality as commercial product. The higher (101) peak over (001) suggests a stronger polymeric crystal structure, which may be resulted from crystallization process during drying and exceeding I^- in the crystal. Considering I^- loss in perovskite crystals during storage, exceeding I^- was not identified as an issue. To verify purity, 1 mg reformed PbI_2 sample was dissolved in 15 mL water with 2 wt.% HNO_3 as digesting media. ICP test shows the Pb concentration of 27.1 ppm vs Ca/Mg below ICP-OES detection limit. The purity of reformed PbI_2 is considered 99+%, and is suitable for PSC fabrication use.

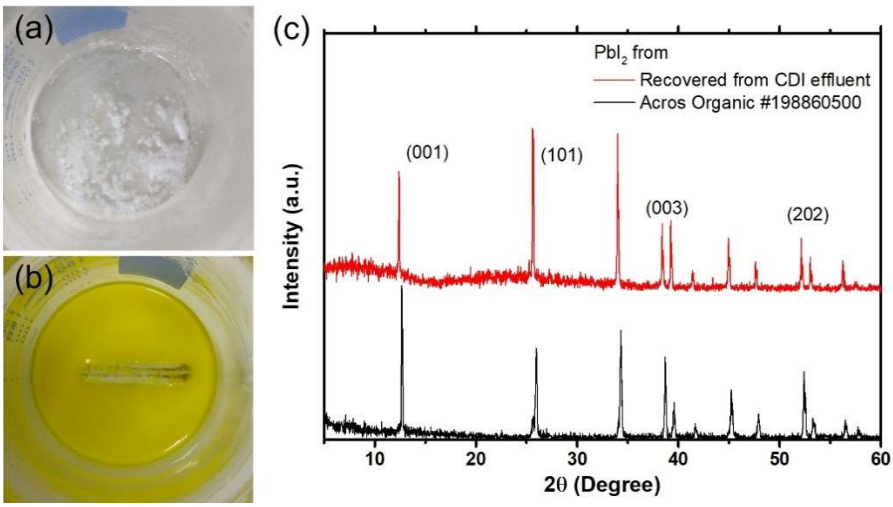

Figure 6-8 (a) The precipitated lead waste mainly in the form of $PbCO_3$ and (b) the precipitated PbI_2 before collection. The recovered PbI_2 material was compared with commecial PbI_2 in (c).

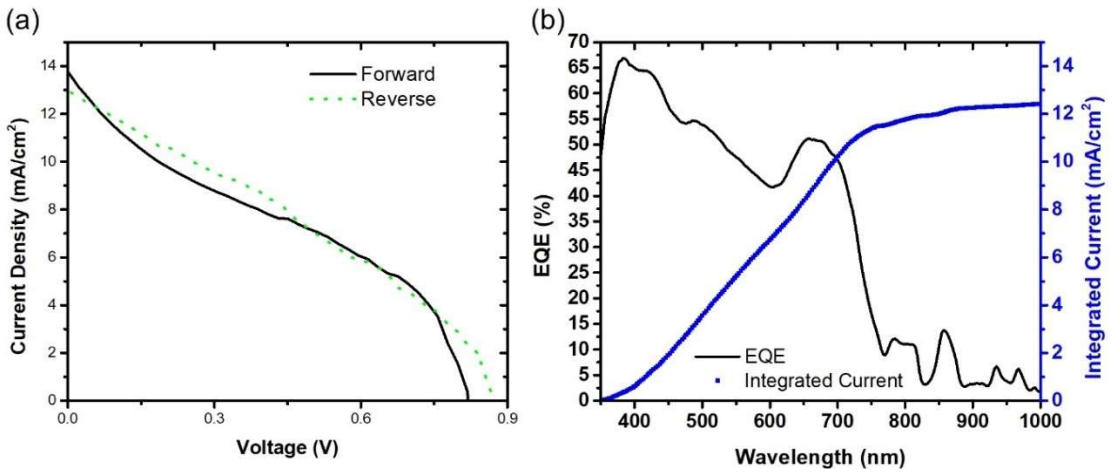

Figure 6-9 The recovered PbI_2 solar cell performance of (a) J-V curve and (b) EQE and the integrated current. The forward scan starts from i_{sc} to V_{oc} and the reversed scan starts from V_{oc} to i_{sc}.

Table 6-3 Key parameters of recovered PbI_2 solar cell for both forward and reversed scans.

	V_{oc} (V)	J_{sc} (mA/cm^2)	V_{max} (V)	J_{max} (mA/cm^2)	Fill Factor (%)	PCE (%)
Forward	0.826	13.8	0.555	6.56	31.9	3.86
Reverse	0.888	13.0	0.635	5.76	31.8	3.88

After the PSCs are assembled, the J-V curve is analyzed for both forward and reversed scans and the results are shown in Figure 6-9(a). The key parameters are summarized in Table 6-3. The i_{sc} of recovered cell is around 13 mA/cm^2 and V_{oc} is close to 0.85 V, which are comparable with published results in similar structure[150]. The overall low efficiency can be explained by the low FF. Because FF is always significantly affected by crystallization of perovskite, as well as the ETM and HTM interface, the reformed lead material recrystallization may play an important role, which requires further investigation and optimization. The EQE of recovered PSC shows a high absorption in visible light region and the integrated current is about 12.4 mA/cm^2. The spectral mismatch factor is calculated to be 0.96 and considered negligible in this study. It is interesting to

notice the small quantum efficiency in IR region for EQE tests, which may result from the impurity in the recovered PbI_2.

6.4. Conclusions

In this chapter, lead contaminants from simulated wastewater are successfully removed through sulfur-treated nanocarbon materials in a CDI system, and the collected lead waste is successfully recovered to perovskite precursors for solar cell study. The sulfur-treated materials can be easily prepared in one-pot hydrothermal reaction with different GO dosage to improve CDI performance. GO shows stronger sulfur modification capability, which is preferred in selective CDI tests. The amount of GO dosage to AC is determined at 25 wt.% as the best performing composite, which benefits from both a high sulfur modification ratio and good electrode coating quality. However, the lead ion behavior in CDI charge and discharge processes can be further studied to improve ion selectivity. In addition, the recovery route of lead ions in CDI effluents is designed to avoid oxidation and reduce mass loss. A yield of 82% is achieved. Recovered perovskite precursor is successfully fabricated into PSCs, and the resulting cells show comparable performance with published results. This research demonstrates a complete lead collection and recovery route to reduce lead risk in the environment and increases commercial value for water treatment systems.

Chapter 7. Summary and Future Work

7.1. Summary of dissertation

Overall the focus of this study is to understand 2D nanomaterials properties and explore their applications for sustainable solar cell fabrication.

First of all, to harness 2D nanomaterial properties, MoS_2/graphene hybrids were created to solve the issue of high cost counter electrode in DSSCs. The hybrids were synthesized through hydrothermal methods and the phase transition and defect formation with varying temperatures were discussed. This study highlighted the understanding of crystallization conditions under different temperatures for the hybrids. Based on the understanding, applications of the hybrids for HER and DSSCs were explored. This work focused on fundamental physical and chemical properties of MoS_2 and graphene, and provided the foundation for the DSSC redox catalyst design.

The second task focused on the design of semi-transparent PSCs. By studying the PSC transparency, crystallization and stability of PSCs, the recipe of semi-transparent PSCs was finalized and the resulting solar cells were successfully used for a smart window application. This work focused on the fundamental understanding of PSC structures and perovskite crystal properties. Through troubleshooting processes, the issues of current PSCs were summarized, and HTM was identified as the main challenge.

The third task employs 2D nanomaterials to address challenges of current PSC design. An improved HTM based on crumpled 2D nanomaterial hybrid was studied. Through a crumpling process at 650 °C with GO nanosheets and CuSCN, a stable CuS/GO nanohybrid was successfully

prepared and tested in PSCs, which demonstrated promising performance. The coating methods were also discussed in this study and improvements were recommended for future research. This study addressed the high-cost and low-stability issues of the HTM for current PSCs and proposed an effective alternative.

The forth task aimed at low-cost and high-volume waste acid treatment methods for lead reform. By applying 2D nanomaterial and other nanostructures in filtration and adsorption systems, the ion removal performances were discussed. The study challenged the historical issue of high concentration sulfuric acid recovery, and discovered the strong disability of created functional groups in the strong acidic condition. This study also explored the possibility of applying the CDI technology to enhance the adsorption kinetics. The preliminary results of produced lead precursors from recycled lead wastes demonstrate the feasibility of sustainably manufacturing perovskite solar cells. This work focused on the sustainable solar cell material recovery and studied multiple waste fluid treatment methods.

The fifth task targeted the lead-contaminated water to expand lead recovery sources. By using nanocarbon materials, a lead-selective CDI device was designed. The CDI system demonstrated a high lead removal efficiency and the discharged lead was successfully recovered to perovskite precursors through simple chemical processes. This work not only offers low-cost and environmentally friendly lead sources for solar cell fabrication, but also addresses a general public concern and increases the value of water treatment system.

In summary, this dissertation work surrounds cost, performance and sustainability as the core of solar cell research, and discusses multiple applications of 2D nanomaterials. Through exploration of solar cell material designs, lead-acid battery recycling methods and water treatment technologies, this work can contribute to the environmentally friendly solar cell design for future energy and environmental applications.

7.2. Future research work

Throughout this study, main properties of 2D nanomaterials are studied for solar cell applications, including semiconducting properties, high surface area, high Young's modules and good flexibility to create nanohybrids and composites. Some limitations are also highlighted. Firstly, the applications of 2D nanomaterial in PSC is still limited, due to the high crystallization quality requirement of perovskite crystals and the narrow allowance of band structure variations. Secondly, the optimization of CDI technology can further improve the recovery of lead materials for sustainable PSC fabrication. Therefore, future studies are suggested in two directions.

First, 2D nanomaterials can be tuned to better adapt to the valence band of perovskite crystals and to better coat the cell surface. Current HTM designs are still limited by their hysteresis effects, which is also present in the HTM designed in this study. The band tuning flexibility of 2D nanomaterials presents an opportunity to address this issue with surface modifications. Further simulation studies can also help address this issue.

Secondly, CDI performance can be evaluated for more fluid matrices. Currently designed CDI system in simulated water has shown high performance with lead concentration in effluent

reaching hundreds of ppm, which is close to the precipitation limit of lead ions in neutral pH water. However, lead removal in acidic or basic water is yet to be realized. In addition, many kinetic behaviors of ions in CDI systems are yet to be explained. With a suitable surface modification of 2D nanomaterials, CDI systems can collect lead from additional sources and decrease negative environmental impact. The understanding of CDI theory can also benefit the design of other electrical-double layer devices, such as capacitors and batteries.

References

1 Chu, S. & Majumdar, A. Opportunities and challenges for a sustainable energy future. *Nature* **488**, 294-303, doi:10.1038/nature11475 (2012).

2 Green, M. A. Third generation photovoltaics: Ultra-high conversion efficiency at low cost. *Prog Photovoltaics* **9**, 123-135, doi:DOI 10.1002/pip.360 (2001).

3 Goetzberger, A., Hebling, C. & Schock, H. W. Photovoltaic materials, history, status and outlook. *Mat Sci Eng R* **40**, 1-46, doi:10.1016/S0927-796x(02)00092-X (2003).

4 Jayawardena, K. D. *et al.* 'Inorganics-in-organics': recent developments and outlook for 4G polymer solar cells. *Nanoscale* **5**, 8411-8427, doi:10.1039/c3nr02733c (2013).

5 Ahmad, S., Guillen, E., Kavan, L., Gratzel, M. & Nazeeruddin, M. K. Metal free sensitizer and catalyst for dye sensitized solar cells. *Energ Environ Sci* **6**, 3439-3466, doi:10.1039/c3ee41888j (2013).

6 Burschka, J. *et al.* Sequential deposition as a route to high-performance perovskite-sensitized solar cells. *Nature* **499**, 316-319, doi:10.1038/nature12340 (2013).

7 Kojima, A., Teshima, K., Shirai, Y. & Miyasaka, T. Organometal halide perovskites as visible-light sensitizers for photovoltaic cells. *J Am Chem Soc* **131**, 6050-6051, doi:10.1021/ja809598r (2009).

8 Etgar, L. *et al.* Mesoscopic CH3NH3PbI3/TiO2 heterojunction solar cells. *J Am Chem Soc* **134**, 17396-17399, doi:10.1021/ja307789s (2012).

9 Kay, A. & Gratzel, M. Low cost photovoltaic modules based on dye sensitized nanocrystalline titanium dioxide and carbon powder. *Sol Energ Mat Sol C* **44**, 99-117, doi:Doi 10.1016/0927-0248(96)00063-3 (1996).

10 Gratzel, M. Recent advances in sensitized mesoscopic solar cells. *Acc Chem Res* **42**, 1788-1798, doi:10.1021/ar900141y (2009).

11 Nazeeruddin, M. K., Baranoff, E. & Gratzel, M. Dye-sensitized solar cells: A brief overview. *Sol Energy* **85**, 1172-1178, doi:10.1016/j.solener.2011.01.018 (2011).

12 Wang, M. *et al.* CoS supersedes Pt as efficient electrocatalyst for triiodide reduction in dye-sensitized solar cells. *J Am Chem Soc* **131**, 15976-15977, doi:10.1021/ja905970y (2009).

13 Wang, M. *et al.* An organic redox electrolyte to rival triiodide/iodide in dye-sensitized solar cells. *Nature chemistry* **2**, 385-389, doi:10.1038/nchem.610 (2010).

14 Chung, I., Lee, B., He, J., Chang, R. P. & Kanatzidis, M. G. All-solid-state dye-sensitized solar cells with high efficiency. *Nature* **485**, 486-489, doi:10.1038/nature11067 (2012).

15 Zhou, H. *et al.* Photovoltaics. Interface engineering of highly efficient perovskite solar cells. *Science* **345**, 542-546, doi:10.1126/science.1254050 (2014).

16 Jeon, N. J. *et al.* Compositional engineering of perovskite materials for high-performance solar cells. *Nature* **517**, 476-480, doi:10.1038/nature14133 (2015).

17 Arora, N. *et al.* Perovskite solar cells with CuSCN hole extraction layers yield stabilized efficiencies greater than 20. *Science* **358**, 768-771, doi:10.1126/science.aam5655 (2017).

18 Beard, M. C., Luther, J. M. & Nozik, A. J. The promise and challenge of nanostructured solar cells. *Nature Nanotechnology* **9**, 951-954, doi:10.1038/nnano.2014.292 (2014).

19 Service, R. F. Energy technology. Perovskite solar cells keep on surging. *Science* **344**, 458, doi:10.1126/science.344.6183.458 (2014).

20 Jung, H. S. & Park, N. G. Perovskite solar cells: from materials to devices. *Small* **11**, 10-25, doi:10.1002/smll.201402767 (2015).

21 Xing, G. *et al.* Long-Range Balanced Electron- and Hole-Transport Lengths in Organic-Inorganic CH3NH3PbI3. *Science* **342**, 344-347, doi:10.1126/science.1243167 (2013).
22 Stranks, S. D. *et al.* Electron-Hole Diffusion Lengths Exceeding 1 Micrometer in an Organometal Trihalide Perovskite Absorber. *Science* **342**, 341-344, doi:10.1126/science.1243982 (2013).
23 Stranks, S. D. & Snaith, H. J. Metal-halide perovskites for photovoltaic and light-emitting devices. *Nat Nanotechnol* **10**, 391-402, doi:10.1038/nnano.2015.90 (2015).
24 Liu, M., Johnston, M. B. & Snaith, H. J. Efficient planar heterojunction perovskite solar cells by vapour deposition. *Nature* **501**, 395-398, doi:10.1038/nature12509 (2013).
25 Zhou, Y. Y. *et al.* Room-temperature crystallization of hybrid-perovskite thin films via solvent-solvent extraction for high-performance solar cells. *J Mater Chem A* **3**, 8178-8184, doi:10.1039/c5ta00477b (2015).
26 Saidaminov, M. I. *et al.* High-quality bulk hybrid perovskite single crystals within minutes by inverse temperature crystallization. *Nat Commun* **6**, 7586, doi:10.1038/ncomms8586 (2015).
27 Ball, J. M., Lee, M. M., Hey, A. & Snaith, H. J. Low-temperature processed meso-superstructured to thin-film perovskite solar cells. *Energ Environ Sci* **6**, 1739-1743, doi:10.1039/c3ee40810h (2013).
28 Leijtens, T. *et al.* Stability of Metal Halide Perovskite Solar Cells. *Adv Energy Mater* **5**, doi:10.1002/aenm.201500963 (2015).
29 Mitzi, D. B., Feild, C. A., Harrison, W. T. A. & Guloy, A. M. Conducting tin halides with a layered organic-based perovskite structure. *Nature* **369**, 467-469 (1994).
30 Mitzi, D. B., Wang, S., Feild, C. A., Chess, C. A. & Guloy, A. M. Conducting Layered Organic-inorganic Halides Containing <110>-Oriented Perovskite Sheets. *Science* **267**, 1473-1476, doi:10.1126/science.267.5203.1473 (1995).
31 Hao, F., Stoumpos, C. C., Chang, R. P. & Kanatzidis, M. G. Anomalous band gap behavior in mixed Sn and Pb perovskites enables broadening of absorption spectrum in solar cells. *J Am Chem Soc* **136**, 8094-8099, doi:10.1021/ja5033259 (2014).
32 Snaith, H. J. *et al.* Anomalous Hysteresis in Perovskite Solar Cells. *J Phys Chem Lett* **5**, 1511-1515, doi:10.1021/jz500113x (2014).
33 Wu, B. *et al.* Long Minority-Carrier Diffusion Length and Low Surface-Recombination Velocity in Inorganic Lead-Free CsSnI3 Perovskite Crystal for Solar Cells. *Advanced Functional Materials*, 1604818, doi:10.1002/adfm.201604818 (2017).
34 Waleed, A. *et al.* Lead-Free Perovskite Nanowire Array Photodetectors with Drastically Improved Stability in Nanoengineering Templates. *Nano Lett*, doi:10.1021/acs.nanolett.6b04587 (2016).
35 Saidaminov, M. I. *et al.* Pure Cs4PbBr6: Highly Luminescent Zero-Dimensional Perovskite Solids. *ACS Energy Letters*, 840-845, doi:10.1021/acsenergylett.6b00396 (2016).
36 Tan, Z. *et al.* Two-Dimensional (C4H9NH3)2PbBr4 Perovskite Crystals for High-Performance Photodetector. *J Am Chem Soc*, doi:10.1021/jacs.6b11683 (2016).
37 Calio, L., Kazim, S., Gratzel, M. & Ahmad, S. Hole-Transport Materials for Perovskite Solar Cells. *Angew Chem Int Ed Engl*, doi:10.1002/anie.201601757 (2016).
38 Jeon, N. J. *et al.* o-Methoxy substituents in spiro-OMeTAD for efficient inorganic-organic hybrid perovskite solar cells. *J Am Chem Soc* **136**, 7837-7840, doi:10.1021/ja502824c (2014).

39 Luo, Q. *et al.* All-Carbon-Electrode-Based Endurable Flexible Perovskite Solar Cells. *Advanced Functional Materials* **28**, doi:10.1002/adfm.201706777 (2018).

40 Fitzer, E., Kochling, K. H., Boehm, H. P. & Marsh, H. in *Pure and Applied Chemistry* Vol. 67 473 (1995).

41 Geim, A. K. & Novoselov, K. S. The rise of graphene. *Nat Mater* **6**, 183-191, doi:10.1038/nmat1849 (2007).

42 Novoselov, K. S. *et al.* Electric field effect in atomically thin carbon films. *Science* **306**, 666-669, doi:10.1126/science.1102896 (2004).

43 Nair, R. R. *et al.* Fine structure constant defines visual transparency of graphene. *Science* **320**, 1308, doi:10.1126/science.1156965 (2008).

44 Novoselov, K. S. *et al.* Two-dimensional atomic crystals. *Proc Natl Acad Sci U S A* **102**, 10451-10453, doi:10.1073/pnas.0502848102 (2005).

45 Zhu, J. H. *et al.* An overview of the engineered graphene nanostructures and nanocomposites. *Rsc Adv* **3**, 22790-22824, doi:10.1039/c3ra44621b (2013).

46 Allen, M. J., Tung, V. C. & Kaner, R. B. Honeycomb carbon: a review of graphene. *Chem Rev* **110**, 132-145, doi:10.1021/cr900070d (2010).

47 Guldi, D. M. & Sgobba, V. Carbon nanostructures for solar energy conversion schemes. *Chem Commun (Camb)* **47**, 606-610, doi:10.1039/c0cc02411b (2011).

48 Mas-Balleste, R., Gomez-Navarro, C., Gomez-Herrero, J. & Zamora, F. 2D materials: to graphene and beyond. *Nanoscale* **3**, 20-30, doi:10.1039/c0nr00323a (2011).

49 Kavan, L., Yum, J. H. & Graetzel, M. Application of graphene-based nanostructures in dye-sensitized solar cells. *Phys Status Solidi B* **250**, 2643-2648, doi:10.1002/pssb.201300064 (2013).

50 Forbeaux, I., Themlin, J. M. & Debever, J. M. Heteroepitaxial graphite on 6H-SiC(0001): Interface formation through conduction-band electronic structure. *Phys Rev B* **58**, 16396-16406, doi:DOI 10.1103/PhysRevB.58.16396 (1998).

51 Hernandez, Y. *et al.* High-yield production of graphene by liquid-phase exfoliation of graphite. *Nat Nanotechnol* **3**, 563-568, doi:10.1038/nnano.2008.215 (2008).

52 Lotya, M. *et al.* Liquid phase production of graphene by exfoliation of graphite in surfactant/water solutions. *J Am Chem Soc* **131**, 3611-3620, doi:10.1021/ja807449u (2009).

53 Kumar, S. *et al.* Gas phase controlled deposition of high quality large-area graphene films. *Chem Commun (Camb)* **46**, 1422-1424, doi:10.1039/b919725g (2010).

54 Kim, K. S. *et al.* Large-scale pattern growth of graphene films for stretchable transparent electrodes. *Nature* **457**, 706-710, doi:10.1038/nature07719 (2009).

55 Li, X. *et al.* Large-area synthesis of high-quality and uniform graphene films on copper foils. *Science* **324**, 1312-1314, doi:10.1126/science.1171245 (2009).

56 Bae, S. *et al.* Roll-to-roll production of 30-inch graphene films for transparent electrodes. *Nat Nanotechnol* **5**, 574-578, doi:10.1038/nnano.2010.132 (2010).

57 Hummers, W. S. & Offeman, R. E. Preparation of Graphitic Oxide. *Journal of the American Chemical Society* **80**, 1339-1339, doi:10.1021/ja01539a017 (1958).

58 Dreyer, D. R., Park, S., Bielawski, C. W. & Ruoff, R. S. The chemistry of graphene oxide. *Chemical Society reviews* **39**, 228-240, doi:10.1039/b917103g (2010).

59 Zhu, Y. *et al.* Graphene and graphene oxide: synthesis, properties, and applications. *Adv Mater* **22**, 3906-3924, doi:10.1002/adma.201001068 (2010).

60 Stankovich, S. *et al.* Synthesis of graphene-based nanosheets via chemical reduction of exfoliated graphite oxide. *Carbon* **45**, 1558-1565, doi:10.1016/j.carbon.2007.02.034 (2007).
61 Lee, S. H. *et al.* Three-dimensional self-assembly of graphene oxide platelets into mechanically flexible macroporous carbon films. *Angew Chem Int Ed Engl* **49**, 10084-10088, doi:10.1002/anie.201006240 (2010).
62 Bo, Z. *et al.* Green preparation of reduced graphene oxide for sensing and energy storage applications. *Sci Rep* **4**, 4684, doi:10.1038/srep04684 (2014).
63 Li, D., Muller, M. B., Gilje, S., Kaner, R. B. & Wallace, G. G. Processable aqueous dispersions of graphene nanosheets. *Nat Nanotechnol* **3**, 101-105, doi:10.1038/nnano.2007.451 (2008).
64 Mattevi, C., Kim, H. & Chhowalla, M. A review of chemical vapour deposition of graphene on copper. *J Mater Chem* **21**, 3324-3334, doi:10.1039/c0jm02126a (2011).
65 Roy-Mayhew, J. D. *Functionalized graphene sheets in dye-sensitized solar cell counter electrodes* Copyright (C) 2014 American Chemical Society (ACS). All Rights Reserved. thesis, (2013).
66 Hong, W. J., Xu, Y. X., Lu, G. W., Li, C. & Shi, G. Q. Transparent graphene/PEDOT-PSS composite films as counter electrodes of dye-sensitized solar cells. *Electrochem Commun* **10**, 1555-1558, doi:10.1016/j.elecom.2008.08.007 (2008).
67 Zhang, D. W. *et al.* Graphene-based counter electrode for dye-sensitized solar cells. *Carbon* **49**, 5382-5388, doi:10.1016/j.carbon.2011.08.005 (2011).
68 Jeon, Y. S. & Shin, H. S. Working electrode for dye sensitized solar cell, dye sensitized solar cell with the working electrode, and its manufacturing method. KR2013033083A (2013).
69 Prakash, S. K., Singh, H., Panjiar, H., Manhas, S. & Daniel, B. S. S. Application of Graphene Oxide and TiO2 in the Fabrication of Dye Sensitized Solar Cells Module by Electrode Modification. *Advanced Materials Research* **585**, 255-259, doi:10.4028/www.scientific.net/AMR.585.255 (2012).
70 Morales-Torres, S., Pastrana-Martinez, L. M., Figueiredo, J. L., Faria, J. L. & Silva, A. M. Design of graphene-based TiO2 photocatalysts--a review. *Environ Sci Pollut Res Int* **19**, 3676-3687, doi:10.1007/s11356-012-0939-4 (2012).
71 Song, M., Ameen, S., Akhtar, M. S., Seo, H. K. & Shin, H. S. HFCVD grown graphene like carbon-nickel nanocomposite thin film as effective counter electrode for dye sensitized solar cells. *Mater Res Bull* **48**, 4538-4543, doi:10.1016/j.materresbull.2013.07.045 (2013).
72 Yang, C. Y. *et al.* Direct PECVD growth of vertically erected graphene walls on dielectric substrates as excellent multifunctional electrodes. *J Mater Chem A* **1**, 770-775, doi:10.1039/c2ta00234e (2013).
73 Wang, X., Zhi, L. & Mullen, K. Transparent, conductive graphene electrodes for dye-sensitized solar cells. *Nano Lett* **8**, 323-327, doi:10.1021/nl072838r (2008).
74 Chen, J. H., Jang, C., Xiao, S., Ishigami, M. & Fuhrer, M. S. Intrinsic and extrinsic performance limits of graphene devices on SiO2. *Nat Nanotechnol* **3**, 206-209, doi:10.1038/nnano.2008.58 (2008).
75 Bolotin, K. I. *et al.* Ultrahigh electron mobility in suspended graphene. *Solid State Commun* **146**, 351-355, doi:10.1016/j.ssc.2008.02.024 (2008).

76 Wu, Z. *et al.* Transparent, conductive carbon nanotube films. *Science* **305**, 1273-1276, doi:10.1126/science.1101243 (2004).
77 Rasool, H. I., Ophus, C., Klug, W. S., Zettl, A. & Gimzewski, J. K. Measurement of the intrinsic strength of crystalline and polycrystalline graphene. *Nature Communications* **4**, doi:10.1038/ncomms3811 (2013).
78 Girit, C. O. *et al.* Graphene at the edge: stability and dynamics. *Science* **323**, 1705-1708, doi:10.1126/science.1166999 (2009).
79 Lee, G. H. *et al.* High-strength chemical-vapor-deposited graphene and grain boundaries. *Science* **340**, 1073-1076, doi:10.1126/science.1235126 (2013).
80 Upadhyaya, H. M., Senthilarasu, S., Hsu, M. H. & Kumar, D. K. Recent progress and the status of dye-sensitised solar cell (DSSC) technology with state-of-the-art conversion efficiencies. *Sol Energ Mat Sol C* **119**, 291-295, doi:10.1016/j.solmat.2013.08.031 (2013).
81 Kalyanasundaram, K. *Dye-sensitized solar cells*. (EPFL press, 2010).
82 Hudaya, C., Park, J. H. & Lee, J. K. Effects of process parameters on sheet resistance uniformity of fluorine-doped tin oxide thin films. *Nanoscale Res Lett* **7**, 17, doi:10.1186/1556-276X-7-17 (2012).
83 Zhang, M. *et al.* Strong, transparent, multifunctional, carbon nanotube sheets. *Science* **309**, 1215-1219, doi:10.1126/science.1115311 (2005).
84 Gratzel, M. Photoelectrochemical cells. *Nature* **414**, 338-344, doi:10.1038/35104607 (2001).
85 Song, M., Seo, H. K., Ameen, S., Akhtar, M. S. & Shin, H. S. Low Resistance Transparent Graphene-Like Carbon Thin Film Substrates for High Performance Dye Sensitized Solar Cells. *Electrochim Acta* **115**, 559-565, doi:DOI 10.1016/j.electacta.2013.10.216 (2014).
86 Batmunkh, M., Shearer, C. J., Biggs, M. J. & Shapter, J. G. Solution processed graphene structures for perovskite solar cells. *J Mater Chem A* **4**, 2605-2616, doi:10.1039/c5ta08996d (2016).
87 Yoon, J. *et al.* Superflexible, high-efficiency perovskite solar cells utilizing graphene electrodes: towards future foldable power sources. *Energ Environ Sci* **10**, 337-345, doi:10.1039/c6ee02650h (2017).
88 Yang, N., Zhai, J., Wang, D., Chen, Y. & Jiang, L. Two-dimensional graphene bridges enhanced photoinduced charge transport in dye-sensitized solar cells. *ACS Nano* **4**, 887-894, doi:10.1021/nn901660v (2010).
89 Kongkanand, A., Dominguez, R. M. & Kamat, P. V. Single wall carbon nanotube scaffolds for photoelectrochemical solar cells. Capture and transport of photogenerated electrons. *Nano Lett* **7**, 676-680, doi:10.1021/nl0627238 (2007).
90 Bell, N. J. *et al.* Understanding the Enhancement in Photoelectrochemical Properties of Photocatalytically Prepared TiO2-Reduced Graphene Oxide Composite. *J Phys Chem C* **115**, 6004-6009, doi:10.1021/jp1113575 (2011).
91 Wang, H., Leonard, S. L. & Hu, Y. H. Promoting Effect of Graphene on Dye-Sensitized Solar Cells. *Industrial & Engineering Chemistry Research* **51**, 10613-10620, doi:10.1021/ie300563h (2012).
92 He, Z., Phan, H., Liu, J., Nguyen, T.-Q. & Tan, T. T. Y. Understanding TiO2 Size-Dependent Electron Transport Properties of a Graphene-TiO2 Photoanode in Dye-

Sensitized Solar Cells Using Conducting Atomic Force Microscopy. *Adv. Mater. (Weinheim, Ger.)* **25**, 6900-6904, doi:10.1002/adma.201303327 (2013).
93 Zhang, H. Y. *et al.* Effects of TiO2 film thickness on photovoltaic properties of dye-sensitized solar cell and its enhanced performance by graphene combination. *Mater Res Bull* **49**, 126-131, doi:10.1016/j.materresbull.2013.08.058 (2014).
94 Petridis, C., Kakavelakis, G. & Kymakis, E. Renaissance of graphene-related materials in photovoltaics due to the emergence of metal halide perovskite solar cells. *Energ Environ Sci*, doi:10.1039/c7ee03620e (2018).
95 Bi, E. *et al.* Diffusion engineering of ions and charge carriers for stable efficient perovskite solar cells. *Nat Commun* **8**, 15330, doi:10.1038/ncomms15330 (2017).
96 Yan, X., Cui, X., Li, B. & Li, L. S. Large, solution-processable graphene quantum dots as light absorbers for photovoltaics. *Nano Lett* **10**, 1869-1873, doi:10.1021/nl101060h (2010).
97 Lee, E., Ryu, J. & Jang, J. Fabrication of graphene quantum dots via size-selective precipitation and their application in upconversion-based DSSCs. *Chem Commun (Camb)* **49**, 9995-9997, doi:10.1039/c3cc45588b (2013).
98 Hadadian, M. *et al.* Enhancing Efficiency of Perovskite Solar Cells via N-doped Graphene: Crystal Modification and Surface Passivation. *Adv Mater* **28**, 8681-8686, doi:10.1002/adma.201602785 (2016).
99 Fang, X. *et al.* Graphene quantum dot incorporated perovskite films: passivating grain boundaries and facilitating electron extraction. *Phys Chem Chem Phys* **19**, 6057-6063, doi:10.1039/c6cp06953c (2017).
100 Kaniyoor, A. & Ramaprabhu, S. Thermally exfoliated graphene based counter electrode for low cost dye sensitized solar cells. *J. Appl. Phys.* **109**, 124308/124301-124308/124306, doi:10.1063/1.3600231 (2011).
101 Roy-Mayhew, J. D., Bozym, D. J., Punckt, C. & Aksay, I. A. Functionalized graphene as a catalytic counter electrode in dye-sensitized solar cells. *ACS Nano* **4**, 6203-6211, doi:10.1021/nn1016428 (2010).
102 Peng, Y., Zhong, J., Wang, K., Xue, B. & Cheng, Y.-B. A printable graphene enhanced composite counter electrode for flexible dye-sensitized solar cells. *Nano Energy* **2**, 235-240, doi:10.1016/j.nanoen.2012.08.010 (2013).
103 Stankovich, S. *et al.* Graphene-based composite materials. *Nature* **442**, 282-286, doi:http://www.nature.com/nature/journal/v442/n7100/suppinfo/nature04969_S1.html (2006).
104 Bajpai, R. *et al.* Graphene supported nickel nanoparticle as a viable replacement for platinum in dye sensitized solar cells. *Nanoscale* **4**, 926-930, doi:10.1039/c2nr11127f (2012).
105 Kaniyoor, A. & Ramaprabhu, S. An optically transparent cathode for dye sensitized solar cells based on cationically functionalized and metal decorated graphene. *Nano Energy* **1**, 757-763, doi:10.1016/j.nanoen.2012.06.004 (2012).
106 Wang, Y., Liu, J., Liu, L. & Sun, D. D. High-quality reduced graphene oxide-nanocrystalline platinum hybrid materials prepared by simultaneous co-reduction of graphene oxide and chloroplatinic acid. *Nanoscale Res. Lett.* **6**, 241, 248 pp., doi:10.1186/1556-276X-6-241 (2011).

107 Tjoa, V. *et al.* Facile Photochemical Synthesis of Graphene-Pt Nanoparticle Composite for Counter Electrode in Dye Sensitized Solar Cell. *ACS Appl. Mater. Interfaces* **4**, 3447-3452, doi:10.1021/am300437g (2012).
108 Yue, G., Lin, J.-Y., Tai, S.-Y., Xiao, Y. & Wu, J. A catalytic composite film of MoS2/graphene flake as a counter electrode for Pt-free dye-sensitized solar cells. *Electrochim. Acta* **85**, 162-168, doi:10.1016/j.electacta.2012.08.040 (2012).
109 Ju, M. J. *et al.* N-Doped Graphene Nanoplatelets as Superior Metal-Free Counter Electrodes for Organic Dye-Sensitized Solar Cells. *ACS Nano* **7**, 5243-5250, doi:10.1021/nn4009774 (2013).
110 Zhu, G., Pan, L. K., Lu, T., Xu, T. & Sun, Z. Electrophoretic deposition of reduced graphene-carbon nanotubes composite films as counter electrodes of dye-sensitized solar cells. *J Mater Chem* **21**, 14869-14875, doi:10.1039/c1jm12433a (2011).
111 Roy-Mayhew, J. D. & Aksay, I. A. Graphene materials and their use in dye-sensitized solar cells. *Chem Rev* **114**, 6323-6348, doi:10.1021/cr400412a (2014).
112 Wang, F. *et al.* Highly stable perovskite solar cells with an all-carbon hole transport layer. *Nanoscale* **8**, 11882-11888, doi:10.1039/c6nr01152g (2016).
113 Li, J. *et al.* Graphdiyne: A Metal-Free Material as Hole Transfer Layer To Fabricate Quantum Dot-Sensitized Photocathodes for Hydrogen Production. *J Am Chem Soc*, doi:10.1021/jacs.5b12758 (2016).
114 Jin, Z. *et al.* Graphdiyne: An Efficient Hole Transporter for Stable High-Performance Colloidal Quantum Dot Solar Cells. *Advanced Functional Materials*, doi:10.1002/adfm.201601570 (2016).
115 Xu, M., Liang, T., Shi, M. & Chen, H. Graphene-like two-dimensional materials. *Chem Rev* **113**, 3766-3798, doi:10.1021/cr300263a (2013).
116 Deng, D. *et al.* Catalysis with two-dimensional materials and their heterostructures. *Nat Nanotechnol* **11**, 218-230, doi:10.1038/nnano.2015.340 (2016).
117 Batmunkh, M., Bat-Erdene, M. & Shapter, J. G. Phosphorene and Phosphorene-Based Materials - Prospects for Future Applications. *Advanced Materials*, doi:10.1002/adma.201602254 (2016).
118 Lange, S., Schmidt, P. & Nilges, T. Au3SnP7@black phosphorus: an easy access to black phosphorus. *Inorg Chem* **46**, 4028-4035, doi:10.1021/ic062192q (2007).
119 Pfitzner, A., Brau, M. F., Zweck, J., Brunklaus, G. & Eckert, H. Phosphorus nanorods--two allotropic modifications of a long-known element. *Angew Chem Int Ed Engl* **43**, 4228-4231, doi:10.1002/anie.200460244 (2004).
120 Sun, J. *et al.* Formation of stable phosphorus-carbon bond for enhanced performance in black phosphorus nanoparticle-graphite composite battery anodes. *Nano Lett* **14**, 4573-4580, doi:10.1021/nl501617j (2014).
121 Cui, S. *et al.* Ultrahigh sensitivity and layer-dependent sensing performance of phosphorene-based gas sensors. *Nature Communications* **6**, 8632, doi:10.1038/ncomms9632 (2015).
122 Xiang, Q., Yu, J. & Jaroniec, M. Synergetic effect of MoS2 and graphene as cocatalysts for enhanced photocatalytic H2 production activity of TiO2 nanoparticles. *J Am Chem Soc* **134**, 6575-6578, doi:10.1021/ja302846n (2012).
123 Lukowski, M. A. *et al.* Enhanced hydrogen evolution catalysis from chemically exfoliated metallic MoS2 nanosheets. *J Am Chem Soc* **135**, 10274-10277, doi:10.1021/ja404523s (2013).

124 Zheng, M. *et al.* Flowerlike molybdenum sulfide/multi-walled carbon nanotube hybrid as Pt-free counter electrode used in dye-sensitized solar cells. *Electrochim Acta* **173**, 252-259, doi:10.1016/j.electacta.2015.05.069 (2015).
125 Al-Mamun, M. *et al.* Directly hydrothermal growth of ultrathin MoS2 nanostructured films as high performance counter electrodes for dye-sensitised solar cells. *RSC Adv.* **4**, 21277-21283, doi:10.1039/c4ra00583j (2014).
126 Du, T. *et al.* TiO2-based solar cells sensitized by chemical-bath-deposited few-layer MoS2. *J. Power Sources* **275**, 943-949, doi:10.1016/j.jpowsour.2014.11.048 (2015).
127 Le, Q. V., Nguyen, T. P., Jang, H. W. & Kim, S. Y. The use of UV/ozone-treated MoS2 nanosheets for extended air stability in organic photovoltaic cells. *Phys. Chem. Chem. Phys.* **16**, 13123-13128, doi:10.1039/c4cp01598c (2014).
128 Evans, B. L. & Thompson, K. T. Photovoltage in thin crystals of molybdenum disulfide. *Brit. J. Appl. Phys.* **[2] 1**, 1619-1623 (1968).
129 Chhowalla, M. *et al.* The chemistry of two-dimensional layered transition metal dichalcogenide nanosheets. *Nature chemistry* **5**, 263-275, doi:10.1038/nchem.1589 (2013).
130 Liu, Z., Lau, S. P. & Yan, F. Functionalized graphene and other two-dimensional materials for photovoltaic devices: device design and processing. *Chemical Society reviews*, doi:10.1039/c4cs00455h (2015).
131 Kuc, A., Zibouche, N. & Heine, T. Influence of quantum confinement on the electronic structure of the transition metal sulfideTS2. *Phys Rev B* **83**, doi:10.1103/PhysRevB.83.245213 (2011).
132 Yun, W. S., Han, S. W., Hong, S. C., Kim, I. G. & Lee, J. D. Thickness and strain effects on electronic structures of transition metal dichalcogenides: 2H-MX2semiconductors (M=Mo, W;X=S, Se, Te). *Phys Rev B* **85**, doi:10.1103/PhysRevB.85.033305 (2012).
133 Yue, G. *et al.* High performance platinum-free counter electrode of molybdenum sulfide-carbon used in dye-sensitized solar cells. *J Mater Chem A* **1**, 1495-1501, doi:10.1039/C2TA00860B (2013).
134 Yue, G., Zhang, W., Wu, J. & Jiang, Q. Glucose aided synthesis of molybdenum sulfide/carbon nanotubes composites as counter electrode for high performance dye-sensitized solar cells. *Electrochim. Acta* **112**, 655-662, doi:10.1016/j.electacta.2013.09.019 (2013).
135 Song, D. *et al.* Facile fabrication of MoS2/PEDOT-PSS composites as low-cost and efficient counter electrodes for dye-sensitized solar cells. *J. Photochem. Photobiol., A* **279**, 47-51, doi:10.1016/j.jphotochem.2014.01.009 (2014).
136 International Lead Association. *Significant growth in lead usage underlines its importance to the global economy*, <https://www.ila-lead.org/news/lead-in-the-news/2012-11-30/significant-growth-in-lead-usage-underlines-its--importance-to-the-global-economy-> (2012).
137 King, M., Moats, M. & Davenport, W. G. I. 1 online resource (464 p (Elsevier Science,, Burlington, 2013).
138 Ryan, P. B., Huet, N. & MacIntosh, D. L. Longitudinal investigation of exposure to arsenic, cadmium, and lead in drinking water. *Environ Health Perspect* **108**, 731-735, doi:sc271_5_1835 [pii] ET - 2000/08/31 (2000).

139 Edwards, M., Triantafyllidou, S. & Best, D. Elevated blood lead in young children due to lead-contaminated drinking water: Washington, DC, 2001-2004. *Environ Sci Technol* **43**, 1618-1623, doi:10.1021/es802789w (2009).
140 US EPA. National Primary Drinking Water Regulations. Report No. 0097-6326 (Print) 0097-6326 (Linking), 141-142 (2013).
141 World Health Organization. Lead in Drinking-water. (2011).
142 US EPA. Final Report - High Lead at Three Residences in Flint, Michigan (2015).
143 Husein, M. M., Vera, J. H. & Weber, M. E. Removal of Lead from Aqueous Solutions with Sodium Caprate. *Separation Science and Technology* **33**, 1889-1904, doi:10.1080/01496399808545911 (1998).
144 Lin, S. W. & Navarro, R. M. F. An innovative method for removing Hg2+ and Pb2+ in ppm concentrations from aqueous media. *Chemosphere* **39**, 1809-1817, doi:10.1016/s0045-6535(99)00074-0 (1999).
145 Fu, F. & Wang, Q. Removal of heavy metal ions from wastewaters: a review. *Journal of environmental management* **92**, 407-418, doi:10.1016/j.jenvman.2010.11.011 (2011).
146 Oren, Y. Capacitive deionization (CDI) for desalination and water treatment — past, present and future (a review). *Desalination* **228**, 10-29, doi:10.1016/j.desal.2007.08.005 (2008).
147 Huang, Z., Lu, L., Cai, Z. & Ren, Z. J. Individual and competitive removal of heavy metals using capacitive deionization. *J Hazard Mater* **302**, 323-331, doi:10.1016/j.jhazmat.2015.09.064 (2016).
148 Seo, S. J. *et al.* Investigation on removal of hardness ions by capacitive deionization (CDI) for water softening applications. *Water Res* **44**, 2267-2275, doi:10.1016/j.watres.2009.10.020 (2010).
149 Porada, S., Zhao, R., van der Wal, A., Presser, V. & Biesheuvel, P. M. Review on the science and technology of water desalination by capacitive deionization. *Prog Mater Sci* **58**, 1388-1442, doi:10.1016/j.pmatsci.2013.03.005 (2013).
150 Chen, P.-Y. *et al.* Environmentally responsible fabrication of efficient perovskite solar cells from recycled car batteries. *Energy Environ. Sci.* **7**, 3659-3665, doi:10.1039/c4ee00965g (2014).
151 Chen, P.-Y. *et al.* Response to the comments on “Environmentally responsible fabrication of efficient perovskite solar cells from recycled car batteries” by Po-Yen Chen, Jifa Qi, Matthew T. Klug, Xiangnan Dang, Paula T. Hammond, and Angela M. Belcher published in Energy Environ. Sci. in 2014. *Energy Environ. Sci.* **8**, 1618-1625, doi:10.1039/c5ee00400d (2015).
152 Mao, S. *et al.* Perpendicularly oriented MoSe2 /graphene nanosheets as advanced electrocatalysts for hydrogen evolution. *Small* **11**, 414-419, doi:10.1002/smll.201401598 (2015).
153 Hou, Y. *et al.* A 3D hybrid of layered MoS2/nitrogen-doped graphene nanosheet aerogels: an effective catalyst for hydrogen evolution in microbial electrolysis cells. *J Mater Chem A* **2**, 13795-13800, doi:10.1039/c4ta02254h (2014).
154 Hou, Y., Wen, Z., Cui, S., Guo, X. & Chen, J. Constructing 2D porous graphitic C3 N4 nanosheets/nitrogen-doped graphene/layered MoS2 ternary nanojunction with enhanced photoelectrochemical activity. *Adv Mater* **25**, 6291-6297, doi:10.1002/adma.201303116 (2013).

155 David, L., Bhandavat, R. & Singh, G. MoS2/graphene composite paper for sodium-ion battery electrodes. *ACS Nano* **8**, 1759-1770, doi:10.1021/nn406156b (2014).
156 Chang, K. & Chen, W. L-cysteine-assisted synthesis of layered MoS(2)/graphene composites with excellent electrochemical performances for lithium ion batteries. *ACS Nano* **5**, 4720-4728, doi:10.1021/nn200659w (2011).
157 Liu, G. B., Shan, W. Y., Yao, Y. G., Yao, W. & Xiao, D. Three-band tight-binding model for monolayers of group-VIB transition metal dichalcogenides. *Phys Rev B* **88**, 085433, doi:10.1103/PhysRevB.88.085433 (2013).
158 Prins, F., Goodman, A. J. & Tisdale, W. A. Reduced Dielectric Screening and Enhanced Energy Transfer in Single- and Few-Layer MoS2. *Nano Lett.* **14**, 6087-6091, doi:10.1021/nl5019386 (2014).
159 Debbichi, L., Eriksson, O. & Lebegue, S. Electronic structure of two-dimensional transition metal dichalcogenide bilayers from ab initio theory. *Phys. Rev. B: Condens. Matter Mater. Phys.* **89**, 205311/205311-205311/205315, 205315 pp., doi:10.1103/PhysRevB.89.205311 (2014).
160 Zhou, W. *et al.* Intrinsic Structural Defects in Monolayer Molybdenum Disulfide. *Nano Lett.* **13**, 2615-2622, doi:10.1021/nl4007479 (2013).
161 Li, Y. *et al.* MoS2 nanoparticles grown on graphene: an advanced catalyst for the hydrogen evolution reaction. *J Am Chem Soc* **133**, 7296-7299, doi:10.1021/ja201269b (2011).
162 Wang, H., Yuan, H., Sae Hong, S., Li, Y. & Cui, Y. Physical and chemical tuning of two-dimensional transition metal dichalcogenides. *Chem. Soc. Rev.*, doi:10.1039/c4cs00287c (2014).
163 Patil, S. A. *et al.* Highly efficient and stable DSSCs of wet-chemically synthesized MoS2 counter electrode. *Dalton Trans* **43**, 5256-5259, doi:10.1039/c3dt53356e (2014).
164 Finn, S. T. & Macdonald, J. E. Petaled Molybdenum Disulfide Surfaces: Facile Synthesis of a Superior Cathode for QDSSCs. *Adv Energy Mater* **4**, n/a, doi:10.1002/aenm.201400495 (2014).
165 Xie, J. *et al.* Controllable disorder engineering in oxygen-incorporated MoS2 ultrathin nanosheets for efficient hydrogen evolution. *J Am Chem Soc* **135**, 17881-17888, doi:10.1021/ja408329q (2013).
166 Dikin, D. A. *et al.* Preparation and characterization of graphene oxide paper. *Nature* **448**, 457-460, doi:10.1038/nature06016 (2007).
167 Hu, W. & Yang, J. L. First-principles study of two-dimensional van der Waals heterojunctions. *Comp Mater Sci* **112**, 518-526, doi:10.1016/j.commatsci.2015.06.033 (2016).
168 Zhang, H. P., Lin, H. F., Zheng, Y., Hu, Y. F. & MacLennan, A. Understanding of the effect of synthesis temperature on the crystallization and activity of nano-MoS2 catalyst. *Appl Catal B-Environ* **165**, 537-546, doi:10.1016/j.apcatb.2014.10.046 (2015).
169 Wang, D. Z., Pan, Z., Wu, Z. Z., Wang, Z. P. & Liu, Z. H. Hydrothermal synthesis of MoS2 nanoflowers as highly efficient hydrogen evolution reaction catalysts. *J Power Sources* **264**, 229-234, doi:10.1016/j.jpowsour.2014.04.066 (2014).
170 Marcano, D. C. *et al.* Improved Synthesis of Graphene Oxide. *ACS Nano* **4**, 4806-4814, doi:10.1021/nn1006368 (2010).
171 Zhu, Y. W. *et al.* Microwave assisted exfoliation and reduction of graphite oxide for ultracapacitors. *Carbon* **48**, 2118-2122, doi:10.1016/j.carbon.2010.02.001 (2010).

172 Hou, Y. *et al.* Strongly Coupled 3D Hybrids of N-doped Porous Carbon Nanosheet/CoNi Alloy-Encapsulated Carbon Nanotubes for Enhanced Electrocatalysis. *Small* **11**, 5940-5948, doi:10.1002/smll.201502297 (2015).
173 Hashimoto, A., Suenaga, K., Gloter, A., Urita, K. & Iijima, S. Direct evidence for atomic defects in graphene layers. *Nature* **430**, 870-873, doi:10.1038/nature02817 (2004).
174 Acerce, M., Voiry, D. & Chhowalla, M. Metallic 1T phase MoS2 nanosheets as supercapacitor electrode materials. *Nat Nanotechnol* **10**, 313-318, doi:10.1038/nnano.2015.40 (2015).
175 Chen, J. M. & Wang, C. S. Second order Raman spectrum of MoS2. *Solid State Commun* **14**, 857-860, doi:10.1016/0038-1098(74)90150-1 (1974).
176 Ambrosi, A., Sofer, Z. & Pumera, M. 2H --> 1T phase transition and hydrogen evolution activity of MoS2, MoSe2, WS2 and WSe2 strongly depends on the MX2 composition. *Chem Commun (Camb)* **51**, 8450-8453, doi:10.1039/c5cc00803d (2015).
177 Yan, Y. *et al.* Facile synthesis of low crystalline MoS2 nanosheet-coated CNTs for enhanced hydrogen evolution reaction. *Nanoscale* **5**, 7768-7771, doi:10.1039/c3nr02994h (2013).
178 Hansen, L. P., Johnson, E., Brorson, M. & Helveg, S. Growth Mechanism for Single- and Multi-Layer MoS2Nanocrystals. *The Journal of Physical Chemistry C* **118**, 22768-22773, doi:10.1021/jp5069279 (2014).
179 Ouyang, Y. *et al.* Activating Inert Basal Planes of MoS2for Hydrogen Evolution Reaction through the Formation of Different Intrinsic Defects. *Chemistry of Materials* **28**, 4390-4396, doi:10.1021/acs.chemmater.6b01395 (2016).
180 Akashi, R. *et al.* Two-Dimensional Valley Electrons and Excitons in Noncentrosymmetric $3R\text{-}{\mathrm{MoS}}_{2}$. *Physical Review Applied* **4**, 014002 (2015).
181 Duerloo, K. A. & Reed, E. J. Structural Phase Transitions by Design in Monolayer Alloys. *ACS Nano* **10**, 289-297, doi:10.1021/acsnano.5b04359 (2016).
182 Britnell, L. *et al.* Strong Light-Matter Interactions in Heterostructures of Atomically Thin Films. *Science* **340**, 1311-1314, doi:DOI 10.1126/science.1235547 (2013).
183 Myoung, N., Seo, K., Lee, S. J. & Ihm, G. Large Current Modulation and Spin-Dependent Tunneling of Vertical Graphene/MoS2 Heterostructures. *ACS Nano* **7**, 7021-7027, doi:10.1021/nn402919d (2013).
184 Guo, X., Lu, G. & Chen, J. Graphene-Based Materials for Photoanodes in Dye-Sensitized Solar Cells. *Frontiers in Energy Research* **3**, doi:10.3389/fenrg.2015.00050 (2015).
185 Ito, S. *et al.* Fabrication of thin film dye sensitized solar cells with solar to electric power conversion efficiency over 10%. *Thin Solid Films* **516**, 4613-4619, doi:10.1016/j.tsf.2007.05.090 (2008).
186 Eng, A. Y. S., Ambrosi, A., Sofer, Z., Šimek, P. & Pumera, M. Electrochemistry of Transition Metal Dichalcogenides: Strong Dependence on the Metal-to-Chalcogen Composition and Exfoliation Method. *ACS Nano*, doi:10.1021/nn503832j (2014).
187 Ito, S. *et al.* High-Efficiency Organic-Dye- Sensitized Solar Cells Controlled by Nanocrystalline-TiO2 Electrode Thickness. *Advanced Materials* **18**, 1202-1205, doi:10.1002/adma.200502540 (2006).
188 Jeon, N. J. *et al.* Solvent engineering for high-performance inorganic-organic hybrid perovskite solar cells. *Nat Mater* **13**, 897-903, doi:10.1038/nmat4014 (2014).

189 Gratia, P. *et al.* Intrinsic Halide Segregation at Nanometer Scale Determines the High Efficiency of Mixed Cation/Mixed Halide Perovskite Solar Cells. *J Am Chem Soc* **138**, 15821-15824, doi:10.1021/jacs.6b10049 (2016).
190 Chen, Q. *et al.* Planar Heterojunction Perovskite Solar Cells via Vapor-Assisted Solution Process. *Journal of the American Chemical Society* **136**, 622-625, doi:10.1021/ja411509g (2013).
191 Pastorelli, F. *et al.* Enhanced Light Harvesting in Semitransparent Organic Solar Cells using an Optical Metal Cavity Configuration. *Adv Energy Mater*, n/a-n/a, doi:10.1002/aenm.201400614 (2014).
192 Betancur, R. *et al.* Transparent polymer solar cells employing a layered light-trapping architecture. *Nature Photonics* **7**, 995-1000, doi:10.1038/nphoton.2013.276 (2013).
193 Roldán-Carmona, C. *et al.* High efficiency single-junction semitransparent perovskite solar cells. *Energ Environ Sci* **7**, 2968, doi:10.1039/c4ee01389a (2014).
194 Eperon, G. E., Burlakov, V. M., Docampo, P., Goriely, A. & Snaith, H. J. Morphological Control for High Performance, Solution-Processed Planar Heterojunction Perovskite Solar Cells. *Advanced Functional Materials* **24**, 151-157, doi:10.1002/adfm.201302090 (2014).
195 Christians, J. A., Fung, R. C. & Kamat, P. V. An inorganic hole conductor for organo-lead halide perovskite solar cells. Improved hole conductivity with copper iodide. *J Am Chem Soc* **136**, 758-764, doi:10.1021/ja411014k (2014).
196 Lv, M. *et al.* Colloidal CuInS2 Quantum Dots as Inorganic Hole-Transporting Material in Perovskite Solar Cells. *ACS Appl Mater Interfaces* **7**, 17482-17488, doi:10.1021/acsami.5b05104 (2015).
197 Jung, M. *et al.* Thermal Stability of CuSCN Hole Conductor-Based Perovskite Solar Cells. *ChemSusChem* **9**, 2592-2596, doi:10.1002/cssc.201600957 (2016).
198 Wijeyasinghe, N. & Anthopoulos, T. D. Copper(I) thiocyanate (CuSCN) as a hole-transport material for large-area opto/electronics. *Semiconductor Science and Technology* **30**, doi:10.1088/0268-1242/30/10/104002 (2015).
199 Ptaszyński, B., Skiba, E. & Krystek, J. Thermal decomposition of alkali metal, copper(I) and silver(I) thiocyanates. *Thermochimica Acta* **319**, 75-85, doi:10.1016/s0040-6031(98)00391-8 (1998).
200 Rietman, E. A. Conduction properties of silver and copper pseudohalides. *Journal of Materials Science Letters* **4**, 542-544, doi:10.1007/bf00720027 (1985).
201 Kalanur, S. S. & Seo, H. Tuning plasmonic properties of CuS thin films via valence band filling. *Rsc Adv* **7**, 11118-11122, doi:10.1039/c6ra27076j (2017).
202 Nozaki, H., Shibata, K. & Ohhashi, N. Metallic hole conduction in CuS. *Journal of Solid State Chemistry* **91**, 306-311, doi:10.1016/0022-4596(91)90085-v (1991).
203 Ludwig, J. *et al.* Ultrafast Hole Trapping and Relaxation Dynamics in p-Type CuS Nanodisks. *J Phys Chem Lett* **6**, 2671-2675, doi:10.1021/acs.jpclett.5b01078 (2015).
204 Lei, H. *et al.* Performance enhancement of polymer solar cells with high work function CuS modified ITO as anodes. *Organic Electronics* **22**, 173-179, doi:10.1016/j.orgel.2015.03.051 (2015).
205 Rao, H. *et al.* Solution-Processed CuS NPs as an Inorganic Hole-Selective Contact Material for Inverted Planar Perovskite Solar Cells. *ACS Appl Mater Interfaces* **8**, 7800-7805, doi:10.1021/acsami.5b12776 (2016).

206 Mao, S. *et al.* A general approach to one-pot fabrication of crumpled graphene-based nanohybrids for energy applications. *ACS Nano* **6**, 7505-7513, doi:10.1021/nn302818j (2012).
207 Mao, S., Wen, Z., Huang, T., Hou, Y. & Chen, J. High-performance bi-functional electrocatalysts of 3D crumpled graphene–cobalt oxide nanohybrids for oxygen reduction and evolution reactions. *Energy Environ. Sci.* **7**, 609-616, doi:10.1039/c3ee42696c (2014).
208 Chen, Y. *et al.* Superior electrocatalysis for hydrogen evolution with crumpled graphene/tungsten disulfide/tungsten trioxide ternary nanohybrids. *Nano Energy* **47**, 66-73, doi:10.1016/j.nanoen.2018.02.023 (2018).
209 Simonescu, C. M., Teodorescu, V. S., Carp, O., Patron, L. & Capatina, C. Thermal behaviour of CuS (covellite) obtained from copper–thiosulfate system. *Journal of Thermal Analysis and Calorimetry* **88**, 71-76, doi:10.1007/s10973-006-8079-z (2007).
210 Li, W.-f., Jiang, L.-h., Zhan, J. & Zhang, C.-f. in *REWAS 2013* 279-285 (John Wiley & Sons, Inc., 2013).
211 Guo, Y. A sensor of sulfuric acid specific gravity for lead-acid batteries. *Sensors and Actuators B: Chemical* **105**, 194-198, doi:10.1016/j.snb.2004.05.061 (2005).
212 Pavlov, D., Naidenov, V. & Ruevski, S. Influence of H2SO4 concentration on lead-acid battery performance. *J Power Sources* **161**, 658-665, doi:10.1016/j.jpowsour.2006.03.081 (2006).
213 Rivera-Utrilla, J. *et al.* Activated carbon modifications to enhance its water treatment applications. An overview. *J Hazard Mater* **187**, 1-23, doi:10.1016/j.jhazmat.2011.01.033 (2011).
214 Yang, B. *et al.* N-doped carbon xerogels as adsorbents for the removal of heavy metal ions from aqueous solution. *RSC Adv.* **5**, 7182-7191, doi:10.1039/c4ra12441c (2014).
215 Canivet, J., Fateeva, A., Guo, Y., Coasne, B. & Farrusseng, D. Water adsorption in MOFs: fundamentals and applications. *Chemical Society reviews* **43**, 5594-5617, doi:10.1039/c4cs00078a (2014).
216 Abney, C. W., Gilhula, J. C., Lu, K. & Lin, W. Metal-organic framework templated inorganic sorbents for rapid and efficient extraction of heavy metals. *Adv Mater* **26**, 7993-7997, doi:10.1002/adma.201403428 (2014).
217 Yeh, C.-N., Raidongia, K., Shao, J., Yang, Q.-H. & Huang, J. On the origin of the stability of graphene oxide membranes in water. *Nature chemistry*, doi:10.1038/nchem.2145 (2015).
218 Li, L. *et al.* Comment on "Environmentally responsible fabrication of efficient perovskite solar cells from recycled car batteries" by Po-Yen Chen, Jifa Qi, Matthew T. Klug, Xiangnan Dang, Paula T. Hammond and Angela M. Belcher, Energy Environ. Sci., 2014. *Energy Environ. Sci.* **8**, 1616-1617, doi:10.1039/c4ee02977a (2015).
219 Huang, Z., Lu, L., Cai, Z. X. & Ren, Z. J. Individual and competitive removal of heavy metals using capacitive deionization. *Journal of Hazardous Materials* **302**, 323-331, doi:10.1016/j.jhazmat.2015.09.064 (2016).
220 Liu, L. J., Guo, X. R., Tallon, R., Huang, X. K. & Chen, J. H. Highly porous N-doped graphene nanosheets for rapid removal of heavy metals from water by capacitive deionization. *Chemical Communications* **53**, 881-884, doi:10.1039/c6cc08515f (2017).

221 Zhang, X. F. *et al.* Three-dimensional honeycomb-like porous carbon derived from corncob for the removal of heavy metals from water by capacitive deionization. *Rsc Adv* **8**, 1159-1167, doi:10.1039/c7ra10689k (2018).
222 Li, J. *et al.* Functionalization of biomass carbonaceous aerogels and their application as electrode materials for electro-enhanced recovery of metal ions. *Environ Sci-Nano* **4**, 1114-1123, doi:10.1039/c7en00019g (2017).
223 Tang, W., Kovalsky, P., Cao, B. & Waite, T. D. Investigation of fluoride removal from low-salinity groundwater by single-pass constant-voltage capacitive deionization. *Water Res* **99**, 112-121, doi:10.1016/j.watres.2016.04.047 (2016).
224 Fan, C. S., Liou, S. Y. H. & Hou, C. H. Capacitive deionization of arsenic-contaminated groundwater in a single-pass mode. *Chemosphere* **184**, 924-931, doi:10.1016/j.chemosphere.2017.06.068 (2017).
225 Suss, M. E. *et al.* Water desalination via capacitive deionization: what is it and what can we expect from it? *Energy Environ. Sci.* **8**, 2296-2319, doi:10.1039/c5ee00519a (2015).
226 Hemmatifar, A., Stadermann, M. & Santiago, J. G. Two-Dimensional Porous Electrode Model for Capacitive Deionization. *J Phys Chem C* **119**, 24681-24694, doi:10.1021/acs.jpcc.5b05847 (2015).
227 Guyes, E. N., Shocron, A. N., Simanovski, A., Biesheuvel, P. M. & Suss, M. E. A one-dimensional model for water desalination by flow-through electrode capacitive deionization. *Desalination* **415**, 8-13, doi:10.1016/j.desal.2017.03.013 (2017).
228 Jande, Y. A. C. & Kim, W. S. Modeling the capacitive deionization batch mode operation for desalination. *J Ind Eng Chem* **20**, 3356-3360, doi:10.1016/j.jiec.2013.12.020 (2014).
229 El-Deen, A. G. *et al.* Flexible 3D Nanoporous Graphene for Desalination and Biodecontamination of Brackish Water via Asymmetric Capacitive Deionization. *Acs Appl Mater Inter* **8**, 25313-25325, doi:10.1021/acsami.6b08658 (2016).
230 Liu, L., Guo, X., Tallon, R., Huang, X. & Chen, J. Highly porous N-doped graphene nanosheets for rapid removal of heavy metals from water by capacitive deionization. *Chemical Communications* **53**, 881-884 (2017).
231 Guo, X., Hou, Y., Ren, R. & Chen, J. Temperature-dependent Crystallization of MoS2 Nanoflakes on Graphene Nanosheets for Electrocatalysis. *Nanoscale Res Lett* **12**, 479, doi:10.1186/s11671-017-2248-9 (2017).
232 Yang, J. *et al.* Self-Assembly of Thiourea-Crosslinked Graphene Oxide Framework Membranes toward Separation of Small Molecules. *Adv Mater*, doi:10.1002/adma.201705775 (2018).
233 Zhao, J., Ren, W. & Cheng, H.-M. Graphene sponge for efficient and repeatable adsorption and desorption of water contaminations. *J Mater Chem* **22**, doi:10.1039/c2jm34128j (2012).
234 Pan, F., Duan, Y., Zhang, X. & Zhang, J. A Facile Synthesis of Nitrogen/Sulfur Co-Doped Graphene for the Oxygen Reduction Reaction. *ChemCatChem* **8**, 163-170, doi:10.1002/cctc.201500893 (2016).
235 Sun, S. R., Gao, L. & Liu, Y. Q. Enhanced dye-sensitized solar cell using graphene-TiO2 photoanode prepared by heterogeneous coagulation. *Appl Phys Lett* **96**, 083113/083111-083113/083113, doi:10.1063/1.3318466 (2010).
236 Tang, Y. B. *et al.* Incorporation of graphenes in nanostructured TiO(2) films via molecular grafting for dye-sensitized solar cell application. *ACS Nano* **4**, 3482-3488, doi:10.1021/nn100449w (2010).

237 He, Z. *et al.* Nanostructure control of graphene-composited TiO2 by a one-step solvothermal approach for high performance dye-sensitized solar cells. *Nanoscale* **3**, 4613-4616, doi:10.1039/c1nr11300c (2011).
238 Song, J. *et al.* Enhancement of photogenerated electron transport in dye-sensitized solar cells with introduction of a reduced graphene oxide-TiO2 junction. *Chemistry* **17**, 10832-10837, doi:10.1002/chem.201101263 (2011).
239 Yang, H. B. *et al.* NiO/Graphene Composite for Enhanced Charge Separation and Collection in p-Type Dye Sensitized Solar Cell. *J Phys Chem C* **115**, 12209-12215, doi:10.1021/jp201178a (2011).
240 Yen, M. Y. *et al.* Preparation of graphene/multi-walled carbon nanotube hybrid and its use as photoanodes of dye-sensitized solar cells. *Carbon* **49**, 3597-3606, doi:10.1016/j.carbon.2011.04.062 (2011).
241 Madhavan, A. A. *et al.* Electrical and optical properties of electrospun TiO2-graphene composite nanofibers and its application as DSSC photo-anodes. *Rsc Adv* **2**, 13032-13037, doi:10.1039/c2ra22091a (2012).
242 Fan, J. J., Liu, S. W. & Yu, J. G. Enhanced photovoltaic performance of dye-sensitized solar cells based on TiO2 nanosheets/graphene composite films. *J Mater Chem* **22**, 17027-17036, doi:10.1039/c2jm33104g (2012).
243 Tang, B. & Hu, G. X. Two kinds of graphene-based composites for photoanode applying in dye-sensitized solar cell. *J Power Sources* **220**, 95-102, doi:10.1016/j.jpowsour.2012.07.093 (2012).
244 Anjusree, G. S., Nair, A. S., Nair, S. V. & Vadukumpully, S. One-pot hydrothermal synthesis of TiO2/graphene nanocomposites for enhanced visible light photocatalysis and photovoltaics. *Rsc Adv* **3**, 12933-12938, doi:10.1039/c3ra41388h (2013).
245 Chatterjee, S., Patra, A. K., Bhaumik, A. & Nandi, A. K. Poly[3-(2-hydroxyethyl)-2,5-thienylene] grafted reduced graphene oxide: an efficient alternate material of TiO2 in dye sensitized solar cells. *Chem Commun (Camb)* **49**, 4646-4648, doi:10.1039/c3cc40843d (2013).
246 Chen, L. *et al.* Enhanced photovoltaic performance of a dye-sensitized solar cell using graphene-TiO2 photoanode prepared by a novel in situ simultaneous reduction-hydrolysis technique. *Nanoscale* **5**, 3481-3485, doi:10.1039/c3nr34059g (2013).
247 Kim, H. N., Yoo, H. & Moon, J. H. Graphene-embedded 3D TiO2 inverse opal electrodes for highly efficient dye-sensitized solar cells: morphological characteristics and photocurrent enhancement. *Nanoscale* **5**, 4200-4204, doi:10.1039/c3nr33672g (2013).
248 Madhavan, A. A. *et al.* Electrospun continuous nanofibers based on a TiO2-ZnO-graphene composite. *Rsc Adv* **3**, 25312-25316, doi:10.1039/c3ra44574g (2013).
249 Shanmugam, M., Durcan, C., Gedrim, R. J., Bansal, T. & Yu, B. Oxygenated-graphene-enabled recombination barrier layer for high performance dye-sensitized solar cell. *Carbon* **60**, 523-530, doi:10.1016/j.carbon.2013.04.083 (2013).
250 Sharma, G. D. *et al.* Enhancement of power conversion efficiency of dye-sensitized solar cells by co-sensitization of zinc-porphyrin and thiocyanate-free ruthenium(II)-terpyridine dyes and graphene modified TiO2 photoanode. *Rsc Adv* **3**, 22412-22420, doi:10.1039/c3ra42537a (2013).

251 Tang, B., Hu, G. X., Gao, H. Y. & Shi, Z. X. Three-dimensional graphene network assisted high performance dye sensitized solar cells. *J Power Sources* **234**, 60-68, doi:10.1016/j.jpowsour.2013.01.130 (2013).
252 Xu, F. *et al.* Graphene Scaffolds Enhanced Photogenerated Electron Transport in ZnO Photoanodes for High-Efficiency Dye-Sensitized Solar Cells. *J Phys Chem C* **117**, 8619-8627, doi:10.1021/jp312379b (2013).

Appendix A: Comparison of Graphene as Photoanode Additives

Ref. No.	Graphene added cell	Preparation method	Reference cell	Graphene added cell		Reference cell	
				I_{sc} mA/cm^2	η %	I_{sc} mA/cm^2	η %
235	Nafion coated graphene with TiO_2 P25	Heterogeneous coagulation	TiO_2 P25	8.38	4.28	5.04	2.70
236	Graphene (from GO) with TiO_2	Molecular grafting	TiO_2	6.67	1.68	1.95	0.32
88	Graphene (from GO) with TiO_2	Solution dispersion	CNT with TiO_2	16.29	6.97	3.35	0.58
237	Graphene (from GO) with TiO_2 P25	Solvothermal approach	TiO_2 P25	13.5*	7.25*	6.20	2.85
238	rGO (from GO) with TiO_2	Spray on to TiO_2 film	TiO_2	18.2	6.06	16.4	5.09
239	Graphene (from GO) with NiO	NiO Solution dispersion	NiO	0.27	0.0094	0.14	0.0034
240	Graphene (from GO) and MWCNTs hybrid with TiO_2	Solution based dispersion	Pristine TiO_2	11.27	6.11	8.61	4.54
241	Graphene (from GO) with TiO_2 nanofiber	Electrospinning	TiO_2 fiber	16.2	7.6	13.9	6.3
242	Graphene (from GO) with TiO_2 nanosheets	Solution based dispersion	TiO_2 nanosheet	16.8	5.77	13.7	4.61
243	Graphene/titanate nanotubes with TiO_2 P25	Hydrothermal methods first to prepare nanotubes, then doctor-blading	Pure TiO_2 P25	18.3	7.54	14.9	6.25
244	Graphene (from GO) with TiO_2	One-pot hydrothermal synthesis	Pure TiO_2	6.13	4.26	4.29	3.22
245	PHET with grafted rGO (from GO)	Molecular grafting	TiO_2	7.5	3.06	5.6	2.66
246	Graphene (from GO) with TiO_2	in *situ* simultaneous reduction-hydrolysis technique	TiO_2	13.93	7.1	10.99	5.3
247	Graphene-embedded 3D TiO_2 inverse opal electrodes	infiltrated into the templates	Pure TiO_2 inverse opal electrode	17.10	7.52	12.39	4.86
248	TiO_2-ZnO-graphene nanocomposite fibers	Electro-spinning	TiO_2-ZnO nano-composite fiber	9.4	3.7	6.3	2.7
249	Multilayer oxygenated graphene with TiO_2	CVD then chemical modification	TiO_2	16.0	6.7	12.7	5.6
250	Graphene modified TiO_2 with modified dyes	Solution based dispersion	TiO_2 with modified dyes	16.69	8.15	16.18	7.35
251	3D graphene network with TiO_2 P25	CVD then solution based dispersion	Pure TiO_2 P25	15.4	6.58	11.9	4.96
252	Graphene with ZnO	Solvothermal process	ZnO	10.89	3.19	7.6	2.31

Appendix B: Additional Data for Sulfur-Treated Graphene / Activated Carbon for CDI Performance in Overtime / Cycling Tests

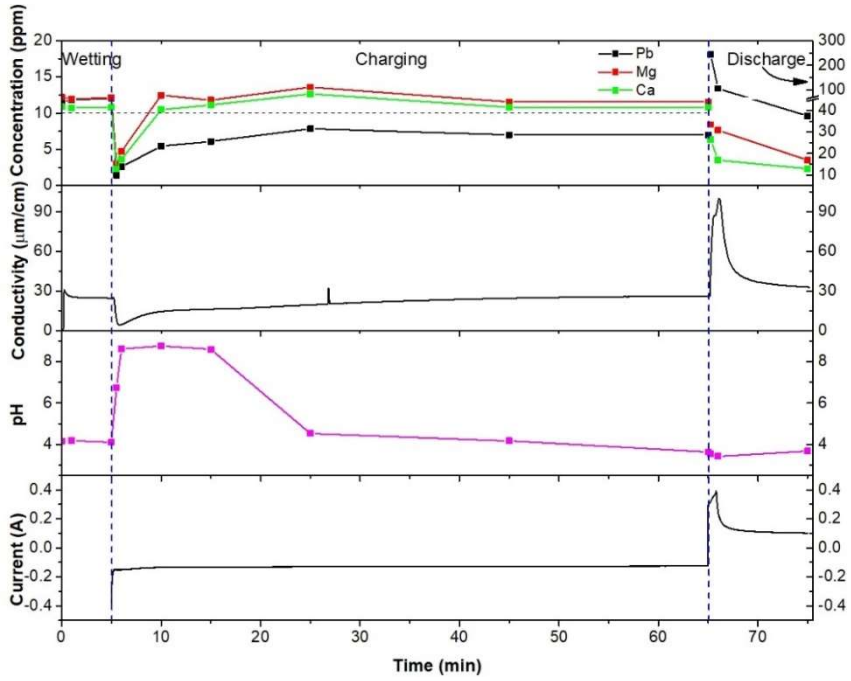

Figure Appendix B-1 Over time CDI test for pure activated carbon treated by thiourea (CS) as CDI electrode

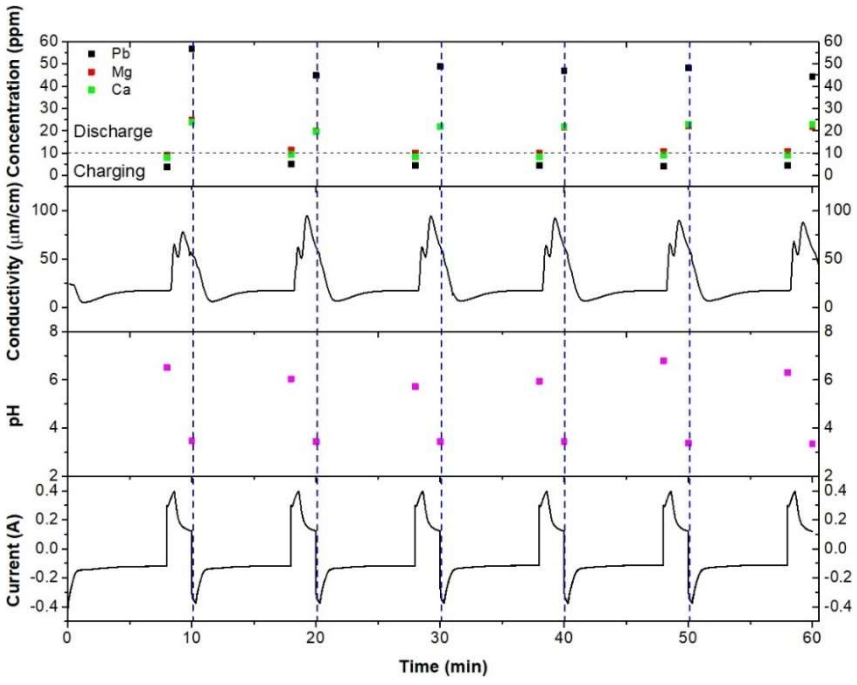

Figure Appendix B-2 Cycling CDI test for pure activated carbon treated by thiourea (CS) as CDI electrode

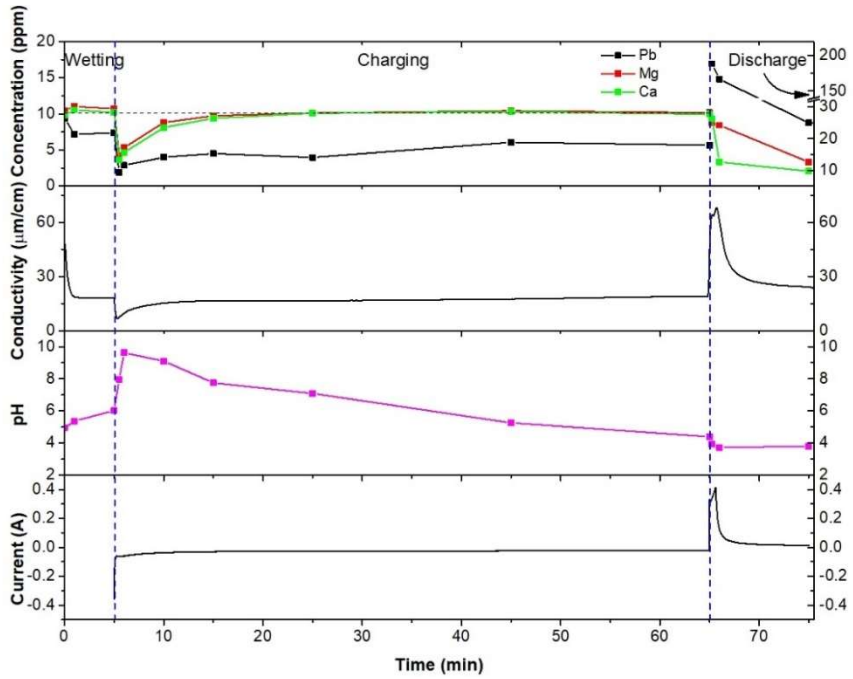

Figure Appendix B-3 Over time CDI test for 12.5 wt.% GO in activated carbon treated by thiourea (12.5GCS) as CDI electrode

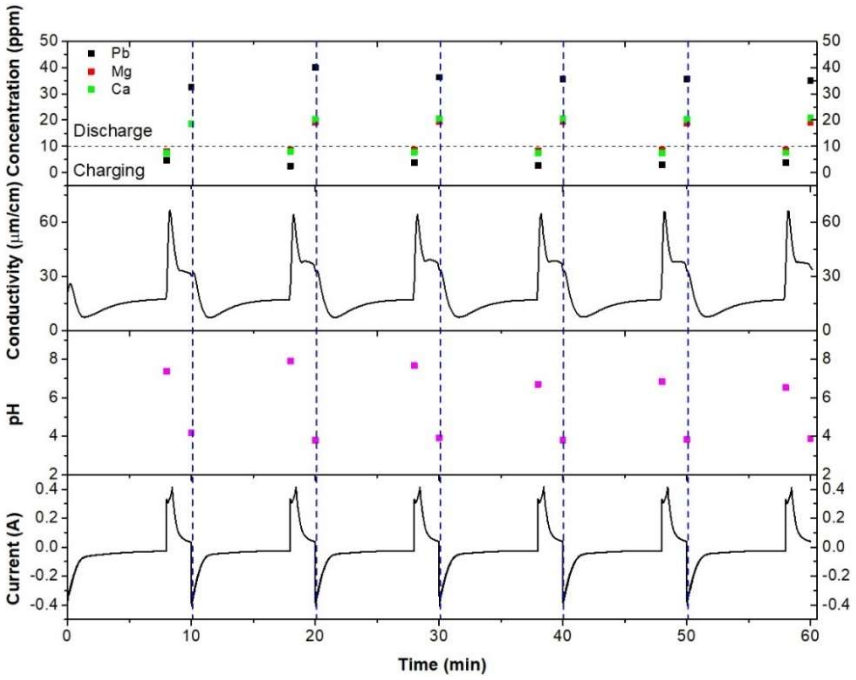

Figure Appendix B-4 Cycling CDI test for 12.5 wt.% GO in activated carbon treated by thiourea (12.5GCS) as CDI electrode

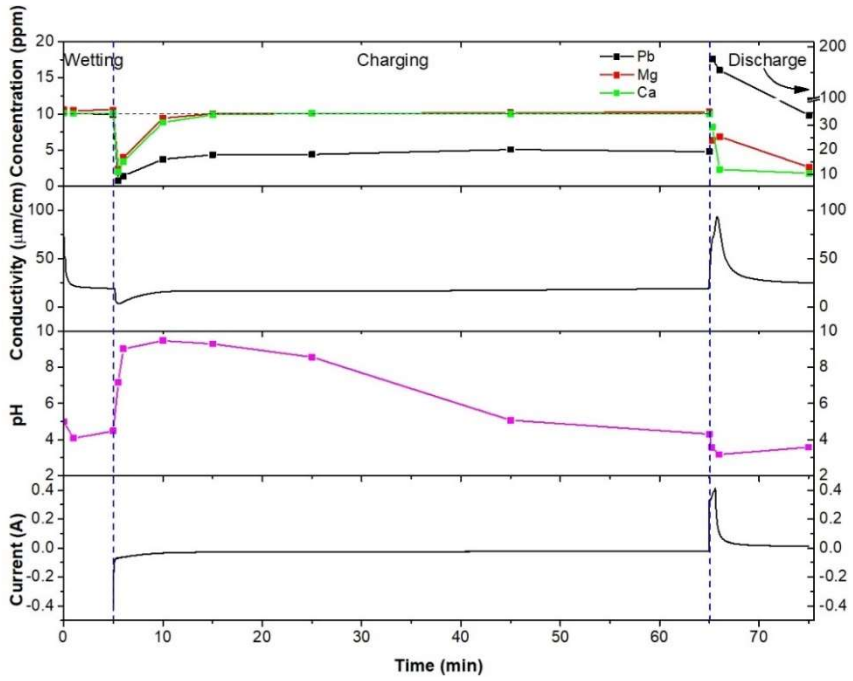

Figure Appendix B-5 Over time CDI test for 25 wt.% GO in activated carbon treated by thiourea (25GCS) as CDI electrode

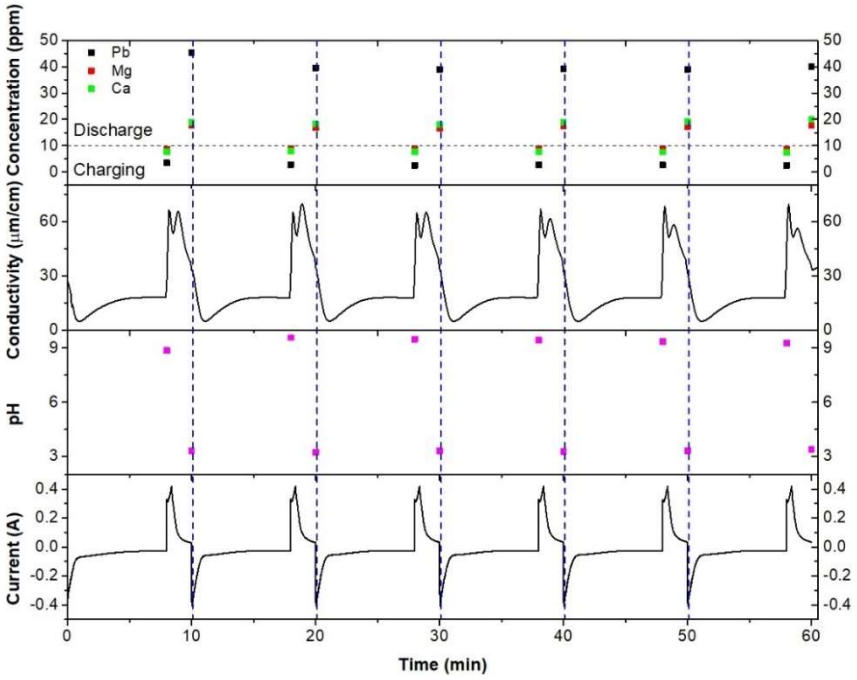

Figure Appendix B-6 Cycling CDI test for 25 wt.% GO in activated carbon treated by thiourea (25GCS) as CDI electrode

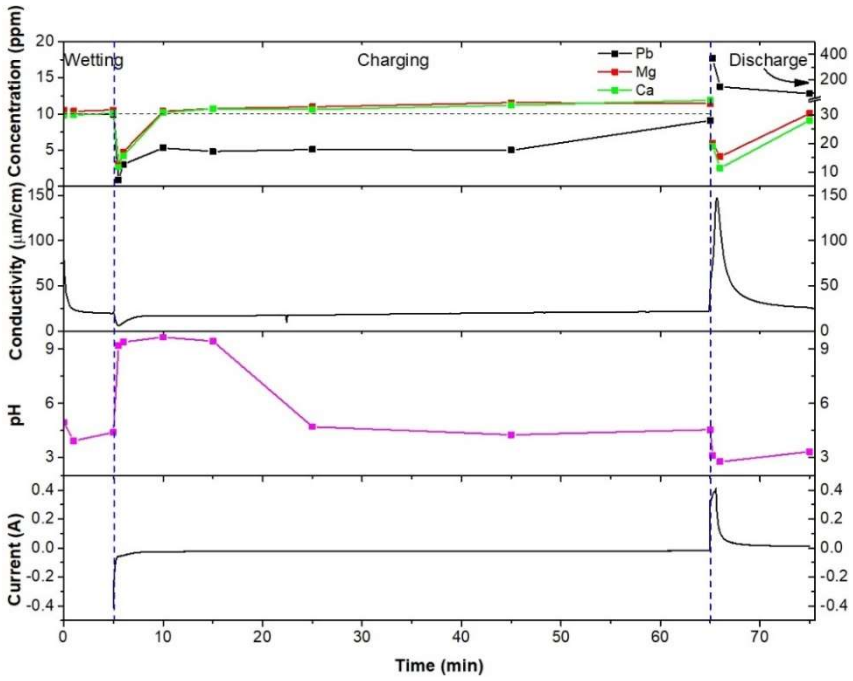

Figure Appendix B-7 Over time CDI test for 50 wt.% GO in activated carbon treated by thiourea (50GCS) as CDI electrode

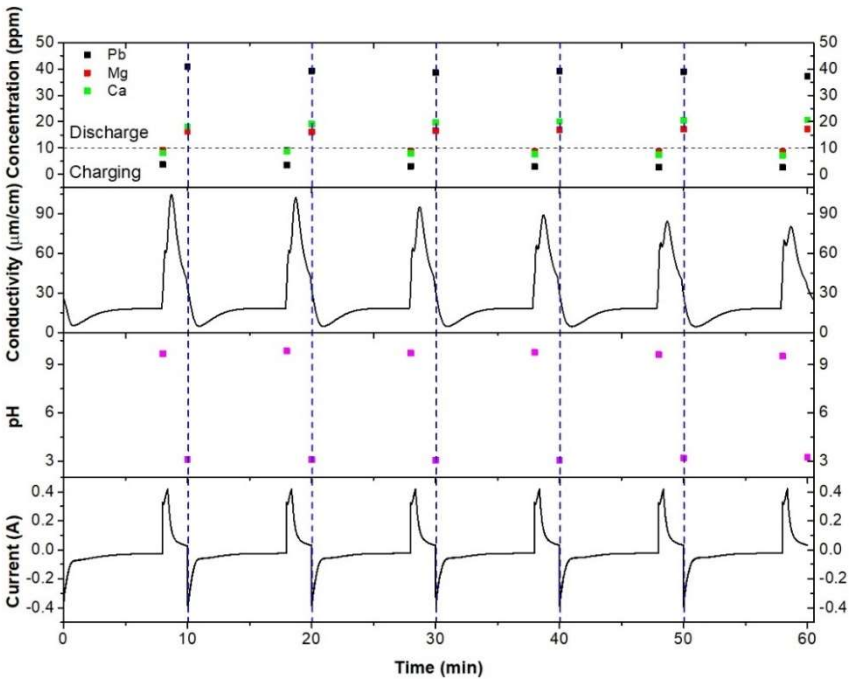

Figure Appendix B-8 Cycling CDI test for 50 wt.% GO in activated carbon treated by thiourea (50GCS) as CDI electrode

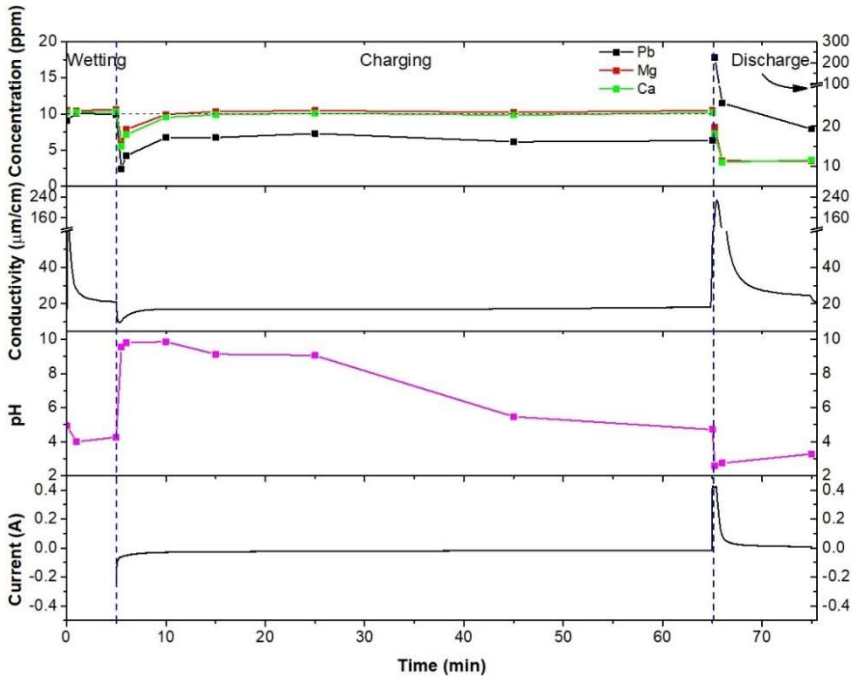

Figure Appendix B-9 Over time CDI test for pure GO treated by thiourea (GS) as CDI electrode

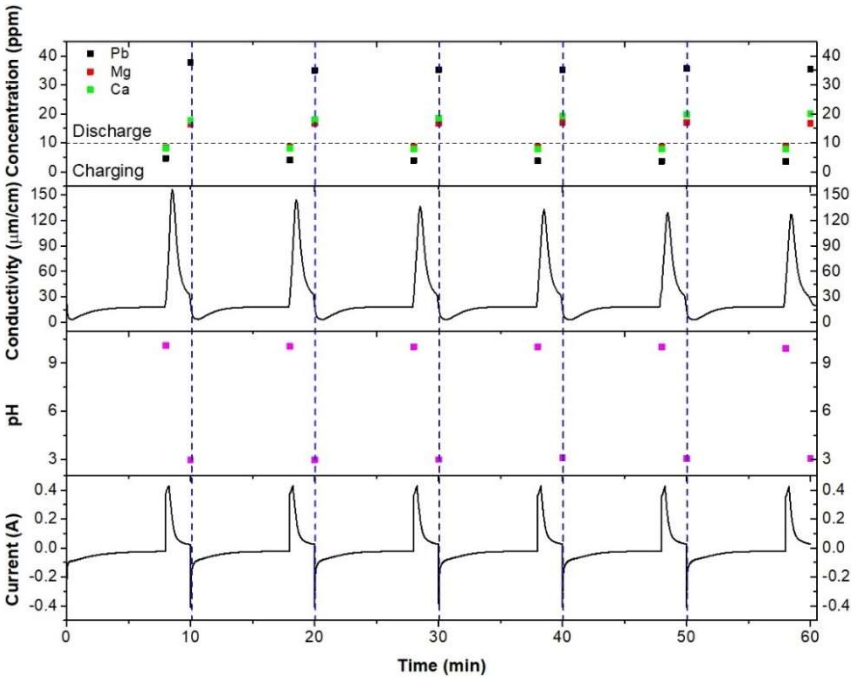

Figure Appendix B-10 Cycling CDI test for pure GO treated by thiourea (GS) as CDI electrode

Curriculum Vitae

Xiaoru Guo

Education

Ph.D. of Engineering 05/2018

University of Wisconsin-Milwaukee, WI, USA

Dissertation Title: Novel Solar Cells Based on Two-Dimensional Nanomaterials and Recycled Lead Components

Advisor: Dr. Junhong Chen

B.S. of Thermal Engineering 07/2011

Tsinghua University, Beijing, China

Research Experience

Nanocarbon Materials Based Capacitive Deionization for Water Treatment

University of Wisconsin-Milwaukee, WI, USA 01/2017 – Present

- Prepared carbon-based nanomaterials, especially graphene composites, for lead recycling from contaminated water in drinking water system
- Designed and constructed capacitive deionization cells, and tested ion removal performances in contaminated water
- Studied lead recovery methods for new battery or solar cell use

Nanomaterial Preparation for Batteries and Other Energy Applications

University of Wisconsin-Milwaukee, WI, USA 09/2012 – Present

- Prepared 2D nanomaterials for energy applications, including photocatalysts, lithium-ion batteries and solar cells
- Studied electrochemical catalytic activity of 2D material hybrids
- Fabricated and tested dye-sensitized solar cells and perovskite solar cells
- Failure study and reliability analysis of nanomaterials over solar cells life time

2D Nanomaterial Study for Lead Removal and Reform from Waste Sulfuric Acid

University of Wisconsin-Milwaukee, WI, USA 09/2014 – 12/2015

- Prepared multiple carbon-based nanomaterials, including graphene oxide, metal-oxide frameworks, modified activated carbon and activated carbon/graphene composites, for waste sulfuric acid purification from used lead-acid batteries, targeting iron, copper, nickel, magnesium and zinc.
- Studied 2D nanomaterial adsorption and filtration performance in strong acidic environment
- Designed and constructed capacitive deionization cells, and tested ion removal performances in waste acid

- Studied lead recovery methods for new battery or solar cell use

Multi-Energy Complementary Distributed CCHP Systems

Tsinghua University, Beijing, China 11/2010 – 07/2011

- Studied lithium bromide aqueous solution thermal properties.
- Constructed a multi-energy complementary experimental bench, and verified design with simulating calculations.

Engine and Transmission Redesign, Formula Student China

Tsinghua University, Beijing, China 10/2008 – 10/2010

- Redesigned and optimized a 600cc engine for a FSAE-student car through Catia. Simulations and analysis were done through Ansys.
- Designed car raced in 2010 Formula Student China.

Teaching & Advising

Teaching Assistant, University of Wisconsin-Milwaukee

- ME 110 Engineering Fundamentals I 08/2017 – 05/2018
  Assisted teaching Creo for modeling. Assisted teaching introduction to engineering disciplines, problem solving, visualization, technical communication, and data collection and analysis.
- ME 111 Engineering Fundamentals II 01/2018 – 05/2018
  Assisted teaching advanced Creo skills for modeling and analysis. Assisted teaching intermediate problem-solving skills, experimentation, technical communication and engineering design.
- ME 301 Basic Engineering Thermodynamics 08/2016 – 05/2017
- ME 321 Basic Heat Transfer 01/2017 – 05/2017
- ME 438 Mechanical Engineering Experimentation 08/2013 – 05/2014
  Assisted teaching data acquisition systems, experiment planning, sensor calibration, professional report writing and communication.

Work Experience

Teaching and Research Assistant, University of Wisconsin-Milwaukee 08/2012 – Present

- Studied 2D nanomaterials, especially graphene-based materials.
- Studied multiple thin-film growth / coating techniques, including CVD, PVD, ALD and more.
- Studied multiple energy and environment applications, including solar cells, catalysts, batteries and capacitive deionization.
- Studied 2D nanomaterial based chemical sensors for blood tests and FET sensors for gas sensing and water analysis.
- Studied 3D printing of biomaterials for artificial organs. Design and constructed 3D printing systems.
- Assisted teaching undergraduate mechanical engineering classes, including engineering ethics, basic skills, thermodynamics, heat transfer and experiment design.

Advanced Manufacturing Intern, Johnson Controls 06/2014 – 08/2014

- Screened recycling methods for lithium-ion batteries to prepare for upcoming battery recycling challenges. Reports include possible recycling methods, market analysis and extensive comparisons. Compiled recommendations for recycling options.
- Studied lithium-ion battery screening methods for defects in large-scale production environment.
- Researched lead-acid battery and lithium-ion battery separation technology, to reduce recycling facility incidents, especially fluorine leaking from mixed battery packs.
- Onsite studies of lead-acid battery manufacturing and testing.

Scrub, Hulu Beijing R&D Center 10/2011 – 08/2012

- Supported face recognition research. Maintained internal front end with Ruby and Python.

Conference Presentation

The 231st Electrochemical Society Meeting

Oral Presentation Title: Temperature-Dependent Hydrothermal Preparation of MoS2/Graphene Hybrid Electrocatalyst

---

Publications

Citations: 878 h-index: 10 i10-index: 11 Updated on April 28, 2018

Solar Cells:

1) Gao, X.; Li, J.; Gollon, S.; Qiu, M.; Guan, D.; Guo, X.; Chen, J.; Yuan, C. A TiO 2 Nanotube Network Electron Transport Layer for High Efficiency Perovskite Solar Cells. *Phys. Chem. Chem. Phys.* **2017**, *19* (7), 4956–4961.
2) Guo, X.; Hou, Y.; Ren, R.; Chen, J. Temperature-Dependent Crystallization of MoS 2 Nanoflakes on Graphene Nanosheets for Electrocatalysis. *Nanoscale Res. Lett.* **2017**, *12* (1), 479.
3) Guo, X.; Lu, G.; Chen, J. Graphene-Based Materials for Photoanodes in Dye-Sensitized Solar Cells. *Front. Energy Res.* **2015**, *3*, 50.

Water Treatment:

4) Liu, L.; Guo, X.; Tallon, R.; Huang, X.; Chen, J. Highly Porous N-Doped Graphene Nanosheets for Rapid Removal of Heavy Metals from Water by Capacitive Deionization. *Chem Commun* **2017**, *53* (5), 881–884.

Sensors:

5) Thakur, B.; Guo, X.; Chang, J.; Kron, M.; Chen, J. Porous Carbon and Prussian Blue Composite: A Highly Sensitive Electrochemical Platform for Glucose Biosensing. *Sens. Bio-Sensing Res.* **2017**, *14*, 47–53.
6) Chen, Y.; Ren, R.; Pu, H.; Guo, X.; Chang, J.; Zhou, G.; Mao, S.; Kron, M.; Chen, J. Field-Effect Transistor Biosensor for Rapid Detection of Ebola Antigen. *Sci. Rep.* **2017**, *7* (1), 10974.
7) Cui, S. M.; Guo, X. R.; Ren, R.; Zhou, G. H.; Chen, J. H. Decoration of Vertical Graphene with Aerosol Nanoparticles for Gas Sensing. *J. Phys. D-Applied Phys.* **2015**, *48* (31).

Other Energy Applications:

8) Huang, X.; Sui, X.; Yang, H.; Ren, R.; Wu, Y.; Guo, X.; Chen, J. HF-Free Synthesis of Si/C Yolk/Shell Anodes for Lithium-Ion Batteries. *J. Mater. Chem. A* **2018**, *6* (6), 2593–2599.
9) Wu, Y.; Huang, X.; Huang, L.; Guo, X.; Ren, R.; Liu, D.; Qu, D.; Chen, J. Self-Healing Liquid Metal and Si Composite as a High-Performance Anode for Lithium-Ion Batteries. *ACS Appl. Energy Mater.* **2018**.
10) Wu, Y.; Huang, L.; Huang, X.; Guo, X.; Liu, D.; Zheng, D.; Zhang, X.; Ren, R.; Qu, D.; Chen, J. A Room-Temperature Liquid Metal-Based Self-Healing Anode for Lithium-Ion Batteries with an Ultra-Long Cycle Life. *Energy Environ. Sci.* **2017**, *10* (8), 1854–1861.
11) Liu, L.; Huang, X.; Guo, X.; Mao, S.; Chen, J. Decorating in Situ Ultrasmall Tin Particles on Crumpled N-Doped Graphene for Lithium-Ion Batteries with a Long Life Cycle. *J. Power Sources* **2016**, *328*, 482–491.
12) Hou, Y.; Yuan, H.; Wen, Z.; Cui, S.; Guo, X.; He, Z.; Chen, J. Nitrogen-Doped Graphene/CoNi Alloy Encased within Bamboo-like Carbon Nanotube Hybrids as Cathode Catalysts in Microbial Fuel Cells. *J. Power Sources* **2016**, *307*, 561–568.
13) Yuan, H.; Hou, Y.; Wen, Z.; Guo, X.; Chen, J.; He, Z. Porous Carbon Nanosheets Codoped with Nitrogen and Sulfur for Oxygen Reduction Reaction in Microbial Fuel Cells. *ACS Appl Mater Interfaces* **2015**, *7* (33), 18672–18678.
14) Hou, Y.; Cui, S.; Wen, Z.; Guo, X.; Feng, X.; Chen, J. Electrocatalysis: Strongly Coupled 3D Hybrids of N-Doped Porous Carbon Nanosheet/CoNi Alloy-Encapsulated Carbon Nanotubes for Enhanced Electrocatalysis (Small 44/2015). *Small* **2015**, *11* (44), 5939.
15) Hou, Y.; Cui, S.; Wen, Z.; Guo, X.; Feng, X.; Chen, J. Strongly Coupled 3D Hybrids of N-Doped Porous Carbon Nanosheet/CoNi Alloy-Encapsulated Carbon Nanotubes for Enhanced Electrocatalysis. *Small* **2015**, *11* (44), 5940–5948.
16) Mao, S.; Wen, Z.; Ci, S.; Guo, X.; Ostrikov, K. K.; Chen, J. Perpendicularly Oriented MoSe2 /Graphene Nanosheets as Advanced Electrocatalysts for Hydrogen Evolution. *Small* **2015**, *11* (4), 414–419.
17) Mao, S.; Wen, Z.; Ci, S.; Guo, X.; Ostrikov, K.; Chen, J. Hydrogen Evolution: Perpendicularly Oriented MoSe2/Graphene Nanosheets as Advanced Electrocatalysts for Hydrogen Evolution (Small 4/2015). *Small* **2015**, *11* (4), 508.
18) Ren, R.; Wen, Z.; Cui, S.; Hou, Y.; Guo, X.; Chen, J. Controllable Synthesis and Tunable Photocatalytic Properties of Ti(3+)-Doped TiO2. *Sci Rep* **2015**, *5*, 10714.
19) Kim, H.; Huang, X. K.; Wen, Z. H.; Cui, S. M.; Guo, X. R.; Chen, J. H. Novel Hybrid Si Film/Carbon Nanofibers as Anode Materials in Lithium-Ion Batteries. *J. Mater. Chem. A* **2015**, *3* (5), 1947–1952.
20) Kim, H.; Huang, X.; Guo, X.; Wen, Z.; Cui, S.; Chen, J. Novel Hybrid Carbon Nanofiber/Highly Branched Graphene Nanosheet for Anode Materials in Lithium-Ion Batteries. *ACS Appl Mater Interfaces* **2014**, *6* (21), 18590–18596.
21) Hou, Y.; Zhang, B.; Wen, Z. H.; Cui, S. M.; Guo, X. R.; He, Z.; Chen, J. H. A 3D Hybrid of Layered MoS2/Nitrogen-Doped Graphene Nanosheet Aerogels: An Effective Catalyst for Hydrogen Evolution in Microbial Electrolysis Cells. *J. Mater. Chem. A* **2014**, *2* (34), 13795–13800.

22) Hou, Y.; Wen, Z.; Cui, S.; Guo, X.; Chen, J. Constructing 2D Porous Graphitic C3 N4 Nanosheets/Nitrogen-Doped Graphene/Layered MoS2 Ternary Nanojunction with Enhanced Photoelectrochemical Activity. *Adv Mater* **2013**, *25* (43), 6291–6297.

Biomaterial Printing:

23) McCune, D.; Guo, X.; Shi, T.; Stealey, S.; Antrobus, R.; Kaltchev, M.; Chen, J.; Kumpaty, S.; Hua, X.; Ren, W.; et al. Electrospinning Pectin-Based Nanofibers: A Parametric and Cross-Linker Study. *Appl. Nanosci.* **2018**, *8* (1–2), 33–40.
24) Banks, A.; Guo, X.; Chen, J.; Kumpaty, S.; Zhang, W. Novel Bioprinting Method Using a Pectin Based Bioink. *Technol. Heal. Care* **2017**, *25* (4), 651–655.
25) Zhang, W.; Bissen, M. J.; Savela, E. S.; Clausen, J. N.; Fredricks, S. J.; Guo, X.; Paquin, Z. R.; Dohn, R. P.; Pavelich, I. J.; Polovchak, A. L.; et al. Design of Artificial Red Blood Cells Using Polymeric Hydrogel Microcapsules: Hydrogel Stability Improvement and Polymer Selection. *Int J Artif Organs* **2016**, 0.
26) Crouse, J. Z.; Mahuta, K. M.; Mikulski, B. A.; Harvestine, J. N.; Guo, X.; Lee, J. C.; Kaltchev, M. G.; Midelfort, K. S.; Tritt, C. S.; Chen, J.; et al. Development of a Microscale Red Blood Cell-Shaped Pectin-Oligochitosan Hydrogel System Using an Electrospray-Vibration Method: Preparation and Characterization. *J. Appl. Biomater. Funct. Mater.* **2015**, *13* (4), 0–0.
27) Harvestine, J. N.; Mikulski, B. A.; Mahuta, K. M.; Crouse, J. Z.; Guo, X. R.; Lee, J. C.; Midelfort, K. S.; Chen, J. H.; Zhang, W. J. A Novel Red-Blood-Cell-Shaped Pectin-Oligochitosan Hydrogel System. *Part. Part. Syst. Charact.* **2014**, *31* (9), 955–959.
28) Harvestine, J. N.; Mikulski, B. A.; Mahuta, K. M.; Crouse, J. Z.; Guo, X.; Lee, J. C.; Midelfort, K. S.; Chen, J.; Zhang, W. Hydrogels: A Novel Red-Blood-Cell-Shaped Pectin-Oligochitosan Hydrogel System (Part. Part. Syst. Charact. 9/2014). *Part. Part. Syst. Charact.* **2014**, *31* (9), 912.

Honors & Awards

Chancellor's Graduate Student Award, UW-Milwaukee	2012, 2013, 2014, 2015, 2016, 2018
Best Student Presentation, Water Equipment and Policy (WEP) NSF I/UCRC	10/18/2017
ECS Travel Grant, The Electrochemical Society	05/2017
Graduate Student Travel Grant, UW-Milwaukee	05/2017
UWM CEAS Dean's Award, UW-Milwaukee	08/2014 – 05/2015
Social Work Scholarship, Tsinghua University	2010
"Practice for Energy Sources and Environment" Award, Tsinghua University	2008